APPROXIMATING AMBIENT *D*-REGION ELECTRON DENSITIES USING DUAL-BEAM HF HEATING EXPERIMENTS AT THE HIGH-FREQUENCY ACTIVE AURORAL RESEARCH PROGRAM (HAARP)

By

DIVYA AGRAWAL

A DISSERTATION PRESENTED TO THE GRADUATE SCHOOL
OF THE UNIVERSITY OF FLORIDA IN PARTIAL FULFILLMENT
OF THE REQUIREMENTS FOR THE DEGREE OF
DOCTOR OF PHILOSOPHY

UNIVERSITY OF FLORIDA

2013

This dissertation is dedicated to my parents

Renu *and* Susheel

and to my husband

Alexander

ACKNOWLEDGMENTS

I would like to thank my advisor Dr. Robert Moore for providing me the wonderful opportunity to perform this work and for his patience and guidance through the years. I am particularly grateful to my committee members, Dr. Jenshan Lin, Dr. Martin Uman, and Dr. Norman Fitz-Coy for their valuable comments and suggestions.

I extend special thanks to new and old friends at the ionospheric research lab, especially Shuji Fujimaru who has provided me invaluable support and motivation, Daniel Kotovsky for his valuable discussions, Michael Mitchell for building all the hardware, and Neal Dupree for his expertise using the high performance computing facility. I also want to thank the newest members of our group Brittany Finch for her assistance in processing some data and Sydney Greene for being a true friend.

I would like to extend my appreciation to the administrative staff of the ECE department. Shannon Chillingworth, our graduate student advisor has made my life easier on so many levels, Stephenie Sparkman, Edwina McKay and Angela Petringelo for effortlessly running the front office with a warm smile. Janet Holman, Erlinda Lane, Kym Mason and Jennifer Freeman for making our travels and purchasing so much easier and less stressful. I would like to also thank Ray McClure and Waleta Newman for taking care of all our packages and shipments and Laurie Edvardsson for helping me with printing and binding my dissertation. They have all enriched my graduate school experience and been my pillar of support.

This research would not have been successful without the help of the crew from Alaska. I would especially like to thank the owners of Chistochina B&B, Norma and Doyle Traw for taking good care and checking on us and our receiver site. Jay Scrimshaw and Dugh & Judy for minding our receiver sites at Oasis and Paradise respectively. We were able to get phenomenal data from these receiver sites, which has been extensively used in this research. I would also like to thank the HAARP crew, Jay Scrimshaw, Marty Karjala and Stephen for providing the inexperienced Florida

students with Alaskan weather gear and mentoring us on so many levels and sharing their Alaskan experiences with us. In addition, I would like to thank the operators of HAARP, Mike McCarrick, Helio Zwi and Dave Seafolk-Kopp who have accommodated our last minute changes in transmission formats and have worked tirelessly on all the campaigns. Last, but definitely not the least, I would like to thank Ed Kennedy and Lee Synder for their contribution in running the campaigns and providing me support and guidance in the chat room.

This work would not have been possible without the love and support of some of my dear friends, Sendhil, Heera, Bharani, Jennifer Jackson, Erin Patrick, Laureen Ricks, Anitra, Gayatri, Pareena, Atchar, Suresh. I of course can't list all your names, but you know who you are.

I am thankful to Aunty Pramila, Aunty Radha, Uncle Subarna, Uncle Tirtha, Asha and Sheela for opening their home to me, for the delicious home cooked meals and for loving and caring me like their own. I always looked forward to spending weekends and holidays with them. My parents, Renu and Susheel although across the Atlantic, have been my biggest strength through the years. Their phone calls and Skype calls would brighten my day. I thank them from the bottom of my heart for their love, support and commitment. I thank my brother Nikhil and his family for checking on me, advising and supporting me. My in-laws, Don BK and Doñya Zoila, Carol and Johny for their love and support. Lastly, my dear husband Alex for his love, support, guidance, motivation and patience through the years. I am looking forward to our exciting journey together.

This work is supported by US Air Force grant FA9453-12-1-00246, DARPA contract HR0011-09-C-0099, DARPA grant HR0011-10-1-0061, ONR grant #N000141010909, and NSF grants AGS-0940248 and ANT-0944639 to the University of Florida.

TABLE OF CONTENTS

LIST OF TABLES

LIST OF FIGURES

LIST OF ABBREVIATIONS AND SYMBOLS

ABBREVIATIONS :

CW Continuous Wave

ELF Extremely Low Frequency (3-3000 Hz)

ERP Effective Radiated Power

HAARP High-frequency Active Auroral Research Program

HF High Frequency (3-30 MHz)

OA Oasis Receiver location ($\sim$3 km from HAARP)

PD Paradise Receiver location ($\sim$98 km from HAARP)

SC Sinona Creek Receiver location ($\sim$33 km from HAARP)

TOA Time-of-Arrival

VLF Very Low Frequency (3-30 kHz)

SYM BOLS :

f_c Center Frequency (MHz)

N_e Electron Density Profile (elec/cm^{-3})

T_e Electron Temperature Profile (kelvin)

Abstract of Dissertation Presented to the Graduate School
of the University of Florida in Partial Fulfillment of the
Requirements for the Degree of Doctor of Philosophy

APPROXIMATING AMBIENT *D*-REGION ELECTRON DENSITIES USING DUAL-BEAM HF HEATING EXPERIMENTS AT THE HIGH-FREQUENCY ACTIVE AURORAL RESEARCH PROGRAM (HAARP)

By

Divya Agrawal

August 2013

Chair: Robert Moore
Major: Electrical and Computer Engineering

Dual-beam ELF/VLF wave generation experiments performed at the High-frequency Active Auroral Research Program (HAARP) HF transmitter in Gakona, Alaska are critically compared with the predictions of a newly developed ionospheric high frequency (HF) heating model that accounts for the simultaneous propagation and absorption of multiple HF beams. The dual-beam HF heating experiments presented herein consist of two HF beams transmitting simultaneously: one amplitude modulated (AM) HF beam modulates the conductivity of the lower ionosphere in the extremely low frequency (ELF, 30 Hz to 3 kHz) and/or very low frequency (VLF, 3 kHz to 30 kHz) band while a second HF beam broadcasts a continuous waveform (CW) signal, modifying the efficiency of ELF/VLF conductivity modulation and thereby the efficiency of ELF/VLF wave generation. Ground-based experimental observations are used together with the predictions of the theoretical model to identify the property of the received ELF/VLF wave that is most sensitive to the effects of multi-beam HF heating, and that property is determined to be the ELF/VLF signal magnitude. The dependence of the generated ELF/VLF wave magnitude on several HF transmission parameters (HF power, HF frequency, and modulation waveform) is then experimentally measured and analyzed within the context of the multi-beam HF heating model. For all cases studied, the received ELF/VLF wave magnitude as a function of transmission parameter is analyzed

to identify the dependence on the ambient D-region electron density (N_e) and/or electron temperature (T_e), in turn identifying the HF transmission parameters that provide significant independent information regarding the ambient conditions of the D-region ionosphere. A theoretical analysis is performed to determine the conditions under which the effects of N_e and T_e can be decoupled, and the results of this analysis are applied to identify an electron density profile that can reproduce the unusually high level of ELF/VLF magnitude suppression observed on 25 July 2011. Finally, dual-beam ELF/VLF time of arrival (TOA) observations are analyzed and used to demonstrate that the dual-beam experiment is sensitive to structure within the D-region ionosphere.

CHAPTER 1
INTRODUCTION

This Ph.D. dissertation experimentally and theoretically investigates a novel method to estimate the ambient conditions of the D-region ionosphere. The technique requires a high power, high frequency (HF, 3-30 MHz) transmitter such as that available at the **H**igh-frequency **A**ctive **A**uroral **R**esearch **P**rogram (**HAARP**) observatory in Gakona, Alaska. A dual-beam HF heating transmission format is used to quantify the suppression and/or enhancement of the extremely low frequency (ELF, 30 Hz to 3 kHz)/very low frequency (VLF, 3-30 kHz) signal magnitude generated using an amplitude modulated (AM) beam by the addition of a continuous wave (CW) beam at varying HF power levels, HF frequencies, and HF polarizations. In order to understand the impact of the presented material, this chapter provides background information about the ionosphere in general together with a historical context regarding the characterization of electrical parameters within the weakly ionized and highly collisional D-region ionosphere. We present a brief outline of the approach to the problem and summarize the scientific contributions of this work.

1.1 The Ionosphere

> *Shortly before midday I placed the single earphone to my ear and started listening. The receiver on the table before me was very crude - a few coils and condensers and a coherer - no valves, no amplifiers, not even a crystal. But I was at last on the point of putting the correctness of all my beliefs to test. The answer came at 12:30 when I heard, faintly but distinctly, pip-pip-pip. I handed the phone to Kemp : "Can you hear anything?" I asked. "Yes," he said. "The letter S." He could hear it.*
>
> - Guglielmo Marconi, December 12, 1901.

Marconi's words following the transmission of the first wireless trans-Atlantic message between Poldhu, Cornwall on England's SouthWest coast and Saint Johns, Newfoundland Canada, about 3500 kilometers apart, conveys the excitement of this discovery. This experimental observation led to Kennelly and Heaviside making independent suggestions in 1902 that there existed an ionized layer in the Earth's

upper atmosphere that could reflect radio waves around the curved surface of the Earth. A staunch scientific debate ensued regarding the existence of the so called Kennelly-Heaviside layer. The concept of a 'radio reflecting layer'; did not receive general scientific acceptance until the early 1920's. It is generally accepted that *Appleton and Barnett* [1925] and *Appleton* [1932] experimentally proved the existence of the atmospheric ionized layer along with an estimate of the height of the reflecting layer. In retrospect, it was actually *de Forest* [1912] who made the first approximate measurements of the height of the 'radio reflecting layer' and it is unfortunate that his contribution is often overlooked in the works of radio communication. *Villard* [1976] provides a detailed essay on the contributions of Lee de Forrest and his colleague Leonard F. Fuller. Nevertheless, with the scientifically accepted proof provided by *Appleton and Barnett* [1925] and *Appleton* [1932], the term "Ionosphere" replaced the term "Kennelly-Heaviside layer".

The ionosphere is an example of a naturally occurring, weakly-ionized plasma and consists predominantly of neutral particles, but also of free electrons and positive ions that are assumed to be approximately equal in number. Based on the level of ionization, the ionosphere is divided into layers, with the D-region extending from $\sim$50 – 100 km, the E-region from $\sim$100 – 150 km, and the F-region starting at $\sim$150 km. *Tellegen* [1933] first introduced the concept of artificial ionospheric modification by high power radio waves. High power radio wave heating of the ionosphere provides a means to perform controlled ionospheric modification experiments. Since 1933, plasma physics and the scientific understanding of the ionosphere has dramatically improved. Scientists now investigate the ionosphere for a variety of reasons. There are effects related to lightning (transient luminous events, lightning-induced electron precipitation), effects driven by solar activity (X-ray flares), effects related to intergalactic radiation (γ rays), effects of radiation belt dynamics (via lightning-induced electron precipitation), and effects of atmospheric gravity waves, to name a few.

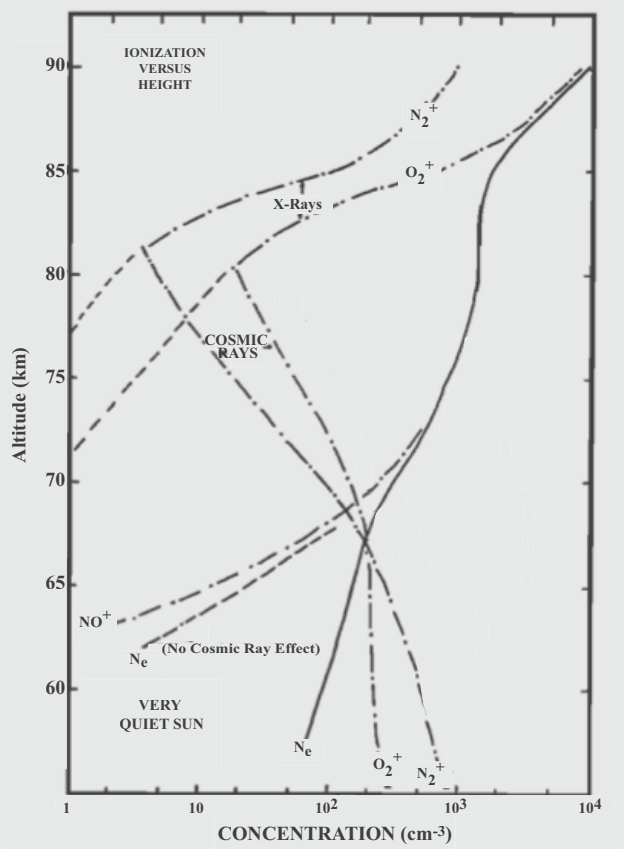

Figure 1-1. Concentrations of positive ions (N_2^+, O_2^+,NO^+), negative ions (O_2^-,) and electrons (n_e) versus altitude for a very quiet sun, adapted from *Nicolet and Aikin* [1960].

1.2 The *D*-Region Ionosphere

The *D*-region ionosphere ($\sim$50 – 100 km) is the weakly ionized and highly collisional plasma layer of the ionosphere, and it serves as an interface between the neutral atmosphere and the more highly ionized atmospheric layers. Ionization in this region is produced by solar X rays, both during solar flares and under normal solar conditions. The primary ionizing radiations from the sun are the discrete Lyman-α line at 1216 Å in the ultraviolet, and hard X-rays of wavelength $<$ 10 Å [*Davies*, 1990, p.33]. *Nicolet and Aikin* [1960] provide a detailed discussion on the primary constituents of the *D*-region: molecular nitrogen and oxygen, nitric oxide, and positive and negative ions. Disturbances within this layer greatly affect the absorption of high frequency waves and the reflection of low frequency radio signals. Figure 1-1 shows the various constituents

of the D-region ionosphere as a function of altitude. The general perception of the D-region constituents has not changed dramatically since 1960.

The D-region is mainly characterized by electron density, neutral density, and electron temperature profiles. The characteristic parameters of the D-region vary with day, season, solar activity, zenith angle, and geographic locations, among others. Radio waves are absorbed as they propagate through the D-region due to the high electron-neutral collision frequency. In fact, the D-region is the primary source of radio wave attenuation for waves propagating from the ground into space and vice versa. Characterizing the electrical properties of the D-region ionosphere is thus an important goal in the effort to understand the dynamic coupling of radio wave energy between the ground and space.

The following section provides an overview of previous efforts to characterize the D-region of the ionosphere.

1.3 Previous Efforts to Characterize the D-Region Ionosphere

The D-region ionosphere is particularly difficult to characterize because its altitude is typically too high for balloon measurements and/or too low for radar and satellite measurements. Efforts to probe the D-region have been performed using rockets, radars, ionosondes, and topside sounders. The list continues with differential absorption and differential phase measurements of partial HF reflection measurements, VLF, low frequency (LF), and medium frequency (MF) sounding techniques. Some of the major efforts in the direction of characterizing the ambient D-region electron density are discussed below.

1.3.1 Rocket Sounding Techniques

The salient methods to probe the D-region ionosphere using rocket sounding include the LF radio wave propagation technique, the VLF Doppler technique, and the Langmuir probe technique that measures both positive and negative or electron currents [*Sechrist*, 1974, and references therein]. These techniques are based on

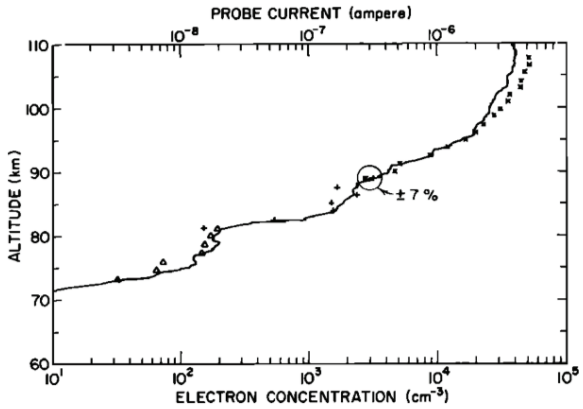

Figure 1-2. Electron concentrations derived from a two-frequency rocket differential absorption (Δ) and Faraday rotation (X, 3385 kHz; +, 2225 kHz) experiment. The solid line is the uncalibrated dc probe current; adapted from *Sechrist* [1974].

measurements of Faraday rotation and differential absorption. For example, Figure 1-2 shows the electron concentrations derived from the differential absorption, Faraday rotation, and dc probe rocket techniques. A number of other scientists have successfully performed rocket experiments to characterize the *D*-region electron density [e.g., *Seddon et al.*, 1954; *Prakash and Pandey*, 1984; *Ulwick et al.*, 1988]. Although rocket-borne measurements of *D*-region electron density profile exhibit good accuracy and height resolution, one of the major drawbacks of using rockets is that the rocket exhaust modifies the chemical composition of the ionosphere [*Zinn and Sutherland*, 1980; *Pickett et al.*, 1985; *Bernhart et al.*, 2005]. Rocket sounding techniques thus cannot be used for the purpose of providing a reliable diagnostic above HAARP for use during ongoing experiments.

1.3.2 Incoherent Scatter Radar (ISR)

The technique to probe the ionosphere using ISR involves transmitting a high-power pulsed radio wave upward and recording the weak return that is scattered from the thermal, chemical, or turbulent components of the ionospheric plasma at ground-based receivers. The Radar Equation is applied to find the relationship between the received power and the transmitted power, in turn estimating the scattering cross section and

thus the electron density or electron concentration (N_e) [e.g., *Mathews*, 1984, 1986; *Chau and Woodman*, 2005]. The shape of the received power spectrum yields further information about the ionosphere in terms of N_e [*Sechrist*, 1974]. *Sechrist* [1974] argued that ISR measurements are quite accurate for electron densities down to the ledge or the steep gradient in electron densities between 80 and 90 km. Five-minute averages produced a statistical error as high as 50% for cases when the electron densities were of the order of 1000 cm^{-3}, which is typical at the highest D-region altitudes. ISR measurements thus provide important bounds for N_e at the highest D-region altitudes, but are clearly not suitable for performing high time-resolution quantification.

1.3.3 Ionosonde

Ionospheric diagnostics provided by the ionosonde consist of short pulse radio echoes over a broad range of HF frequencies. It is also known as 'swept-frequency pulse sounding' [*Hargreaves*, 1992]. These pulses are reflected at an altitude where the plasma frequency equals the wave frequency, and their echos are received at a ground based receiver. An ionogram is a graph of reflection height versus HF frequency, and under optimal conditions it represents a direct measure of the electron density as a function of altitude. The scale height is another important ionospheric characteristic that describes the shape of the ionospheric electron density profile. Ionosonde measurements have been used for the accurate determination of ionospheric effective scale heights [*Tulasi et al.*, 2009]. Although ionosonde measurements provide accurate electron density measurement in the upper regions of the ionosphere (E- and F-regions), this method typically produces no echo from within the D-region, due to the low electron densities at that altitude range [*Rishbeth and Garriott*, 1969].

1.3.4 Lightning as a Source for Remote Sensing

It is well known that the major portion of the radiation of electromagnetic energy from lightning discharges is in the VLF range [*Rakov and Uman*, 2003]. *Cummer et al.* [1998] showed that observations of ELF/VLF radio atmospherics or sferics made

by ground based receivers can be utilized to derive best-fit exponential D-region electron density profiles along the propagation path. *Cheng et al.* [2006] used a similar methodology of radio atmospherics to extract the nighttime D-region electron density profile along with a model for VLF propagation in the Earth-ionosphere waveguide. More recently, *Jacobson et al.* [2008], *Lay and Shao* [2011] performed VLF-LF ionospheric sounding of the D-region ionosphere using lightning radio emissions. Although these exponential profiles reflect the long-path averaged D-region electron densities, it remains to be seen whether they can provide more detailed information about the local D-region conditions near HAARP. It would be unrealistic to expect that enough lightning would occur at a specific time and be properly located to provide a usable localized diagnostic at HAARP during experiments.

1.3.5 HF Cross-Modulation

Cross-Modulation probing experiments have been widely used to determine the extent of ionospheric conductivity modulation in the D-region ionosphere. The method uses a sequence of precisely timed short, high-power disturbing pulses and short, low-power probing pulses, such that the probe pulse reflects from the F-region and as it propagates downwards, undergoes cross-modulation through the modified D-region, which in turn leads to a direct calculation of the virtual altitude of interaction. A number of scientists have extensively explored the heater-modified characteristics of the D-region ionosphere using measurements of cross-modulation experiments [e.g., *Weisbrod et al*., 1964; *Fejer*, 1970; *Senior et al*., 2010] . Recently, *Langston and Moore* [2013] demonstrated using HF cross-modulation during HF heating experiments at HAARP that it was possible to quantize the D-region absorption produced by HF heating both during the initial stages of heating and under steady-state conditions. Although, this gives an estimate of the extend of ionospheric conductivity modulation in the D-region, this methodology does not however provide details on the D-region structure.

1.4 Motivation

The effort of this work to characterize the properties of the D-region plasma are motivated by the fact that the D-region is the primary source of radio wave attenuation for waves propagating from the ground into space and vice versa. Characterizing the electrical properties of the D-region ionosphere is thus an important goal in the effort to understand the dynamic coupling of radio wave energy between the ground and space. HF heating provides a means to perform controlled ionospheric modification experiments.

Knowledge of the ambient D-region and thus the variable absorption taking place in the D-region is essential for understanding the mechanism of ELF/VLF generation and to improve the efficiency of wave generation. ELF/VLF waves can propagate for large distances of the order of the Earth's radius and find their application in global communication and navigation. Further, since ELF/VLF waves penetrate deep below the surface of the earth, they are useful for submarine communication and in imaging underground structures, e.g., in cave detection. Extensive work has also been performed using direct transmission of VLF waves from the ground to interact with radiation belt electrons in the magnetosphere.

Aside from the aforementioned direct applications of ELF/VLF wave generation, knowledge of the ambient D-region above HAARP is essential in understanding the physics that occurs at higher altitudes. Artificially-produced small-scale and large-scale structures in the plasma density in the E- and F-regions of the ionosphere known as 'Ionospheric Irregularities' present random temporal fluctuations in both amplitude and phase when received at an antenna, known as 'Ionospheric Scintillation' [e.g., *Djuth et al.*, 2006; *Hysell*, 2008; *Fallen et al.*, 2011]. Scintillation may cause problems that degrade the quality of the satellite navigation systems [e.g., *Milikh et al.*, 2008; *Kou et al.*, 2010]. Furthermore, scientists are interested in generating artificial emissions spectrally similar to the natural aurora by high power HF-heating of the bottom-side

F-region [e.g., *Kendall et al.*, 2010; *Holmes et al.*, 2011] and in understanding the mechanism of ion outflows related to artificial duct formation by HF heating in both the bottom- and top-side F-regions [*Milikh et al.*, 2010]. Many other types of higher altitude experiments are performed at HAARP, and in all cases, it is now imperative to have an understanding of the HF power that reaches these altitudes. The D-region diagnostic proposed in this work directly addresses these issues, and will be used to quantify the HF power that reaches E- and F-region altitudes.

Having provided a discussion of the previous efforts to characterize the D-region ionosphere, the drawbacks associated with them, and the motivation to perform HF heating experiments to characterize the D-region ionosphere, the following section briefly describes the approach used in this work towards the D-region characterization problem.

1.5 Approach

In order to characterize the ambient D-region ionosphere, this work utilizes ELF/VLF wave generation using dual-beam HF heating experiments. Ground-based experimental observations of ELF/VLF waves are interpreted in the context of a theoretical model. The ELF/VLF wave magnitude is identified as the property of the received ELF/VLF wave that is most sensitive to the effects of dual-beam HF heating. The dependence of the generated ELF/VLF wave magnitude on several HF transmission parameters (HF power, HF frequency, and modulation waveform) is then experimentally measured and analyzed in order to identify the dependence on the ambient D-region electron density (N_e) and/or electron temperature (T_e). It is shown that the power, frequency, and polarization of the CW HF beam (in addition to the type of amplitude modulation waveform used) provide independent information about the ambient D-region ionosphere. Furthermore, conditions under which the effects of N_e and T_e can be decoupled are determined theoretically by evaluating model predictions for numerous exponential electron density profiles with differing densities and slopes and

Figure 1-3. The HAARP HF heating facility. (Photo courtesy of Dr.Lee Synder.)

for numerous linear temperature profiles. Lastly, it is demonstrated that dual-beam ELF/VLF time-of-arrival (TOA) experiments provide additional key information about the ambient N_e profile. Using this information, we demonstrate that the ambient D-region electron density can be approximated using a piecewise-exponential N_e profile that is consistent with all observations to date.

The experimental work is carried out at HAARP, located in Gakona, Alaska. The geographic coordinates of the HF antenna array are approximately 62.39° N, 145.15° W. The facility is designed to transmit a narrow beam of high power radio signals in the 2.8 to 10 MHz frequency range. It has been shown that for HF frequencies $>$ 10 MHz, the absorption of HF radio waves gets progressively smaller. There are 180 towers

in a 12×15 rectangular grid with each tower supporting two pairs of crossed dipole antennas. Each active dipole element has a 10 kW transmitter, for a total of 3600 kW available for transmission. Figure 1-3 shows a picture of the HF antenna array. More technical information about the HAARP facility can be found at `http://www.haarp.alaska.edu/haarp/index.html`.

The HAARP array can be used to independently broadcast different HF frequencies simultaneously using a split-array configuration. The experiments presented in this work utilize the split-array configuration to perform dual-beam HF heating experiments and to assess the veracity of a multiple-beam ionospheric heating model. The dual-beam experiments performed consist of two HF beams simultaneously heating the lower ionosphere: while one beam modulates the conductivity of the lower ionosphere at ELF/VLF frequencies (AM), a second HF beam continually heats the same part of the lower ionosphere (CW), modifying the efficiency of ELF/VLF conductivity modulation and thereby the efficiency of ELF/VLF wave generation. The ELF/VLF waves generated are observed at various ground-based ELF/VLF receivers deployed by the University of Florida. Figure 1-4 shows the locations of HAARP and the receivers on the map of Alaska. Table 1-1 lists the receiver acronyms, latitude and longitude of each receiver site and HAARP, and their approximate distance (in km) from HAARP.

Table 1-1. Receiver Latitude, Longitude, and Distance (km) from HAARP.

Receiver Name	Latitude (N)	Longitude (W)	Dist. from HAARP (km)
HAARP	62.39°	145.2°	0
Oasis (OA)	62.35°	145.1°	3
Sinona Creek(SC)	62.58°	144.6°	33
Paradise(PD)	62.52°	143.2°	98

Figure 1-5 shows the ground-based ELF/VLF receiver system. Each receiver system consists of two orthogonal magnetic loop antennas oriented to detect the radial and azimuthal components of the magnetic field at ground level, a preamplifier, a line receiver, and a digitizing computer. Accurate timing is provided by a GPS clock.

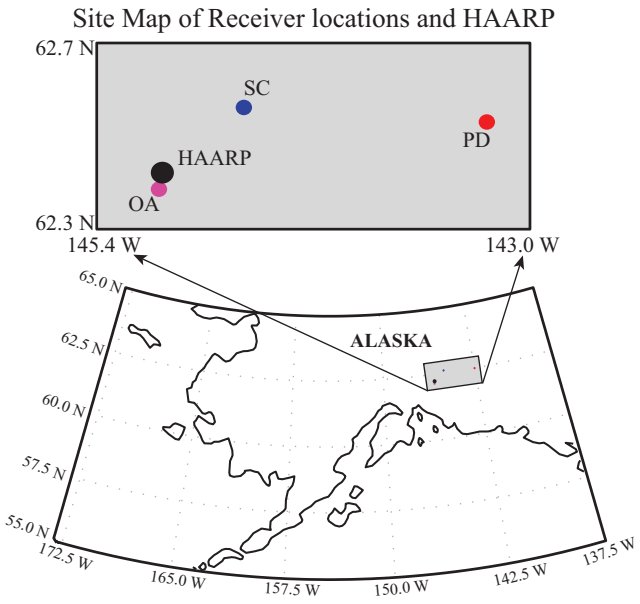

Figure 1-4. A map of Alaska, showing the receiver locations relative to the location of HAARP. Receiver acronyms and latitudes and longitudes are given in Table 1-1.

The receiver is sensitive to magnetic fields with frequencies between ∼300 Hz and ∼45 kHz. The ELF/VLF receiver has been rigorously tested to determine whether the observed ELF/VLF signals could be artificially created by non-linear demodulation of the high-power HF wave arriving at the receiver. If this were the case, one would expect to observe nonlinear effects on other ELF and VLF signals recorded in the data at the time of transmission, and these effects are not observed. For instance, modulation sidebands are not observed on VLF transmitter signals (in the 20-25 kHz range), and natural VLF signals do not exhibit evidence of receiver saturation or other nonlinearities, despite the fact that these signals are typically many times stronger than the ELF/VLF signals generated by modulated heating of auroral electrojet currents. Additionally, direct measurements of common-mode and differential-mode signal coupling also suggest that the observed ELF/VLF signals are generated by modulated heating of the auroral electrojet currents, rather than by nonlinear demodulation of the HF wave in the receiver electronics. Injected common-mode signals at 1.6 MHz were reduced by 40 dB compared to signals at 1 kHz, and common-mode signals at higher frequencies were

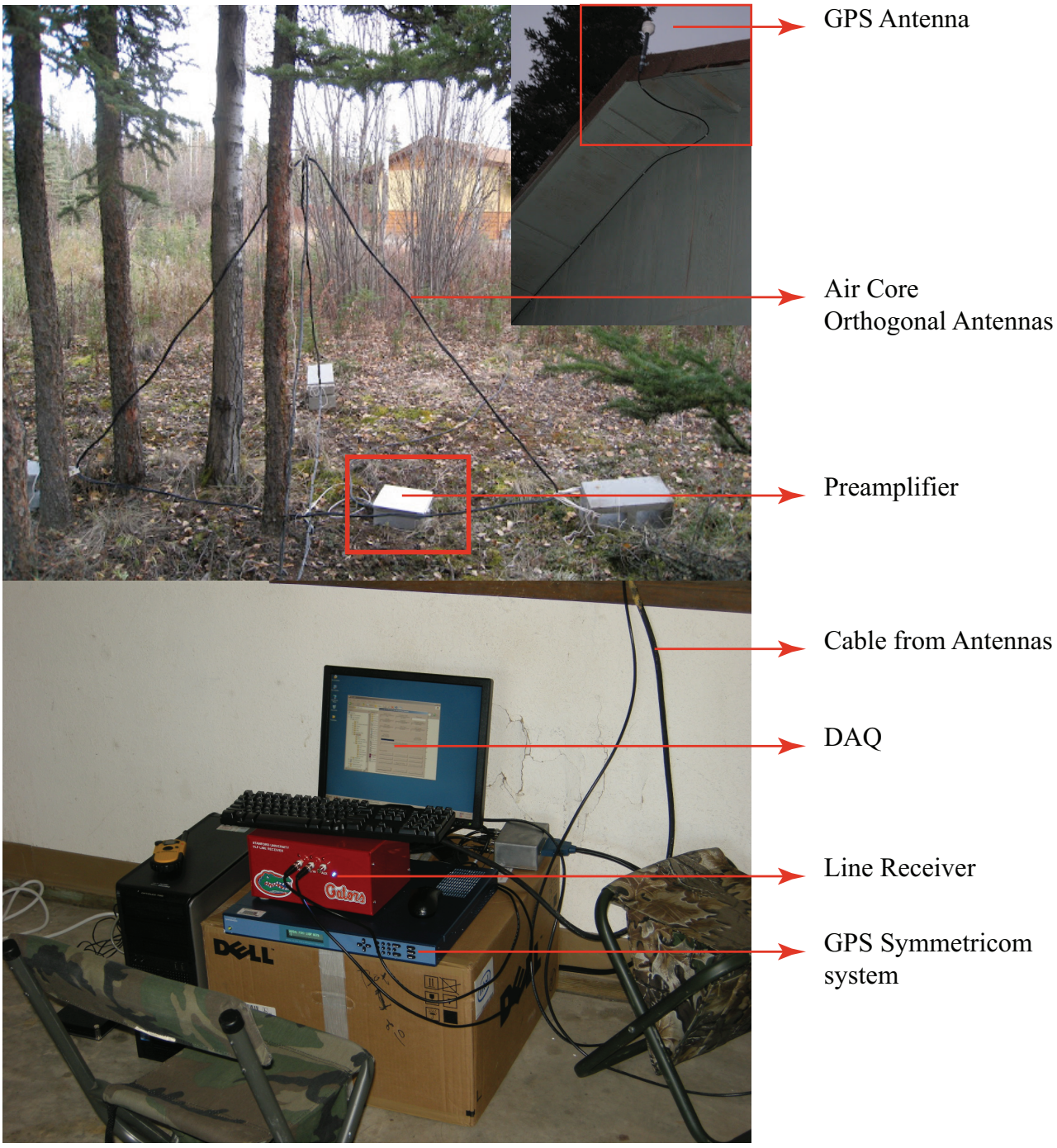

Figure 1-5. Receiver system deployed to measure radial and azimuthal B-fields. (Photo courtesy of Divya Agrawal.)

too small to be measured. Injected differential-mode signals measured at 1 MHz were reduced by 40 dB from the 1 kHz value. Higher frequency differential-mode signals were also too small to measure accurately. Except where noted, the amplitudes and phases

of the ELF/VLF tones at the modulation frequencies and their harmonics are determined in post-processing using discrete Fourier transforms.

Having provided the background, historical review of past *D*-region probing experiments, motivation, and approach to characterize the *D*-region of the ionosphere, the remainder of this work is organized as follows: Chapter 2, describes the implementation of multi-beam HF heating; Chapter 3 identifies the ELF/VLF magnitude as the ELF/VLF wave property most sensitive to additional CW heating; Chapter 4 critically investigates the dependance of ELF/VLF waves on CW heating as a function of HF-power, HF frequency, modulation waveform, and receiver location; Chapter 5 demonstrates that the dual-beam experiment is sensitive to structure within the *D*-region ionosphere; and Chapter 6 summarizes the presented material and suggests further efforts in this area.

1.6 Scientific Contributions

The following scientific contributions are demonstrated in this work:

1. A multi-beam HF ionospheric heating model has been tested and validated using observations at HAARP. The functionality of the multi-beam HF heating model has been successfully extended to account for five different AM waveforms, namely square, sinusoidal, square-root-sine (sqrt-sine), triangle, and saw-tooth. The model has also been extended to account for both X- and O-mode polarization of the CW beam.

2. It has been experimentally established that the magnitude of ELF/VLF wave generation is the parameter most sensitive to additional CW heating.

3. The transmission parameters that provide independent information about the ambient *D*-region ionosphere during dual-beam heating experiments have been experimentally identified. These transmission parameters are : 1) the CW power levels, 2) the frequency of the HF CW beam, 3) the modulation waveform, and 4) the polarization of the HF CW beam.

4. In the context of the HF heating model, it has been demonstrated that observations performed during the dual-beam heating experiment are sensitive to structure within the *D*-region ionosphere. Piecewise-exponential electron density approximations appear to adequately match all available observations.

CHAPTER 2
DUAL-BEAM ELF/VLF WAVE GENERATION: MODEL IMPLEMENTATION

This chapter provides a description of the multi-beam HF heating model that is utilized to provide the model predictions in Chapters 3, 4, and 5 of this dissertation. The extension of this multi-beam HF heating model to account for five different AM waveforms, X-, and O-mode polarization of the CW beam is also described.

2.1 Numerical Analysis

The ELF/VLF wave generation model presented herein is implemented using two distinct calculations: 1) a multiple-HF-beam ionospheric heating model is used to calculate the full time-evolution of the ionospheric conductivity modulation as a function of space, and 2) a simple radiation model is employed to calculate the electromagnetic fields at the receiver. This section provides a discussion of each of these calculations.

2.1.1 Multi-Beam HF Heating Model

The multiple-HF beam ionospheric heating model is based on the single-beam HF heating model provided by *Moore* [2007], which has been used to successfully model ground-based ELF/VLF observations in a number of works [e.g., *Payne et al.*, 2007; *Lehtinen and Inan*, 2008; *Fujimaru and Moore*, 2011a]. Given a set of ionospheric profiles, including electron density and electron temperature height profiles, and given the parameters of the HF heating beam, such as the HF frequency, HF polarization, HF beam pattern, modulation frequency, and HF power, the model predicts the time-variation of electron temperature as a function of altitude within the highly collisional D-region ionosphere. The model accounts for the self-absorption of the HF wave [e.g., *Tomko*, 1981] as well as for nonlinear electron energy losses [e.g., *Rodriguez*, 1994]. It neglects a number of ionospheric processes that are important at higher altitudes (but that are presumably less important in the D-region), such as electron density changes that may result from long-term HF heating. The resulting variation in electron temperature is used to calculate the full time-evolution of the

so-called Hall, Pedersen, and Parallel conductivities, from which the amplitudes and phases of conductivity modulation at the modulation frequency and its harmonics are extracted.

The ambient electron density and temperature profiles used throughout this work are as shown in Figure 2-1. These profiles have been extensively used in previous ELF/VLF wave generation analyses [e.g., *Moore et al.*, 2007; *Agrawal and Moore*, 2012; *Moore and Agrawal*, 2011]. The electron densities (panel A of Figure 2-1) represent tenuous (I) to dense (III) ionospheric conditions, with electron density changes by factors of 10 at 80 km altitude. The electron temperature profiles shown in panel B of Figure 2-1 are representative of a year-long survey of electron temperature profiles provided by the MSISE-90 Atmosphere Model hosted by NASA at `http://ccmc.gsfc.nasa.gov/modelweb/`[*Labitzke et al.*, 1985; *Hedin*, 1991].

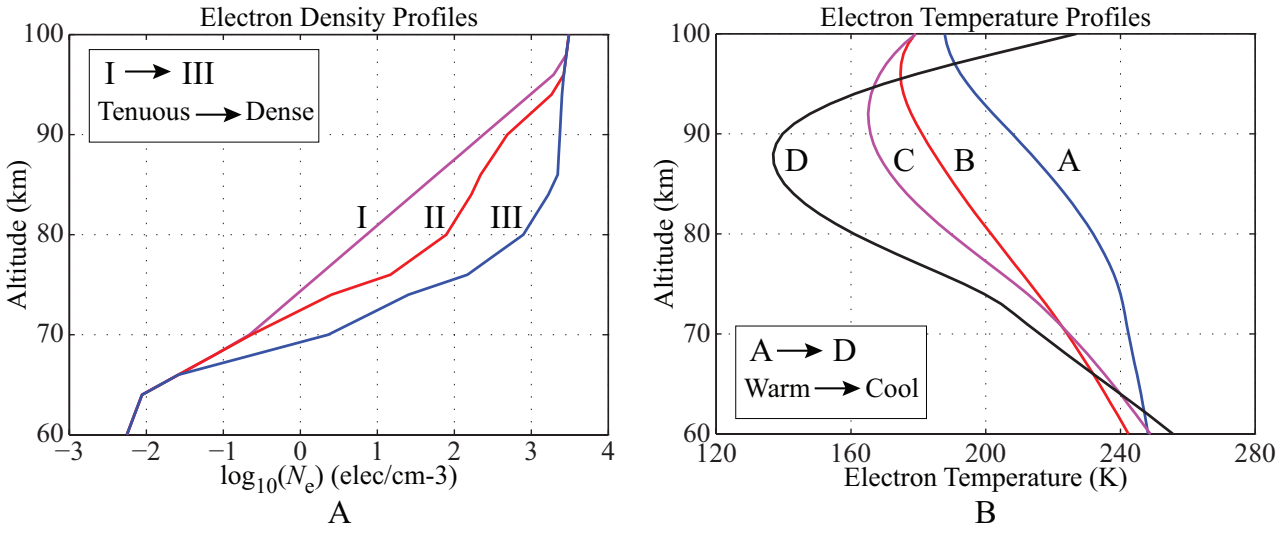

Figure 2-1. *D*-region (A) Ambient Electron Density profiles (B) Ambient Electron Temperature profiles as a function of altitude.

In multibeam-HF heating experiments, the 12 $\times$15 HAARP antenna array (Section 1.5) is utilized in a split-array configuration. This dissertation focuses on dual-beam HF heating. Table 2-1 lists the HF heating beam parameters used as inputs to the dual-beam (6 $\times$15 array) HF-heating model throughout this work.

Table 2-1. List of 6 $\times$15 HF sub-array parameters used as input to the model. Acronyms used are: BW: Beam width, NS: North-South, EW: East-West, HPBW: Half Power Beam Width, ERP: Effective Radiated Power

HF-Beam	HF Frequency (MHz)			
Parameters	3.25	4.5	5.8	6.9
BW_{NS} (°)	37.90°	27.70°	21.50°	18.00°
BW_{EW}(°)	13.90°	9.90°	7.60°	6.40°
$HPBW$ (°)	23.12°	19.67°	12.81°	10.75°
Max ERP (dB W)	78.9	84.2	86.4	87.9

The model is ray-based, meaning that a large number of rays are used to calculate the spatial extent of conductivity modulation. With a large enough number of runs, any HF radiation pattern may be modeled including side-lobes, for instance. The top-left and top-right panels of Figure 2-2 are illustrative examples of the 3-D beam patterns and the corresponding 2-D slice of the HF power patterns for the individual split North 6 $\times$15 array at 3.25 MHz . The middle panel shows the 3-D beam patterns and the corresponding 2-D slice of the HF power patterns from the South 6 $\times$15 array operating at 5.8 MHz. In multibeam-HF heating, the frequency combinations are chosen such that the HF frequency of the CW beam is always smaller than that of the modulated beam, so that the modulated region is completely bathed within the CW heated region. The bottom panel shows the 3-D dual-beam pattern for the split north-south array.

Typically, the total number of model evaluations can be reduced by casting the system as cylindrically symmetric, although it is not necessary to do so, as has been demonstrated [*Payne et al.*, 2007]. In a cylindrically symmetric system, the Earth's magnetic field is oriented perpendicular to the Earth's surface at HAARP ($\sim$15° zenith angle in reality), and this is a good approximation for D-region ohmic heating. The HAARP HF heating array is not cylindrically symmetric, however, particularly when 6x15 sub-arrays are utilized, as is the case in this work. In order to approximate the system as cylindrically symmetric, the widths of the HF beam in the North-South and East-West directions are used to define a solid angle, and an effective cylindrically symmetric beam

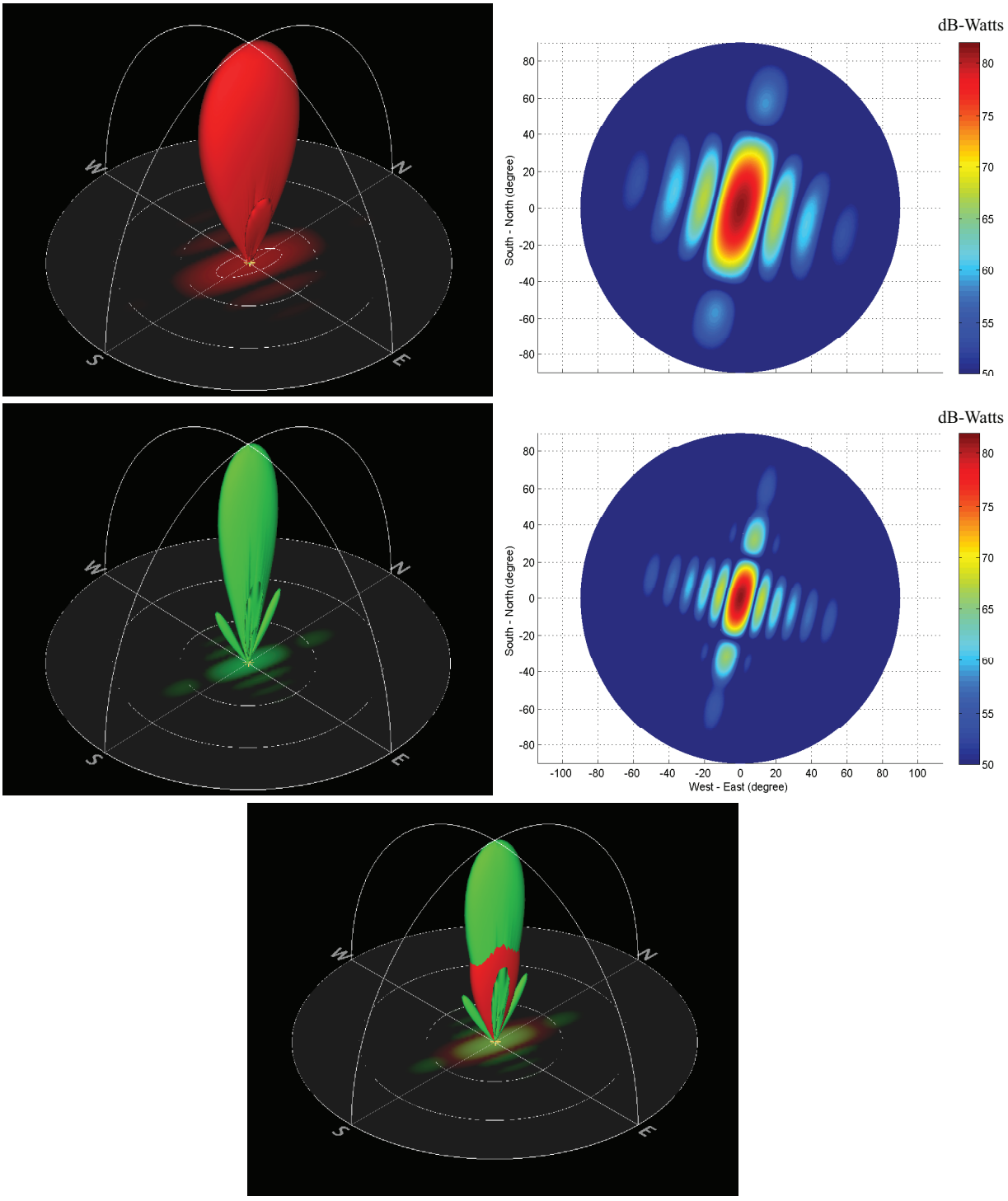

Figure 2-2. 3-D beam pattern and corresponding 2-D slices of the HF power patterns from HAARP for vertical transmissions at HAARP for (top panel) 3.5 MHz, (middle panel) 5.8 MHz and (bottom panel) 3.25 - 5.8 MHz split array (dual-beam transmission). Note that the 3-D beam pattern for the dual-beam transmission looks distorted because the 3.2 MHz beam (top panel) is lower gain (so lower total power) than the 5.8 MHz beam (middle panel) and is partially hidden.

width is chosen such that it produces the same solid angle. This choice has the effect of producing approximately the same total volume of modulated currents.

2.1.2 Temperature Modulation

The following section describes the modifications made to the single-beam HF heating model [*Moore et al.*, 2007] to create a new multiple-beam heating model; and the validity of the new assumptions are evaluated. While the implementation accounts for only two HF beams, the assumptions built in to this system are identical to those needed for a system consisting of more than two HF beams. This analysis, therefore, may be easily expanded to accommodate any larger number of HF beams.

The two primary nonlinearities involved in the modulation of the D-region electron temperature, HF self-absorption and non linear electron energy loss rates, are combined within the well-known electron energy balance equation given in Equation 2–1 [e.g., *Huxley and Ratcliffe*, 1949; *Maslin*, 1974; *Stubbe and Kopka*, 1977; *Tomko*, 1980; *Rietveld et al.*, 1986; *Rodriguez*, 1994]. For a single HF beam, the energy balance equation may be stated:

$$\frac{3}{2} N_e \kappa_B \frac{dT_e}{dt} = 2k\chi(T_e)S - L(T_e, T_0) \tag{2–1}$$

where N_e is the altitude-dependent electron density, κ_B is Boltzmann's constant, T_e is the time-varying local electron temperature, k is the HF free-space wave number, $\chi(T_e)$ is the temperature-dependent rate of absorption in the plasma (the imaginary part of the refractive index, n), S is the time-varying power density of the HF wave, and L is the sum total of all electron energy loss rates, which depend in general on both the ambient electron temperature T_0 and the time-varying electron temperature T_e. Energy losses due to elastic collisions [*Banks*, 1966] with rotational [*Mentzoni and Row*, 1963; *Dalgarno et al.*, 1968], and vibrational [*Stubbe and Varnum*, 1972; *Prasad and Furman*, 1973] excitation of molecular nitrogen and oxygen are taken into account in the model. This equation neglects any time variation in the electron density, and also neglects heat

conduction as well as convection, as is typical for ELF/VLF wave generation models. Convection in particular is usually neglected considering the $\sim$1-millisecond timescale for ELF/VLF wave generation.

When accounting for two HF beams, the electron energy balance equation requires an additional term:

$$\frac{3}{2}N_e\kappa_B\frac{dT_e}{dt} = 2k_1\chi_1(T_e)S_1 + 2k_2\chi_2(T_e)S_2 - L(T_e, T_0) \tag{2–2}$$

where the subscripts, 1 and 2, identify quantities that depend on the HF beam. This additional term represents the energy absorbed by the local medium from a second HF wave. Similarly, if the number of HF beams is M, the electron energy balance equation may be written:

$$\frac{3}{2}N_e\kappa_B\frac{dT_e}{dt} = \sum_m^M 2k_m\chi_m(T_e)S_m - L(T_e, T_0) \tag{2–3}$$

where the energy locally absorbed by the plasma from each of the M waves is contained within the summation term.

The HF heating model simultaneously and self-consistently accounts for wave absorption as it calculates the trajectory of the HF ray paths (i.e., as it performs ray tracing). When accounting for multiple HF ray paths, it becomes clear that the frequency-dependent refraction and group velocity of the waves within the ionosphere will cause HF rays at different frequencies to become both spatially and temporally separated. It is thus the case that any two HF waves at different frequencies that are transmitted at the same time and with the same initial trajectory will in general separate in both space and time as a function of propagation distance. It is assumed that these effects are negligible for HF propagation below 100 km altitude.

In order to evaluate this assumption, the temporal and spatial separation of HF beams at 3.25 and 4.5 MHz at an altitude of 100 km for initial HF ray angles varying from 0–30° zenith angle is found for the twelve possible combinations of electron density and electron temperature profiles shown in Figure 2-1. Among all of the various

combinations of electron density and electron temperature profiles, the maximum lateral spatial separation at 100 km altitude is calculated to be 72 meters, and the maximum temporal separation is calculated to be 0.8 microseconds. For the purposes of evaluating the generation of ELF/VLF conductivity modulation within the D-region ionosphere, these separation values are not likely to be significant. For this reason, the multiple-beam HF ionospheric heating model calculates the trajectory and timing of each ray path independently, but assumes the rays to be co-located for the purposes of evaluating ionospheric heating and HF wave absorption.

It is notable that the dual-beam HF heating model does not automatically account for long-term changes in electron density. These changes are expected to occur on time scales much larger (by a factor $>\sim$1000) than the approximately millisecond time scales of ELF/VLF waves of importance to this work (1-3 kHz). For reference, the theoretical work presented by *Milikh and Papadopoulos* [2007] predicts an electron density change by a factor of $\sim$2 under long-term HF heating conditions.

2.1.3 Conductivity Modulation

The electron temperature modulation is related to the conductivity modulation through a nonlinear relationship. The conductivity tensor is most commonly given by Equation 2–4 [*Tomko*, 1981; *Bittencourt*, 1986; *Moore*, 2007].

$$\bar{\bar{\sigma}} = \begin{bmatrix} \sigma_P & -\sigma_H & 0 \\ \sigma_H & \sigma_P & 0 \\ 0 & 0 & \sigma_{||} \end{bmatrix} \tag{2–4}$$

where σ_P, σ_H, and $\sigma_{||}$ denote the Pedersen, Hall, and Parallel conductivities, respectively.

$$\sigma_P = \frac{4\pi q_e^2}{3m_e} \int_0^\infty \frac{\nu_{av} {v_e}^3}{{\nu_{av}}^2 + {\omega_{ce}}^2} \frac{\partial f_{e,0}}{\partial v_e} dv_e \tag{2–5}$$

$$\sigma_H = \frac{4\pi q_e^2}{3m_e} \int_0^\infty \frac{\omega_{ce} v_e^3}{{\nu_{av}}^2 + {\omega_{ce}}^2} \frac{\partial f_{e,0}}{\partial v_e} dv_e \tag{2–6}$$

$$\sigma_{||} = \frac{4\pi q_e^2}{3m_e} \int_0^\infty \frac{v_e^3}{\nu_{av}} \frac{\partial f_{e,0}}{\partial v_e} dv_e \tag{2–7}$$

where q_e is the electron charge, m_e is the electron mass, ω is the angular frequency, ν_{eff} is the effective electron-neutral collision frequency, ω_{ce} is the cyclotron frequency and $f_{e,0}$ is the Maxwellian electron velocity distribution function.

Tomko [1981] and *Bittencourt* [1986] (pg. 172) provide a detailed discussion on the '*Maxwell-Boltzmann*' or '*Maxwellian velocity distribution function*' which is given by:

$$f_{e,0} = N_e \left(\frac{m_e}{2\pi\kappa_B T_e} \right)^{3/2} \exp\left(\frac{-m_e v_e^2}{2\kappa_B T_e} \right) \tag{2–8}$$

where N_e is the number density of electrons, v_e is the electron velocity, κ_B is *Boltzmann's* constant, and T_e is the electron temperature.

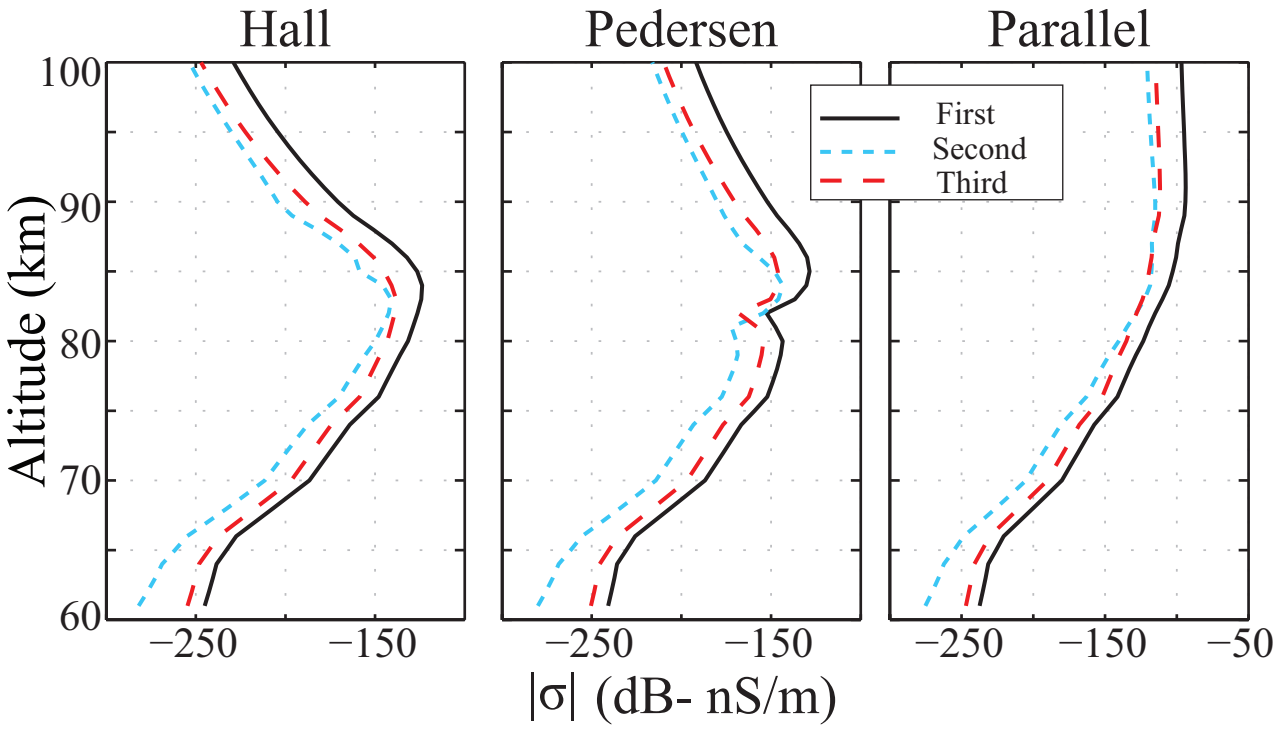

Figure 2-3. Amplitudes of First, Second and Third harmonics for Hall, Pedersen and Parallel conductivities. The model predictions are for f_c 3.25 MHz, Modulated f_c, 5.8 MHz, at max CW ERP, 100% peak power of modulated beam using III-D profile.

Figure 2-3 represents illustrative examples of the amplitude of the first, second and third harmonics of the three components of the conductivity modulation tensor. Hall conductivity shows altitudes of maximum conductivity modulation between 80 and 85 km, which represents the dominant source altitude. The Pedersen conductivity shows two regions of increased conductivity modulation with the dominant source region at $\sim$85 km. While the Parallel conductivity has the strongest amplitude at higher altitudes compared to Hall and Pedersen, this quantity conveniently cancels for ground-based observations as we will see in Secion 2.2.

2.2 Radiation

In order to calculate the magnitude of the electromagnetic wave at the receiver, the Hall, Pedersen, and Parallel currents in the ionosphere are calculated. The amplitudes and phases of the conductivity modulation calculated using the dual-beam HF heating model are interpolated onto a regular rectangular grid with 1-km spacing (Figure 2-4) and multiplied by the electric field of the auroral electrojet. The spatial distribution of the electrojet field is assumed to be constant throughout the D-region and oriented parallel to the ground, consistent with past theoretical work and experimental observations [e.g., *Banks and Doupnik*, 1975; *Stubbe and Kopka*, 1977; *Papadopoulos et al.*, 2003; *Payne*, 2007]. The model inherently accounts for the group delays of the HF waves to each of the ionospheric grid points and also accounts for the temporal reaction of the plasma to the high-power HF signals. Both of these effects modify the phase of the ELF source currents as a function of space. Because the experimental observations performed are all relative observations, the actual magnitude of the electrojet field strength does not matter in our case.

Complications arise when one considers that D-region heating by the electrojet currents themselves may affect the amplitude of the radiated ELF fields, however. It is a good assumption that the electrojet field strength can vary between 5 and 100 mV/m [e.g., *Banks and Doupnik*, 1975; *Stubbe et al.*, 1981; *Papadopoulos et al.*,

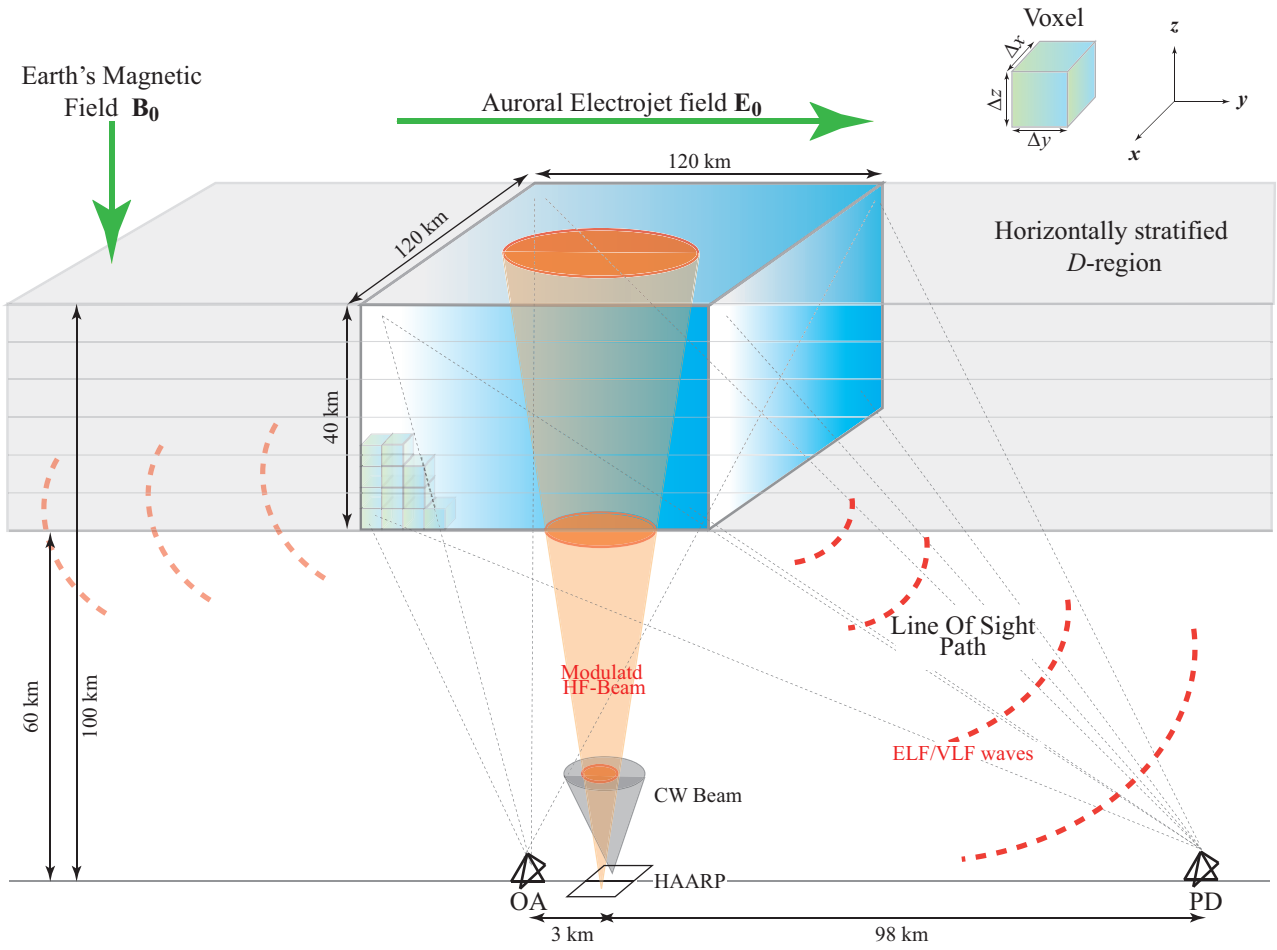

Figure 2-4. 3-D modulated heated region (orange cone: Modulated heated region, gray: CW heated region) and the rectangular cuboid (blue). The green voxels, represent the volume element onto which the amplitudes and phases of conductivity modulation are interpolated.

2003; *Payne*, 2007]. Figure 2-5 indicates that the conductivity modulation produced by modulated HF heating together with a 5 mV/m electrojet field strength is less than 0.2-dB different than that calculated with a 100 mV/m electrojet field. It is thus a good approximation to assume that the ELF source currents vary linearly with the electrojet field strength. Although this model assumes that the electron energy distribution remains Maxwellian throughout the heating process, the minimal impact of electrojet heating on the calculated conductivity modulation indicates that this assumption is likely to be valid even for fully kinetic models.

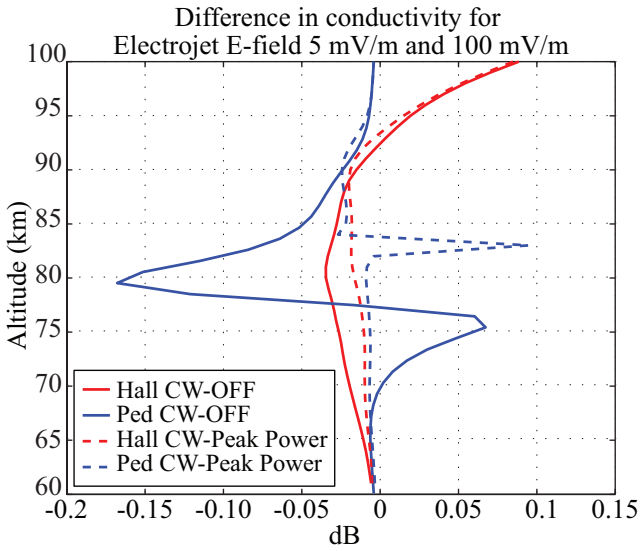

Figure 2-5. The dB difference in conductivity modulation as a function of altitude for a 5-mV/m and a 100-mV/m electrojet electric field.

With the distribution of ionospheric ELF source currents in hand, the magnetic field is calculated for a given ground-based receiver location assuming that the ELF source takes the form of spatially-distributed set of dipoles over a ground plane [e.g., *Payne*, 2007]. For receiver locations within ∼75 km of HAARP, this is a good approximation: *Payne* [2007] demonstrated that within ∼75 km of HAARP the magnitude of the magnetic field calculated using a distributed dipole model closely matches that calculated using a more complete model that accounts for Earth-ionosphere waveguide effects and for the secondary ionospheric currents generated during the modulated heating process. In order to mitigate the errors associated with neglecting these effects, the observations are normalized to the magnetic field observed during CW-OFF periods. This normalization cancels the effects of the Earth-ionosphere waveguide and the varying electrojet field strength to first order [*Barr and Stubbe*, 1993], allowing for the direct comparison of observations and modeling results. It should be noted, however, that the effects of the Earth-ionosphere waveguide are important. For instance, pronounced waveguide resonances at multiples of ∼2 kHz have been observed in ELF/VLF amplitude data [e.g., *Stubbe et al.*, 1982; *Barr and Stubbe*, 1984; *Rietveld*

et al., 1989], and multiple ionospheric reflections have been directly observed during ELF/VLF pulsed-heating experiments [e.g., *Papadopoulos et al.*, 2005; *Fujimaru and Moore*, 2011a]. *Fujimaru and Moore* [2011a], showed via TOA (Time of Arrival) that the line of sight path contribution can be separated from the first ionospherically reflected component using chirped-frequency modulation. It is very clearly the case that the Earth-ionosphere waveguide affects the amplitude and phase of the ELF/VLF signal received on the ground. In this dissertation, we use the normalized ELF/VLF B-fields.

Because we present only normalized field values in this dissertation, it is worth noting that this model is fully capable of predicting absolute field strengths. For the profiles shown in Figure 2-1, and for reasonable (5–100 mV/m) values of the electrojet field strength, the magnetic field magnitudes predicted at a receiver located $\sim$33 km from HAARP vary from $\sim$40 fT to $\sim$20 pT (Figure 2-6), which are very reasonable field values compared to past and present experimental observations [e.g., *Stubbe et al.*, 1982; *Rietveld et al.*, 1986, 1989; *Villasenor et al.*, 1996; *Cohen et al.*, 2010]. The range of possible field values can be easily extended using a greater variety of ionospheric profiles. As mentioned above, however, absolute field measurements depend on Earth-ionosphere waveguide effects, on the generation of secondary ionospheric currents, and on the strength of the electrojet currents, in addition to the conductivity modulation produced by HF heating. In order to isolate the effects of HF heating, this dissertation exclusively presents normalized field observations.

For the given assumptions, the magnitude of the predicted ELF/VLF B-field on the ground is given by $\sqrt{B_H^2 + B_P^2}$, where B_H and B_P are the amplitudes of the B-fields generated by the Hall and Pedersen currents, respectively. The assumption that the Earth's magnetic field is perpendicular to the ground means that the parallel conductivity is also perpendicular to the ground. As a result, the radial and azimuthal components of the the direct-path and ground-reflected B-fields generated by the parallel conductivity cancel, and the parallel B-field does not play a role in the predicted ELF/VLF magnitude.

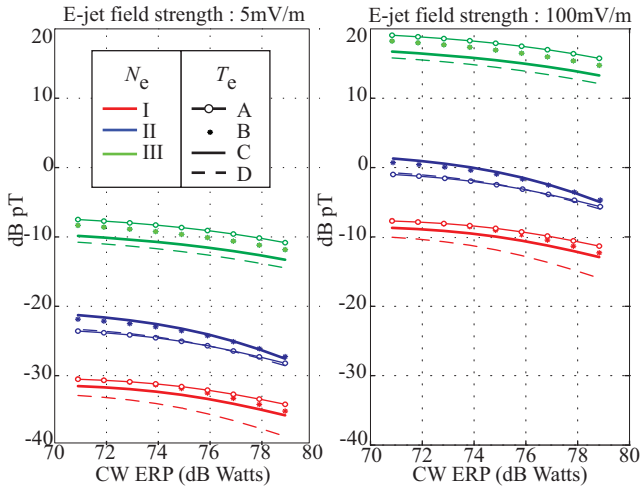

Figure 2-6. Absolute magnetic field strength at Sinona Creek (SC) for electrojet field of 5mV/m and 100 mV/m.

The quantity is conveniently independent of the orientations of the receiver antennas. It is useful to inspect the effect of CW heating on the generation of the Hall and Pedersen B-fields independently, however. Even for realistic B-field directions (15° off-zenith at HAARP), the parallel conductivity does not contribute to the magnitude under the assumption that the high conductivity in the direction of the magnetic field cancels out the modulated currents in that direction [*Cohen et al.*, 2012].

Figures 2-7 and 2-8 show the first harmonic amplitudes of the B-fields generated by the Hall and Pedersen currents as a function of space within the lower ionosphere with a 1-km grid spacing. The colors represent the amplitude (in dB) of the ELF/VLF wave observed at the receiver and generated by a dipole at the plotted location. The left hand panels show the field amplitudes generated under modulated single-beam heating conditions (CW-OFF; sinusoidal AM at 4.5 MHz, X-mode), and the right hand panels show the field amplitudes generated under dual-beam heating conditions (CW-ON at 3.25 MHz, X-mode; sinusoidal AM at 4.5 MHz, X-mode). Results are shown as a function of electron density, from Profile I (top) to Profile III (bottom), for a single electron temperature profile (Profile B). Figures depicting the dependence on the electron temperature profile (not shown) demonstrate essentially the same spatial distribution

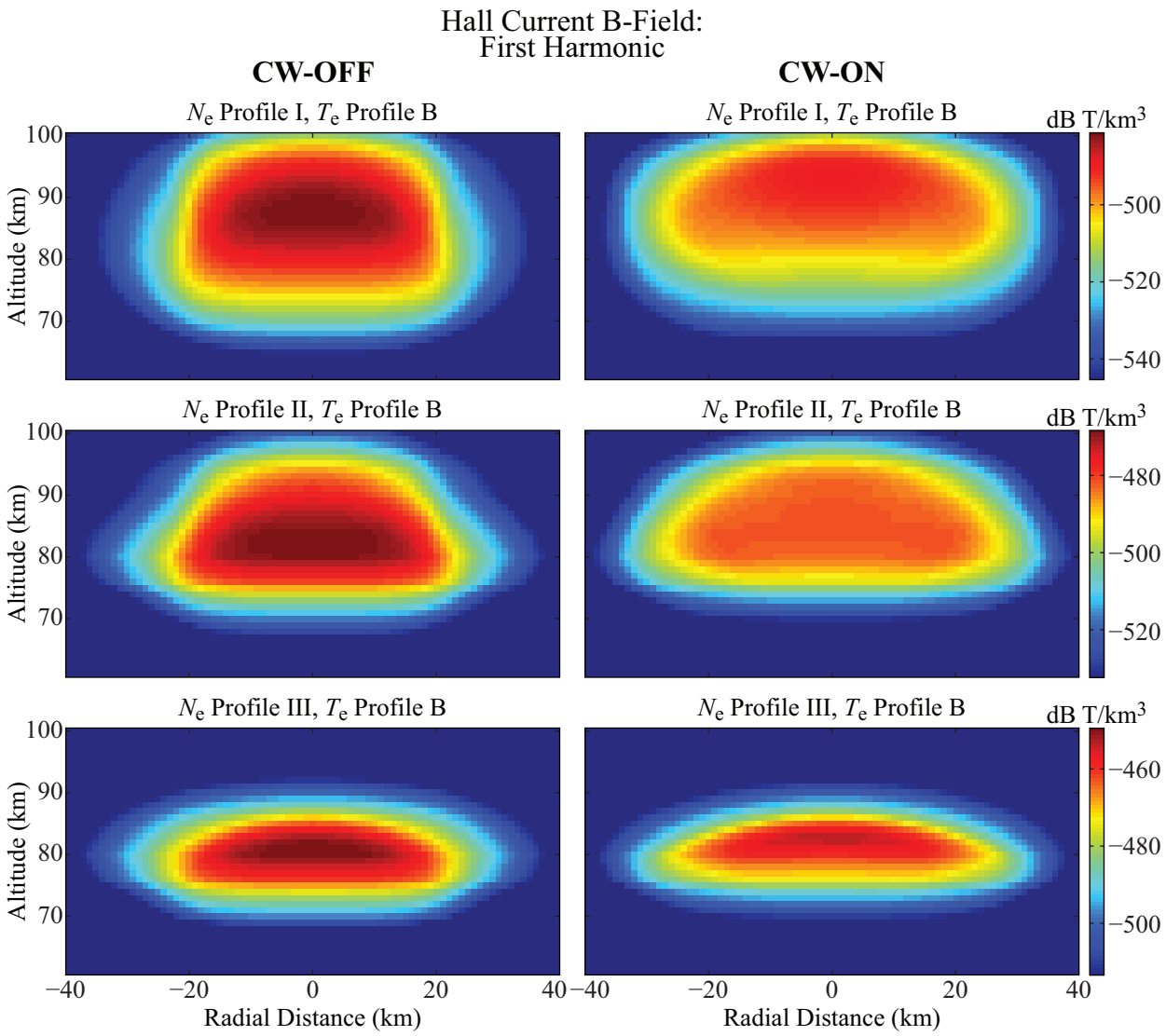

Figure 2-7. Numerical predictions. First harmonic (1215 Hz) Hall current B-field amplitudes as a function of source location. CW-ON and CW-OFF periods are shown as a function of electron density profile.

of fields shown here, although the absolute magnitudes are different. We note that the spatial distribution of the B-fields shown is essentially cylindrically symmetric. In this case, the symmetry results from the fact that the receiver is located very close to (1.5 km from) the origin, in addition to the fact that the condition of cylindrical symmetry was enforced in the calculation of the conductivity modulation. For instance, plots calculated for a receiver distant from HAARP would show higher amplitudes in the direction of the receiver.

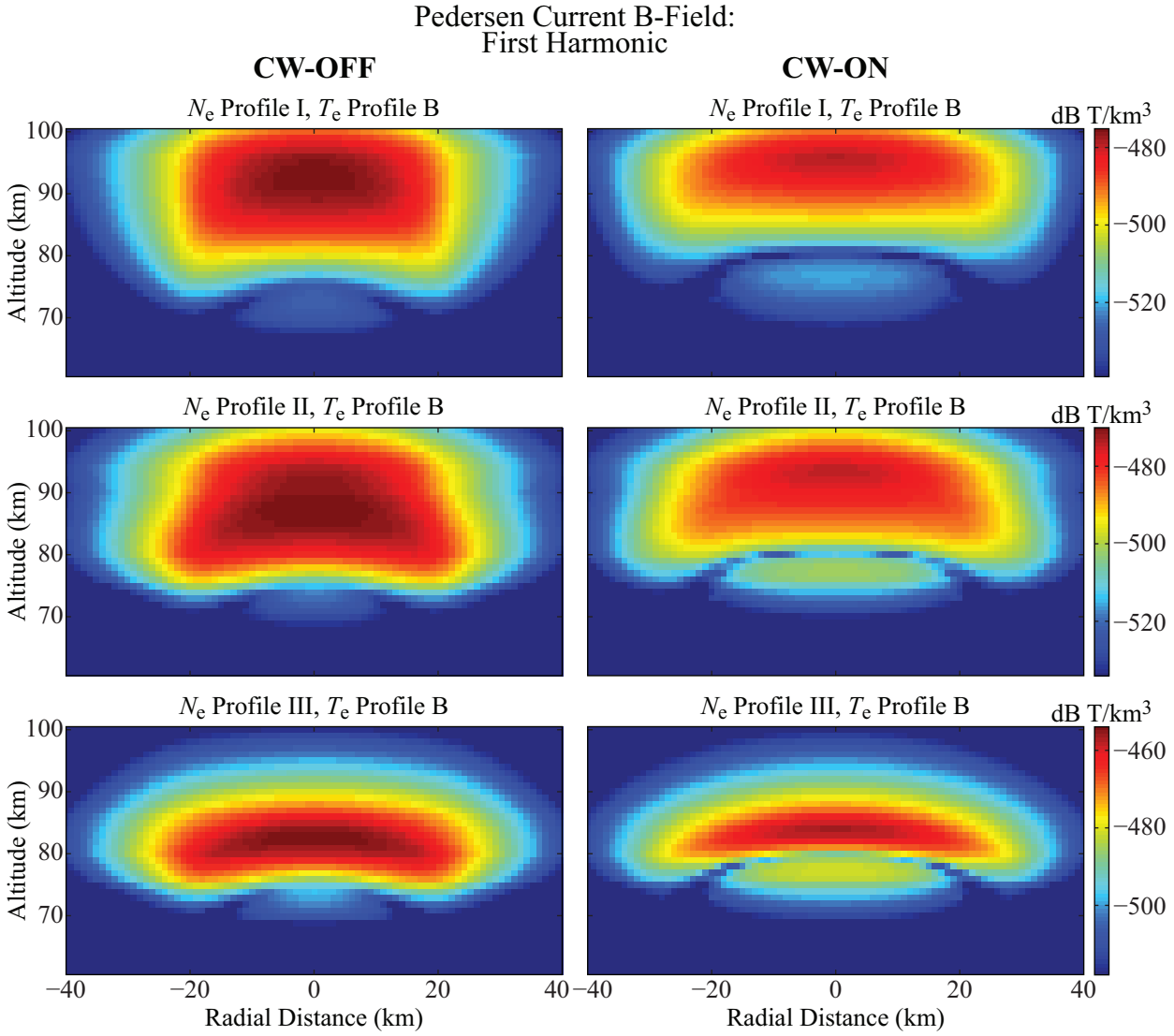

Figure 2-8. Numerical predictions. First harmonic (1215 Hz) Pedersen current B-field amplitudes as a function of source location. CW-ON and CW-OFF periods are shown as a function of electron density profile.

Figures 2-7 and 2-8 demonstrate a pronounced dependence on the electron density profile. Under both CW-OFF and CW-ON conditions, the spatial distribution of both Hall and Pedersen currents becomes more compact in altitude as the electron density varies from Profile I to Profile III. Additionally, the altitude of the peak amplitude decreases significantly (by $\sim$5 km per profile) and the peak amplitude itself increases sharply (by $\sim$15 dB per profile) as the electron density varies from Profile I to Profile III. A detailed

analysis on the affects of electron density and electron temperature profiles is provided in Chapter 4.

The dependence on CW-heating is also very clearly depicted in Figures 2-7 and 2-8. In all cases, the addition of a high-power CW heating beam “pushes” the wave generating currents upwards and outwards. The average altitude of wave generation increases, and the volume of radiating currents decreases at lower altitudes while at the same time increases at higher altitudes. A detailed analysis of this affect is discussed in Chapter 5. The B-field amplitudes are dramatically reduced at lower altitudes, but in some cases they increase slightly at higher altitudes. In all cases, the peak amplitude decreases under CW-ON conditions. Figures 2-7 and 2-8 demonstrate that under a variety of electron density and electron temperature (not shown) conditions, additional CW heating at peak power will tend to reduce the magnitude of the ELF/VLF B-field received on the ground.

Figures 2-9 and 2-10 shows the spatial distribution of the second harmonic components of the Hall and Pedersen currents for comparison with the first harmonic components. It is notable that during CW-OFF periods, the spatial distribution of the second harmonic of the Hall B-field is very similar to that of the first harmonic, although the second harmonic of the Pedersen B-field is somewhat lower in altitude than the first harmonic. During CW-ON periods, however, the second harmonic of the Hall B-field is “pushed” higher in altitude than the first harmonic, whereas the spatial distribution of the second harmonic of the Pedersen B-field is very similar to that of the first harmonic. It is thus the case that during both CW-ON and CW-OFF periods, there is at least one major component of the ELF/VLF magnitudes that has a very similar spatial distribution for both the first and second harmonic, indicating that the ELF/VLF second to first harmonic ratio naturally minimizes second order effects as well as first order effects. A more detailed analysis on the ELF/VLF harmonic ratio is discussed in Chapter 3.

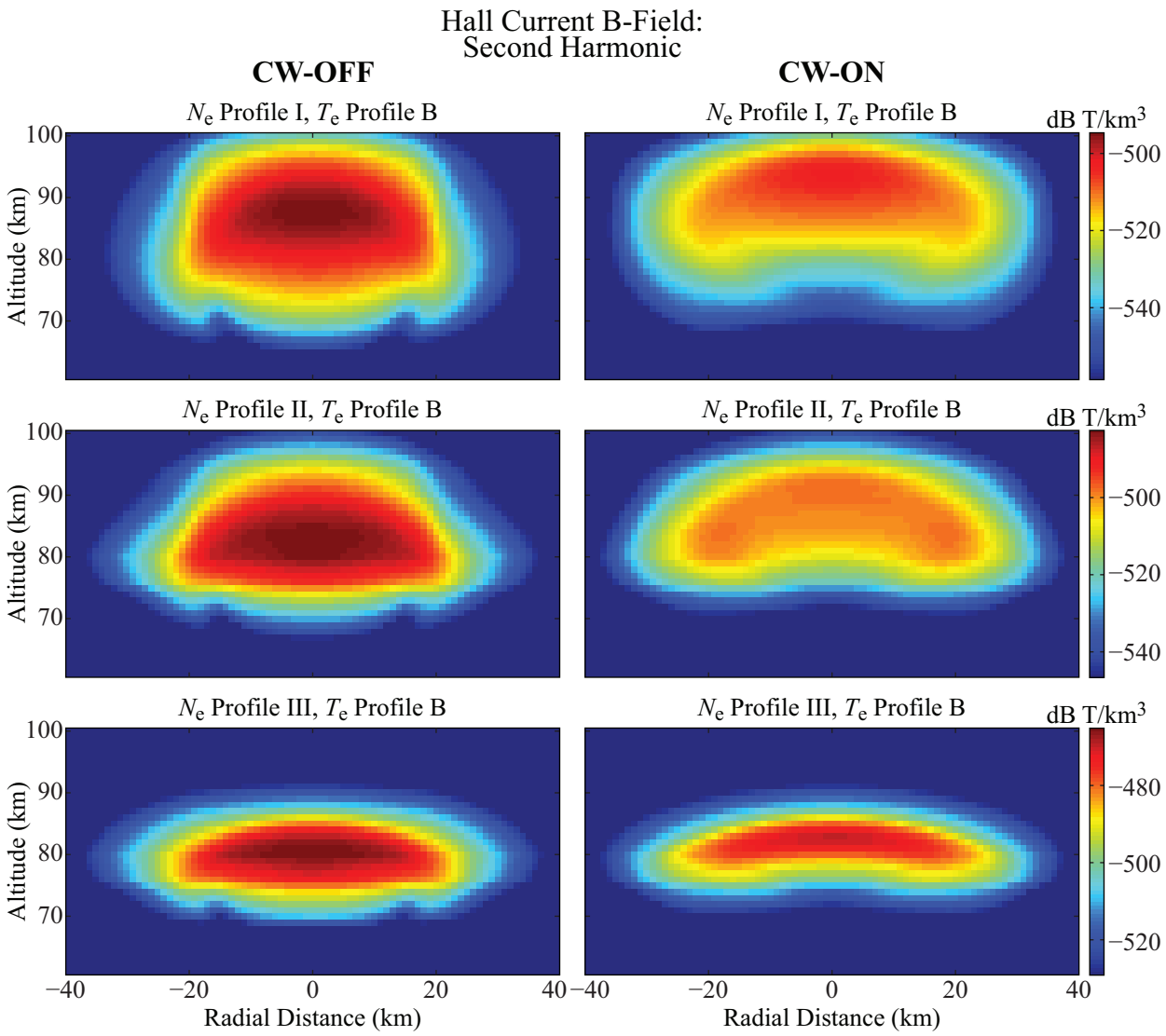

Figure 2-9. Numerical predictions. Second harmonic (2430 Hz) Hall current B-field amplitudes as a function of source location. CW-ON and CW-OFF periods are shown as a function of electron density profile.

Having provided a description of the model implementation for multi-beam HF heating of the ionosphere, the next section describes the extension of the multi-beam HF heating model to account for different modulation waveforms.

2.3 Extension to Other AM Waveforms

In Chapter 4 of this dissertation, the ionosphere is modulated using a split-array configuration and five different modulation waveforms, (square, sinusoid, sqrt-sine, triangle and saw-tooth) are employed. The physics and model implementation leading

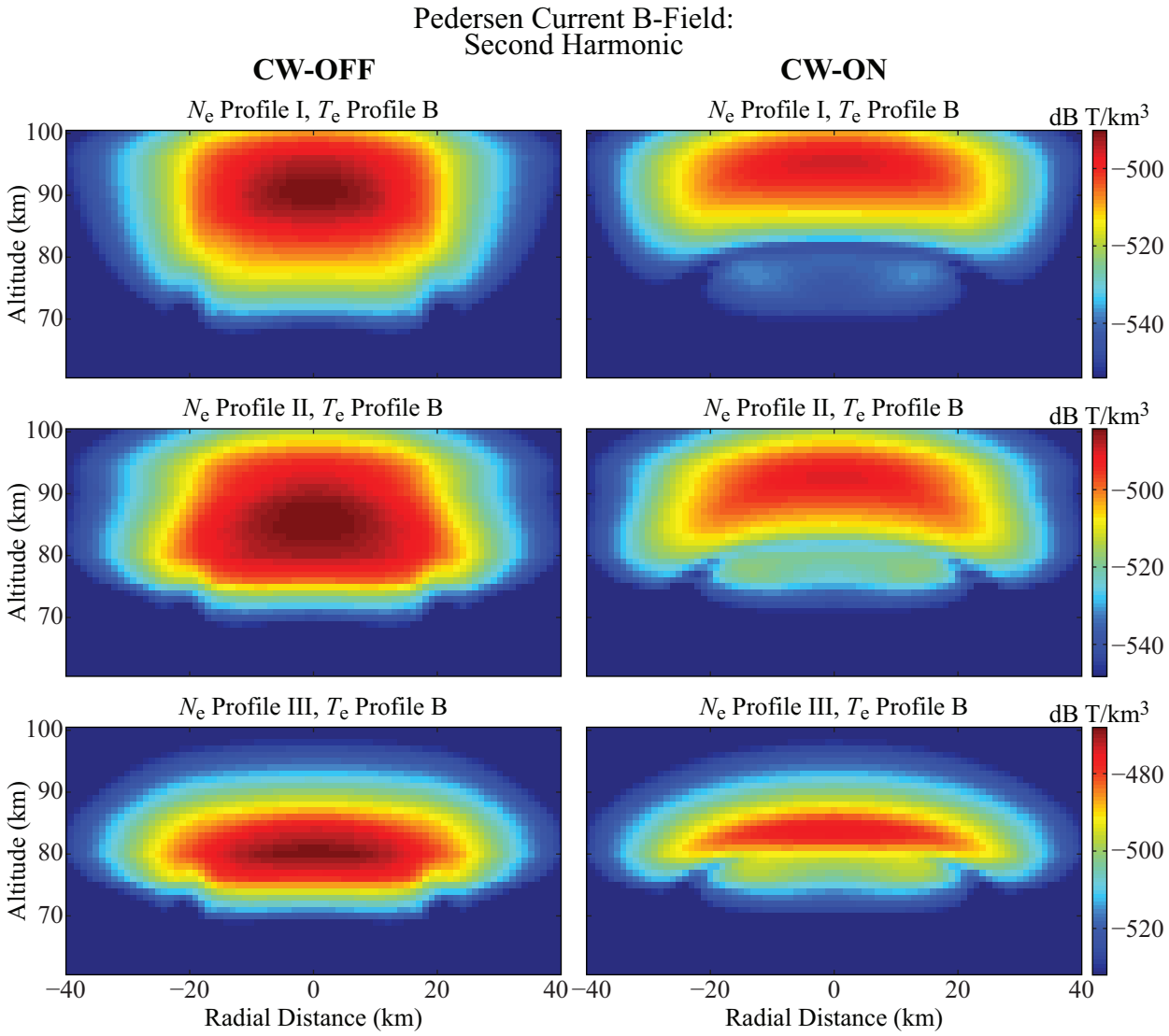

Figure 2-10. Numerical predictions. Second harmonic (2430 Hz) Pedersen current B-field amplitudes as a function of source location. CW-ON and CW-OFF periods are shown as a function of electron density profile.

to the generation of ELF/VLF waves remains the same, as explained in the previous sections, however the affect of using different modulation waveforms is manifested in the calculation of **S**, the time-averaged Poynting flux of the modulated HF wave, making sure to account for the continuous or discontinuous nature of the modulation waveform properly.

Figure 2-11 shows model predictions for T_e modulation at four different altitudes, for two steady state periods of the ELF/VLF wave generation. The model predictions

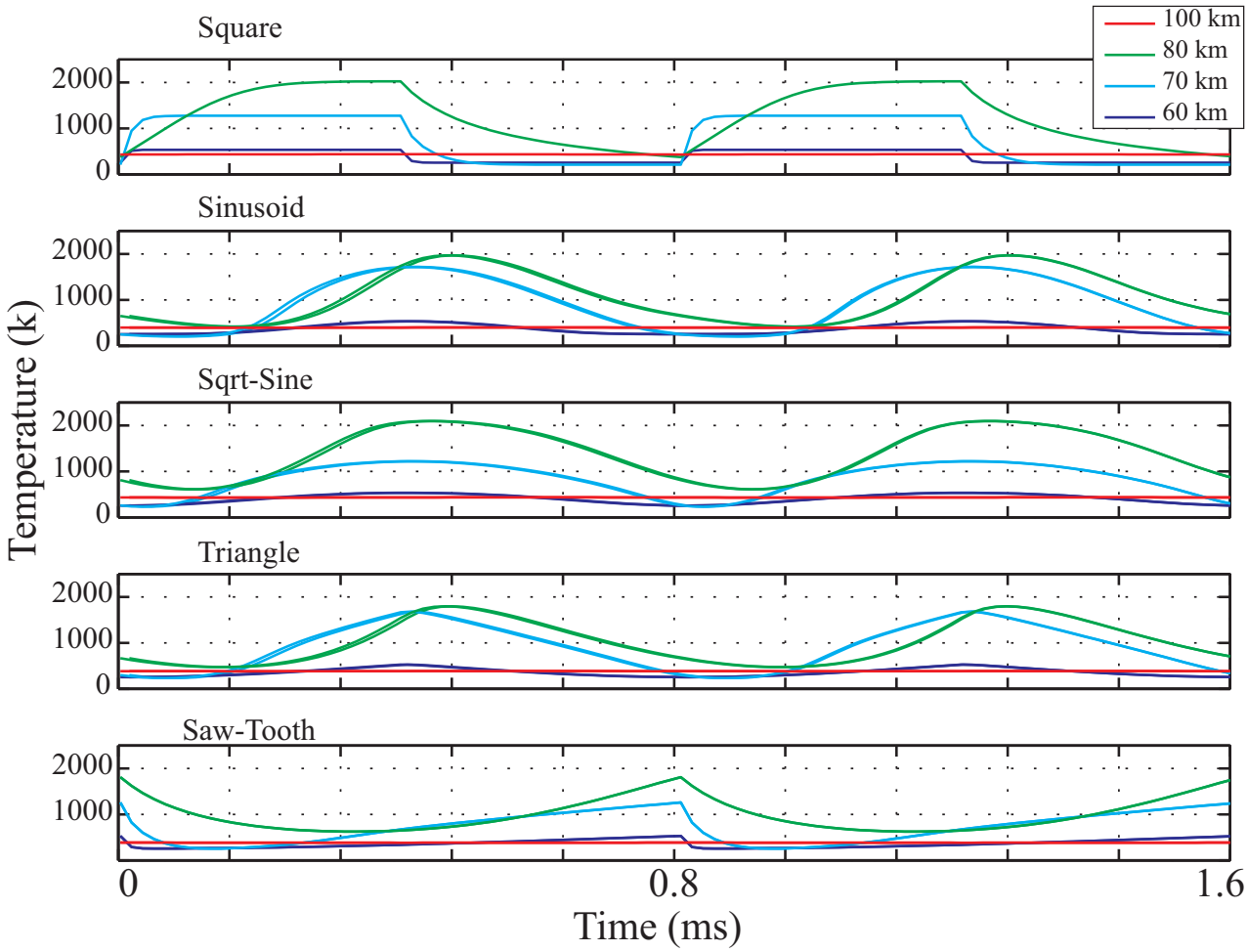

Figure 2-11. Electron Temperature modulation (at 1225 Hz) as a function of altitude for five different modulation waveforms.

shown are for a modulating frequency of 1225 Hz, using ambient conditions III-D, for CW HF frequency 3.25 MHz (78.9 dB W) and modulated HF frequency 5.8 MHz (86.4 dB W peak power and 100% modulation depth). The maximum and minimum temperatures attained at steady state as a function of altitude is not affected by the modulation waveform used. More details on ELF/VLF magnitude generated by different modulation waveforms can be found in Section 4.3.4.

The primary physical effect of dual-beam heating of the ionosphere at different CW power levels is described in Figure 2-12. The figure illustrates the maximum (red traces) and minimum (blue traces) electron temperatures achieved as a function of altitude

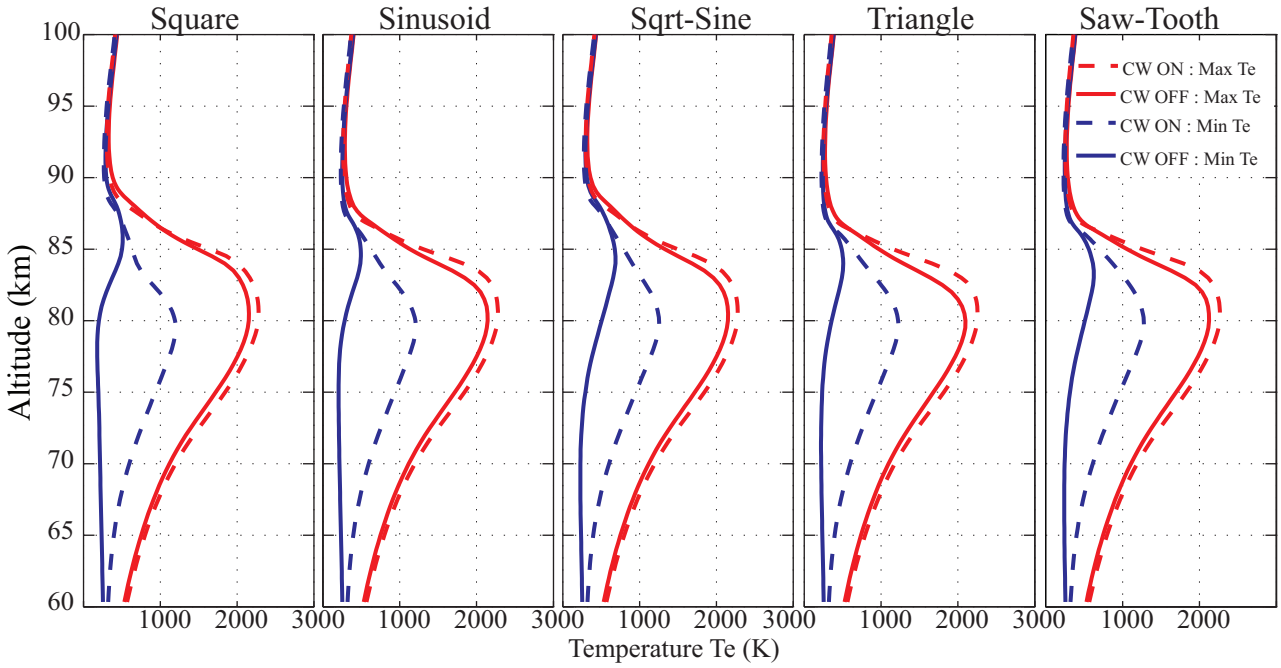

Figure 2-12. Max and min T_e as a function of altitude for five different modulation waveforms.

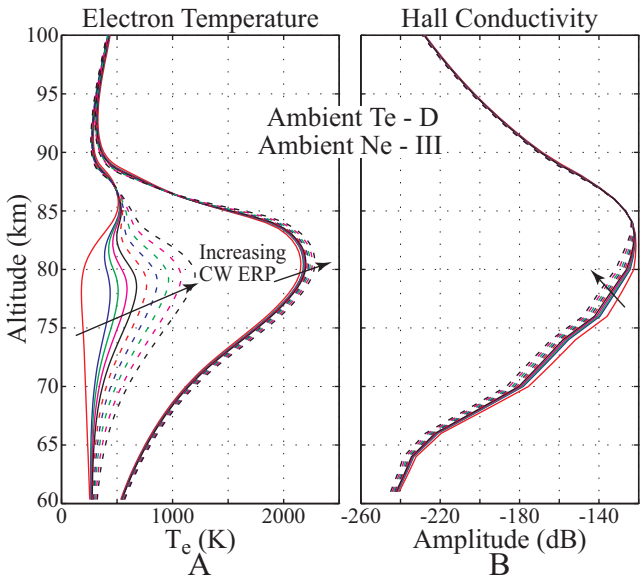

Figure 2-13. (A) Maximum and minimum T_e achieved during the heating cycle for profile combination III-D as a function of CW ERP for square wave AM. (B) The corresponding amplitude of Hall conductivity modulation as a function of CW ERP.

during sinusoidal steady state for each of the five modulation waveforms. The dashed traces, correspond to the simulations with CW at 100% power, and the solid traces correspond to simulations with CW at 0% power. As the CW power increases from 0 to full power, the minimum electron temperature (transition from solid blue to dashed blue) increases to a greater extent than the maximum electron temperature (transition from solid red to dashed red), resulting in an overall reduction in electron temperature modulation. Panel A of Figure 2-13 demonstrated this effect as a function of various CW ERP levels. Increased CW heating results in the significant reduction of the Hall conductivity modulation at lower altitudes (below $\sim$85 km) as is demonstrated by panel B of Figure 2-13. The reduction in conductivity modulation results in the overall reduction of magnetic field strength observed at the receiver as a function of CW ERP. Details of modulation affects as a function of CW ERP, are discussed in great detail in Chapter 3 and Chapter 4 of this dissertation.

2.4 Extension to X- and O-Mode Polarization of the CW Beam

It is well known that modulated X-mode heating produces higher amplitude ELF/VLF waves that does modulated O-mode heating [*Stubbe et al.*, 1981, 1982; *Ferraro et al.*, 1984; *James et al.*, 1984; *Villasenor et al.*, 1996]. In order to increase the SNR of the observations, we choose to use an X-mode polarized HF beam to modulate the ionospheric conductivity for all experiments in this dissertation. However in Section 4.3.6, we theoretically investigate the effects of using both X- and O- mode polarization on the CW beam. The primary differences in evaluating ELF/VLF wave generation using X- and O- mode polarization of the CW beam is in the calculation of the refractive index (n) and the refraction of the HF ray that results [*Budden*, 1985, p. 110].

The refractive index, n of a weakly ionized, magneto plasma is given by the well known Appleton-Hartree Equation:

$$n^2 = 1 - \frac{X}{1 - jZ - \frac{Y^2 sin^2\Theta}{2(1-X-jZ)} \pm \sqrt{\frac{Y^4 sin^4\Theta}{4(1-X-jZ)^2} + Y^2 cos^2\Theta}} \tag{2–9}$$

where the term, '$+$' term represents O-mode polarization, '$-$' represents X-mode polarization, Θ is the angle between the wave normal and the Earth's magnetic field, and:

$$X = \frac{\omega_{pe}^2}{\omega^2} \qquad Y = \frac{\omega_{ce}}{\omega} \qquad Z = \frac{\nu_{eff}}{\omega} \tag{2–10}$$

The terms X, Y and Z represent properties of the plasma. X, which is a function of the electron-plasma frequency ω_{pe}, can be thought of as the natural frequency at which the electrons are oscillating in the plasma and is related to the electron density, N_e, the charge of an electron, q_e, the permittivity, ϵ_0 and the mass of the electron, m_e, through Equation 2–11:

$$\omega_{pe} = \sqrt{\frac{N_e {q_e}^2}{\epsilon_0 m_e}} \tag{2–11}$$

Y depends on the electron gyro frequency, ω_{ce}, which is the frequency at which the electrons gyrate about an externally applied magnetic field, such as the Earth's magnetic field in our case.

$$\omega_{ce} = \frac{|q_e| B_0}{m_e} \tag{2–12}$$

Lastly, Z relates the effective electron-neutral collision frequency, ν_{eff} and the frequency of the propagating HF wave. It is this temperature-dependent quantity, ν_{eff} that primarily undergoes modulation in the HF heating process.

The refractive index, n can also be expressed as $n = \mu - j\chi$, where the real part, μ drives the wave propagation and the imaginary part, χ, determines the rate of absorption.

The deviation of the ray direction from the k-vector direction is calculated as:

$$tan\delta = \frac{1}{n}\frac{\partial n}{\partial \Theta} \tag{2–13}$$

and $\frac{1}{n}\frac{\partial n}{\partial \Theta}$ can be obtained by taking the partial differential of Equation 2–9 with respect to Θ as follows:

$$\begin{aligned}\frac{1}{n}\frac{\partial n}{\partial \Theta} = \frac{1}{2n^2}\Bigg[\frac{X}{\left[1 - jZ - \frac{Y^2 sin^2\Theta}{2(1-X-jZ)} \pm \sqrt{\frac{Y^4 sin^4\Theta}{4(1-X-jZ)^2} + Y^2 cos^2\Theta}\right]^2}\Bigg] \times \\ \Bigg[\frac{-Y^2}{(1-X-jZ)} sin\Theta cos\Theta \pm \frac{1}{2}\frac{1}{\sqrt{\frac{Y^4 sin^4\Theta}{4(1-X-jZ)^2} + Y^2 cos^2\Theta}} \times \\ \Bigg[\frac{Y^4}{(1-X-jZ)^2} sin^3\Theta cos\Theta - 2Y^2 sin\Theta cos\Theta\Bigg]\Bigg]\end{aligned} \tag{2–14}$$

where the term, '$+$' term represents O-mode polarization, '$-$' represents X-mode polarization, Θ is the angle between the wave normal and the Earth's magnetic field.

By properly accounting for the polarization of the CW beam in the refractive index and the bending of the HF ray, we evaluate the model predictions for both X- and O-mode CW polarized beams.

CHAPTER 3
ELF/VLF WAVE GENERATION USING SIMULTANEOUS CW AND MODULATED HF HEATING OF THE IONOSPHERE

In this chapter, the multibeam-HF heating model described in Chapter 2 is utilized together with ground based ELF/VLF observations to identify the property of the received wave that is most sensitive to the effects of the multibeam-HF heating. Three properties of the ELF/VLF waves are assessed: the ELF/VLF signal magnitude, the ELF/VLF harmonic ratio, and the ELF/VLF power-law exponent. Ground-based experimental observations indicate that simultaneous heating of the ionosphere by a CW HF wave and a modulated HF wave generates significantly lower ELF/VLF magnitudes than during periods without CW heating, consistent with model predictions. The ratio of ELF/VLF harmonic magnitudes is also shown to be a sensitive indicator of ionospheric modification, although it is somewhat less sensitive than the ELF/VLF magnitude and requires high SNR. Lastly, the peak power level of the modulated HF beam is varied in order to assess the power dependence of ELF/VLF wave generation under both single- and dual-beam heating conditions. Experimental and theoretical results indicate that accurate evaluation of the ELF/VLF power-law index requires high signal-to-noise ratio; it is thus a less sensitive indicator of ionospheric modification than either ELF/VLF magnitude or the ELF/VLF harmonic ratio.

The work presented in this chapter has been published in the *Journal of Geophysical Research* [*Moore and Agrawal*, 2011].

3.1 Description of the Experiment

During a thirty-minute period between 0830 and 0900 UT on 2 August 2007, the 12 $\times$15 HAARP HF transmitter array was divided into two 6 $\times$15 sub-arrays, each with a peak power of 1800 kW. One sub-array was used to generate ELF/VLF-waves in the ionosphere by transmitting a sinusoidal AM beam at 4.5 MHz (X-mode polarization). The modulation frequency alternated between 1215 Hz and 2430 Hz and the peak HF power was stepped in 15 distinct log-based steps (from $-$12.5 dB to 0 dB with

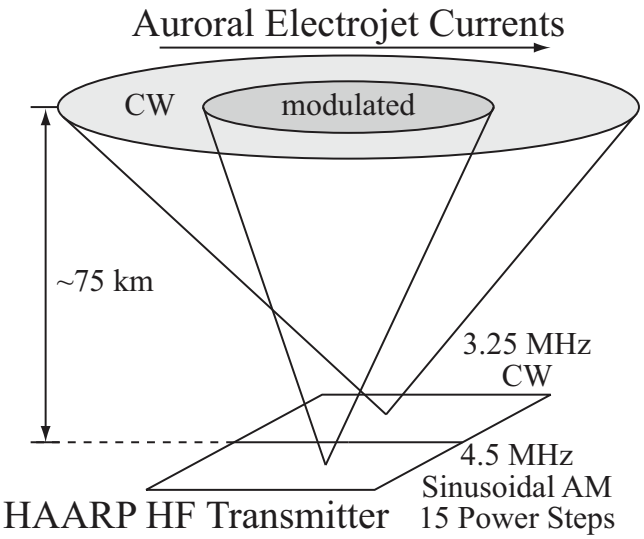

Figure 3-1. A cartoon diagram of the dual-beam HF heating experiment. The 3.25 MHz CW beam is broader than the 4.5 MHz modulated beam.

1 second at each power level). Simultaneously, the second beam of the HAARP HF transmitter continually heated the same patch of ionosphere at peak power at 3.25 MHz (CW, X-mode) for a period of 8 minutes. A lower HF frequency was selected for the CW beam so that the CW beam pattern would be broader than that of the modulated 4.5 MHz HF beam. The 8-minute CW transmission block was followed by a 7-minute period without CW heating (i.e., the first beam continued to modulate at 4.5 MHz while the second beam was OFF). A cartoon depiction of the HF beam configuration can be seen in Figure 3-1, and a diagram of the modulation frequency and HF power format can be seen in Figure 3-2. The gains of the two sub-arrays depend on the frequencies transmitted. For the purposes of modeling, we have approximated the peak effective radiated power (ERP) levels (using 6x15 sub-arrays) to be 78.9 dBW at 3.25 MHz and 84.2 dBW at 4.5 MHz. The 15-minute experiment was repeated twice during the 30-minute window, and the K_P index was 2 at this time.

ELF/VLF wave observations were performed at a ground-based receiver located at the HAARP observatory, approximately 1.5 km from the HF transmitter. The radial and azimuthal components of the magnetic field were monitored continually. In

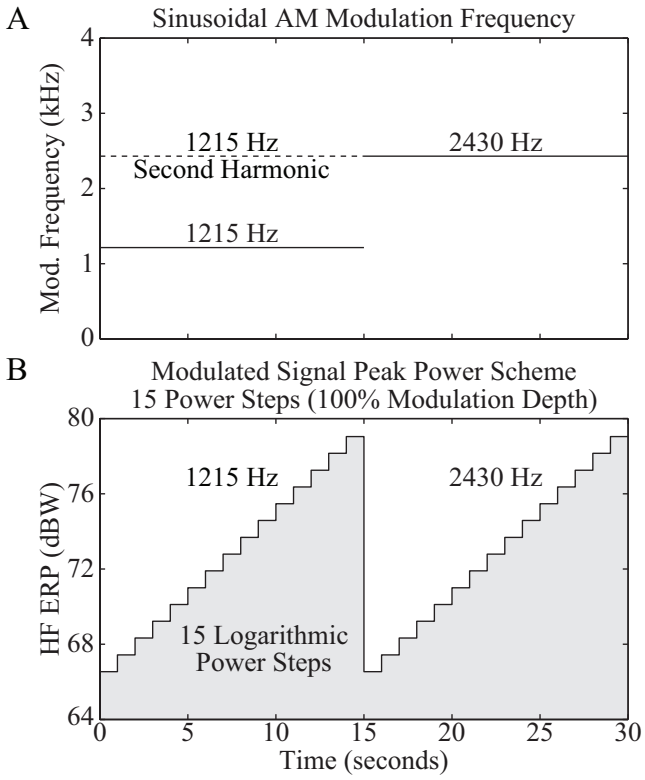

Figure 3-2. The transmission schedule for the 4.5 MHz modulated HF beam. (A) The modulation frequency (sinusoidal AM) as a function of time. (B) The peak power employed as a function of time. 100% modulation depth was used for all cases. The two panels share the same time axis. This 30-second schedule repeated continually for 30 minutes.

post-processing, the narrowband ELF/VLF amplitudes and phases at the modulation frequencies and their harmonics were determined using 1-second-long discrete Fourier transforms.

3.2 Experimental Observations

Figure 3-3 shows the magnitude of the ELF/VLF signal observed at HAARP at 1215 Hz and 2430 Hz for the entire 30-minute duration of the experiment, with the CW-ON and CW-OFF periods indicated using a gray and white background, respectively. Good ($>$10 dB) signal-to-noise ratios (SNR) were observed during the first 15 minutes of the experiment. During the second 15-minute period, the SNR decreased by approximately 5 dB. Panel B of Figure 3-3 shows several power-step series during a CW-OFF period with a magnified time scale. From 0–15 seconds

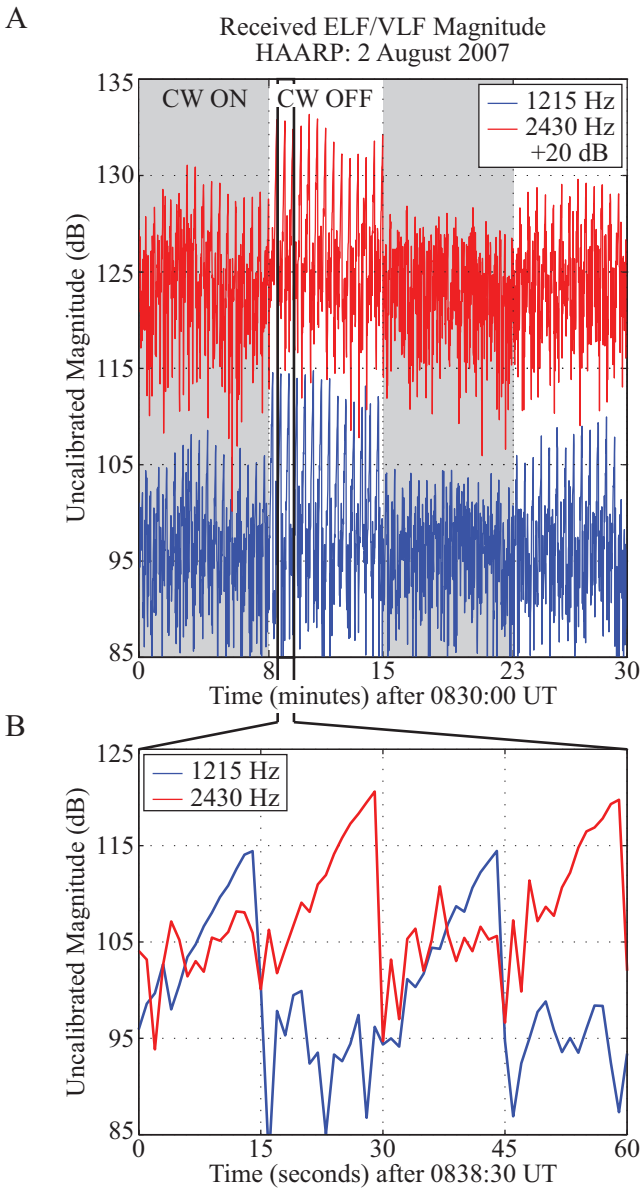

Figure 3-3. The magnitude of ELF/VLF signals observed at the ground-based receiver at HAARP. (A) All data for the 30-minute duration of the experiment, with CW-ON and CW-OFF periods indicated with gray and white backgrounds, respectively. (B) Several examples of power-step series observed during a CW-OFF block.

and from 30–45 seconds, the first and second harmonics (at 1215 Hz and 2430 Hz, respectively) clearly increase with transmitted power, which increases logarithmically over 15 seconds. From 15–30 seconds and from 45–60 seconds, a similar trend is observed, except that the 2430 Hz signal is the first harmonic (i.e., the modulation frequency was 2430 Hz). When the second-to-first harmonic ratio is calculated later in this section, we will divide the second harmonic magnitude at 2430 Hz (generated by the 1215 Hz transmission) by the first harmonic magnitude at 2430 Hz (generated by the 2430 Hz transmission), effectively canceling (to first order) the frequency-dependent effects of the Earth-ionosphere waveguide. The slopes of these traces (effectively on log-log scale) quantify the differential increase of ELF/VLF magnitude with peak modulated HF power.

We will now discuss the observed ELF/VLF magnitudes in detail.

3.2.1 ELF/VLF Magnitude

The left panels of Figure 3-4 show the probability density functions (PDFs) for the SNR, the received ELF/VLF magnitude, and the ratio of ELF/VLF magnitudes recorded during CW-OFF periods to those recorded during CW-ON periods for observations at 1215 Hz. The right panels show the same traces for observations at 2430 Hz. These PDFs are calculated using all available data points (including all power steps) in order to provide statistical significance. To calculate the SNR, noise levels are determined by extracting the ELF/VLF magnitudes at 1170 Hz (for comparison 1215 Hz) and at 2390 Hz (for comparison with 2430 Hz) as a function of time. At 1215 Hz, the SNR is on average 5.6 dB higher during CW-OFF periods than during CW-ON periods. At 2430 Hz, the SNR is 4.4 dB higher during the CW-OFF periods than during the CW-ON periods. The results are similar for ELF/VLF magnitudes: at 1215 Hz, the ELF/VLF magnitude is on average 4.9 dB higher during CW-OFF periods, and at 2430 Hz, it is 4.1 dB higher. The bottom panels show the CW-OFF to CW-ON ELF/VLF magnitude ratio, calculated by dividing the observed magnitudes separated by 8 minutes in time. For reference,

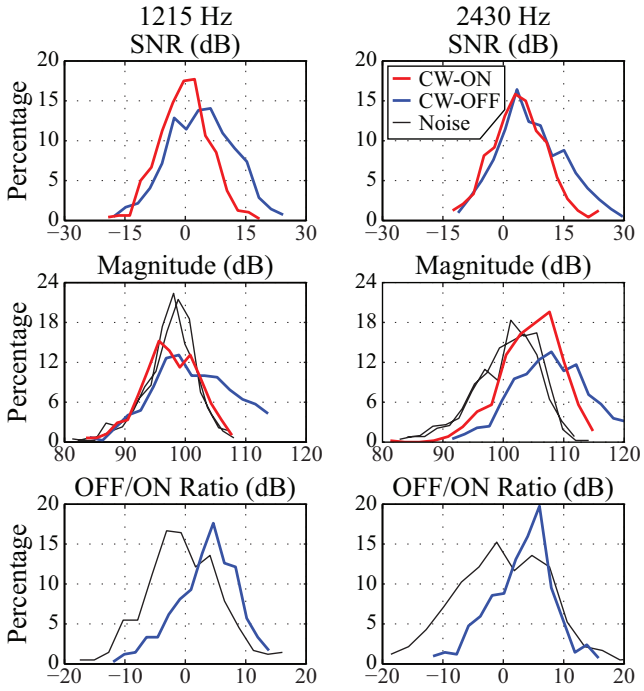

Figure 3-4. Statistical distributions (probability density functions). left column: 1215 Hz. right column: 2430 Hz. top: SNR. middle: magnitude. bottom: CW-ON to CW-OFF ratio calculated as described in the text.

the noise has been processed in the same manner. As expected, the average results are similar: a 4.9 dB ratio is observed at 1215 Hz, and a 4.5 dB ratio is observed at 2430 Hz. The fact that these distributions are very similar to each other supports the statement that the ELF/VLF magnitude is significantly reduced by additional CW heating.

In order to assess the effects of CW heating on the magnitude of the received ELF/VLF signal as a function of time, we select the magnitude of the first harmonic at the peak power transmission (i.e, the 15th power step). This selection supplies observations with the highest SNR. These magnitudes are available once every 30 seconds, and they are shown in Figure 3-5 for both 1215 Hz and 2430 Hz. The magnitudes exhibit a natural variation on the order of several dB over the 30-minute experiment. This variation is likely dominated by the varying strength of the auroral electrojet currents, but also may be due to variations in electron density and electron

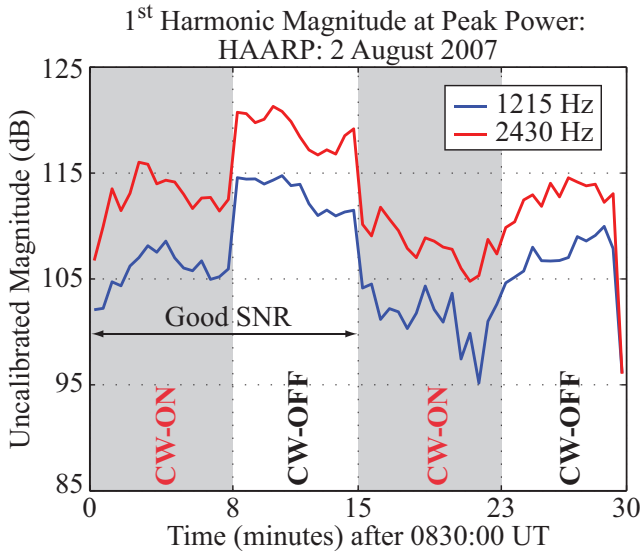

Figure 3-5. The magnitude of the 1st harmonic observed during only the peak power transmissions throughout the 30-minute experiment. For each trace, there is one sample every 30 seconds.

temperature in the *D*-region ionosphere. On the one hand, the variations in ionospheric parameters may be produced directly by HF heating; on the other hand they may also occur naturally, produced, for instance, by energetic electron precipitation or other natural phenomena. The observed change in ELF/VLF magnitude between CW-ON and CW-OFF periods, however, can be directly attributed to HF heating. At 1215 Hz and 2430 Hz, the magnitudes of the ELF/VLF signals increase by 8.6 and 8.1 dB, respectively, when the CW beam is turned off. When the CW beam is turned on again seven minutes later, the 1215 Hz and 2430 Hz magnitudes decrease by 7.4 and 9.1 dB, respectively. Observations during the second half of the experiment suffer from low SNR, although the data are not inconsistent with observations performed during the first 15 minutes of the experiment: the ELF/VLF field magnitudes are still higher during the CW-OFF period than during the CW-ON period.

The large (7–9 dB) changes in ELF/VLF magnitude between CW-ON and CW-OFF periods indicate that the ELF/VLF magnitude may be used as a very sensitive indicator of ionospheric modification and that more detailed experiments may be performed.

By alternating between CW-ON and CW-OFF periods once per second (or faster), the change in ELF/VLF magnitude may be tracked as a function of time, yielding insight into the variation of ionospheric parameters with much higher time resolution than available in the presented experiment. Additionally, the power and frequency of the CW signal may be varied, resulting in different changes in ELF/VLF magnitude between CW-ON and CW-OFF periods. Based on the large (7–9 dB) changes in ELF/VLF magnitude presented in this chapter, it is likely that these suggested experiments would yield measurable distinct changes ELF/VLF magnitude, and we directly assess this possibility in the modeling section of the chapter and in Chapter 4.

We now move on to discuss another sensitive experimental method to detect changes in ionospheric properties.

3.2.2 ELF/VLF Harmonic Ratio

In this work, the ELF/VLF harmonic ratio is the ratio of the second harmonic magnitude to the first harmonic magnitude. For the presented experiment, ELF/VLF waves were generated using sinusoidal amplitude modulation, and the power envelope of the HF transmission thus consists of a first and second harmonic. If square-wave amplitude modulation had been used, for instance, an equivalent measure would be the third harmonic to first harmonic ratio. In any case, the ratio of these two magnitudes generated at the same time essentially cancels strength of the auroral electrojet currents (to first order). Propagation within the Earth-ionosphere waveguide is strongly frequency-dependent, however. In order to cancel the effects of the Earth-ionosphere waveguide (to first order), we require that the two magnitudes be measured at the same frequency. It is impossible to discern first and second harmonics generated at the same frequency at the same time, however. As a reasonable approximation, we generate the second harmonic at 2430 Hz using a 1215 Hz tone, and the first harmonic a short time later using a 2430 Hz tone. *Barr and Stubbe* [1993] used this method for evaluating

harmonic ratios with great success to cancel (to first-order) the frequency-dependent effects of the Earth-ionosphere waveguide.

Because the SNR of the second harmonic is not particularly high throughout each of the 15 power steps, we use the second harmonic magnitude during only the peak power step ($\sim$6 dB SNR) to analyze the second-to-first harmonic ratio. Figure 3-6 shows the variation of the harmonic ratio over the course of the 30-minute experiment. During the first CW-ON period, the harmonic ratio is essentially constant at -14.05 ± 0.4 dB. We attribute the two sharp, but temporary, deviations from this level to lightning-generated sferics coupling into the band rather than to changes in the properties of the ionosphere. When the CW beam turns off, however, the harmonic ratio immediately decreases by 3.75 dB to -17.8 ± 0.7 dB. During the CW-OFF period, the ratio again remains relatively constant, with two sharp deviations that likely result from lightning. During the second 15-minute period of the experiment, observations suffer from low SNR. Despite this fact, some comparisons can be made. Upon turning the CW beam ON for the second time, the harmonic ratio immediately increases by 4.5 dB. During the second CW-ON period, the harmonic ratio fluctuates rapidly between -12 and -15 dB due to low SNR, although we note that the -12 to -15 dB range includes the -14 dB level observed during the first CW-ON period. Approximately 1 minute into the second CW-OFF period, the SNR increases somewhat, and the harmonic ratio remains close to -18 dB for the remainder of the period, similar to the first CW-OFF period.

The assumption that the harmonic ratio is a sensitive indicator of ionospheric change under good SNR conditions will be evaluated numerically in the modeling section of this chapter. Because the harmonic ratio is evaluated only once every 30 seconds, the immediacy of the -3.75 dB change and the $+4.5$ dB change at CW-ON/CW-OFF boundaries can only be stated with 30-second resolution. This may easily be improved during future experiments, however, by omitting the power-stepping feature of the presented experiment.

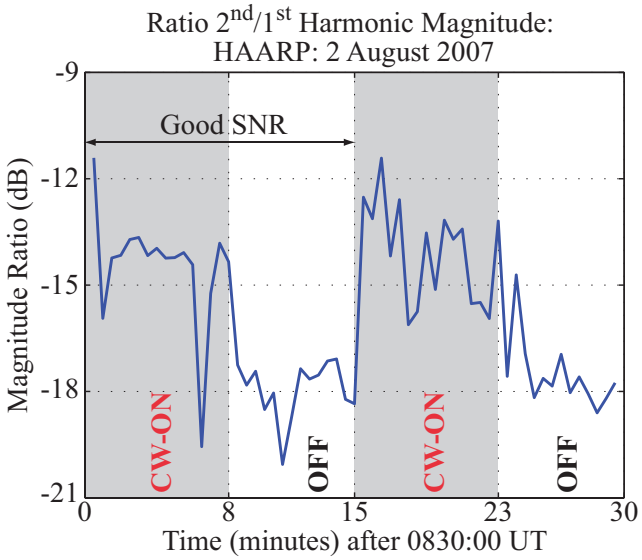

Figure 3-6. Ratio of the second harmonic magnitude to the first harmonic magnitude, calculated as discussed in the text, observed during only the peak power transmissions throughout the 30-minute experiment. There is one sample every 30 seconds.

We will now discuss the observed dependence of ELF/VLF magnitude on HF power.

3.2.3 ELF/VLF Power-Law Exponent

In the early 1990's, *Papadopoulos et al.* [1990] and *Barr and Stubbe* [1991] suggested that the ELF/VLF magnitude depends on the peak input HF power as a power law with index n: $A_{\mathrm{ELF}} \propto P_{\mathrm{HF}}^{n}$. In this context, we will refer to the index n as the ELF/VLF Power-Law Exponent (EPLE), which should in principle depend on the ambient properties of the D-region ionosphere. For each power-step series performed in our experiment, the EPLE is calculated using a weighted least-square fit to the observed ELF/VLF magnitude as a function of HF power: $n = (P_{\mathrm{HF}}^{\mathsf{T}} W^{\mathsf{T}} W P_{\mathrm{HF}})^{-1} P_{\mathrm{HF}}^{\mathsf{T}} W^{\mathsf{T}} W A_{\mathrm{ELF}}$, with the weights of the matrix W determined by the SNR of the data points.

Figure 3-7 shows the EPLE calculated for both 1215 Hz and 2430 Hz over the course of the experiment with 30-second resolution. During the first 15-minute period, the EPLE measured at 1215 Hz is 0.63 ± 0.15 during the CW-ON period and 0.68 ± 0.11 during the CW-OFF period. No significant trends are observed during either the CW-ON or CW-OFF period, although they may be obscured by the noise. The EPLE exhibits a

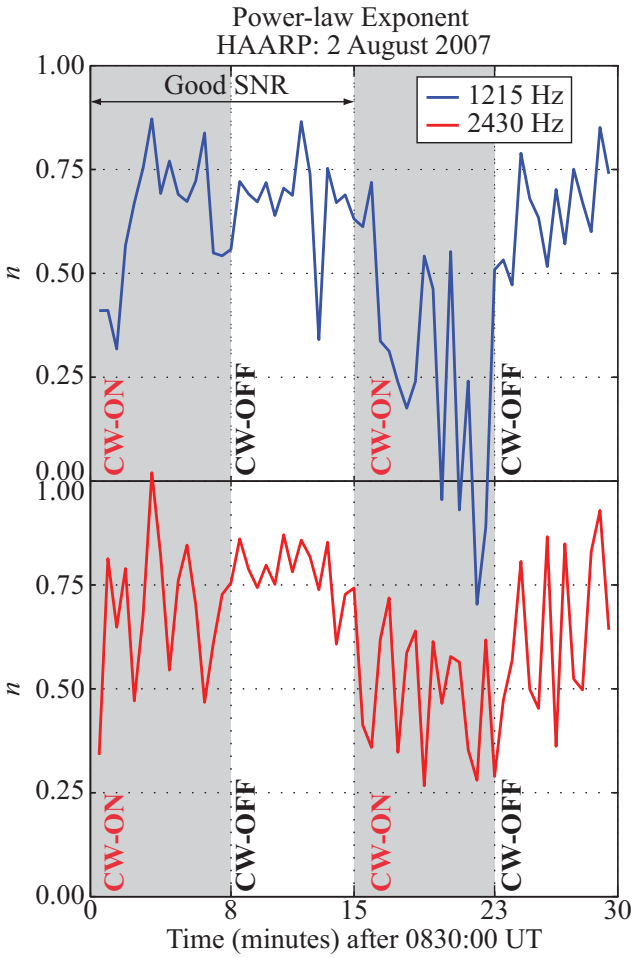

Figure 3-7. The power-law exponent at 1215 Hz and 2430 Hz for each power-step series, calculated as discussed in the text. The two traces are separated for clarity. For each trace, there is one sample every 30 seconds.

very subtle increase coincidentally with (within 30 seconds of) the change from CW-ON to CW-OFF. At 2430 Hz, the EPLE is measured to be 0.69 ± 0.16 during the CW-ON period and 0.78 ± 0.07 during the CW-OFF period. Again, no significant trends are observed during either period, although small trends may be obscured by the noise of the measurement. In this case, the EPLE appears to increase coincidentally (within 30 seconds) with the change from CW-ON to CW-OFF. During the second 15-minute period, the SNR is too low for a reliable calculation of the EPLE. This effect is evident in the marked increase in measurement variability during the second 15-minute period.

The appearance of slight increases in EPLE at both 1215 Hz and 2430 Hz during CW-OFF periods may be misleading, however. Based on this data set, turning off the CW beam increases the EPLE by 0.05 ± 0.26 at 1215 Hz and by 0.09 ± 0.23 at 2430 Hz. The large uncertainties in the EPLE measurements indicate that it is not as well-suited for evaluating changes in ionospheric properties as the ELF/VLF magnitude or the ELF/VLF harmonic ratio. Furthermore, it would be difficult to properly evaluate the EPLE with high time resolution. These conclusions will be evaluated in the theoretical modeling section of this chapter.

3.3 Model Predictions

In the following sections, each property of the ELF/VLF wave is compared with model predictions of the dual-beam HF heating experiment, as described in great detail in Chapter 2. The ambient electron density and electron temperature profiles used for the purpose of modeling are the same profiles as in Figure 2-1.

3.3.1 ELF/VLF Magnitude

Figure 3-8 shows the total B-field magnitude received on the ground at 1215 and 2430 Hz as a function of electron density and electron temperature profile. At both modulation frequencies, the magnitude of the B-field at the receiver increases with increasing (80 km) electron density at a rate of about 10 dB per profile. Because the electron density increases by a factor of 10 between each profile, the x-axis of these plots have an essentially logarithmic scale. Thus, a factor of 2 change in electron density at 80 km, as suggested by *Milikh and Papadopoulos* [2007], would produce $\sim$5 dB increase in ELF/VLF magnitude on the ground by these estimates. This value is only slightly smaller than the 7 dB increase in magnitude predicted by *Milikh and Papadopoulos* [2007]. The effect of ambient electron temperature is less pronounced on these plots, but still important, as they may produce a 2–5 dB change in ELF/VLF magnitude. In most cases, the ELF/VLF B-field magnitude increases with decreasing ambient electron temperature. The one exception is the combination of electron density

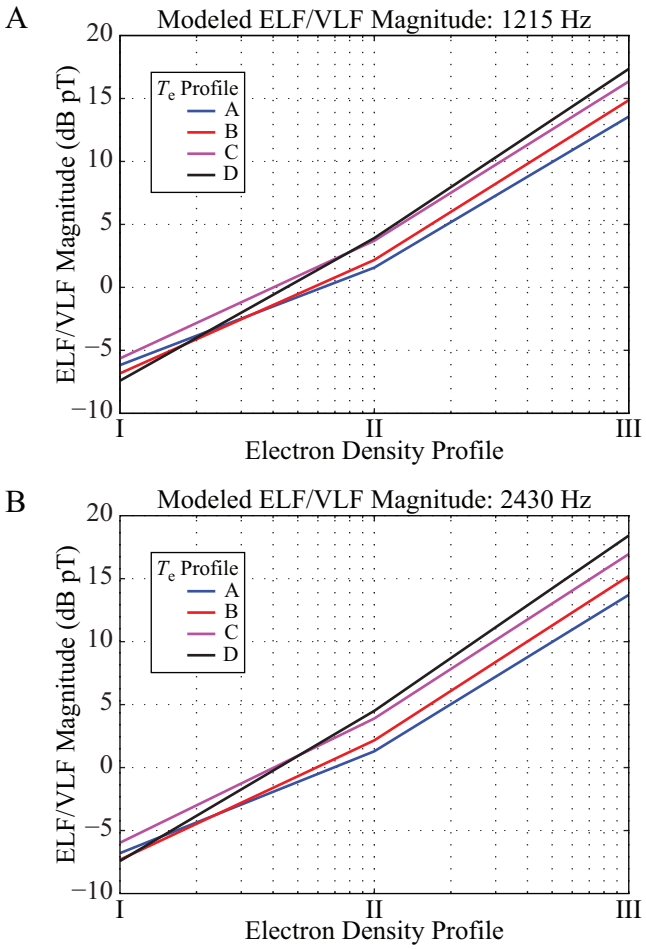

Figure 3-8. Numerical predictions. Total B-field magnitude at the receiver as a function of electron density profile and electron temperature profile. (A): 1215 Hz. (B) 2430 Hz.

Profile I with electron temperature Profile D. Together, these plots indicate that the ELF/VLF B-field magnitude observed on the ground could be more effectively enhanced by the introduction of a chemical process that both increases the electron density and simultaneously decreases the electron temperature in the *D*-region. The two effects are typically competing effects, however, as an increase in electron density also produces an increase in electron-neutral collision frequency.

Figure 3-9 shows the change in ELF/VLF magnitude received on the ground during CW-ON and CW-OFF periods. Positive dB values on this plot indicate that the ELF/VLF magnitude is higher during CW-OFF periods than during CW-ON periods. We note

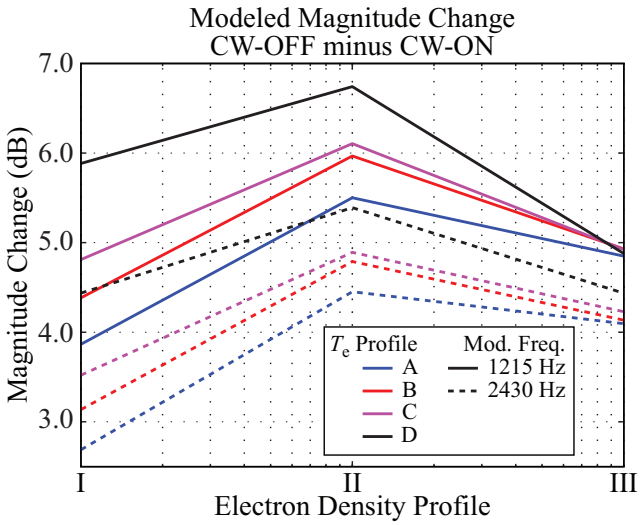

Figure 3-9. Numerical predictions. The change in total B-field magnitude at the receiver from CW-OFF to CW-ON conditions.

that this model predicts that the B-field on the ground is always higher during CW-OFF periods than during CW-ON periods, consistent with observations at these power levels. The observed 7-9 dB changes in ELF/VLF magnitude (shown in Figure 3-5) are slightly ($\sim$2 dB) higher than the predicted values shown in Figure 3-9. Nevertheless, the predicted values are reasonably close to the observed values. Considering that the additional CW heating tends to increase the altitude of the dominant ELF/VLF source currents, it may be the case that Earth-ionosphere waveguide effects, which depend upon both the altitude and frequency of the source and which are not accounted for in our wave propagation model, may be important in accurately accounting for the change in ELF/VLF magnitude on the ground.

Considering the changes predicted for both modulation frequencies, the model predicts that the change in ELF/VLF magnitude on the ground is about 1 dB lower at 2430 Hz than at 1215 Hz. This was the case observed during the first CW-ON/CW-OFF transition, which is very encouraging, but it was not the case during the second CW-ON/CW-OFF transition, when the change in 2430 Hz magnitude was observed to change by 1 dB more than at 1215 Hz. Whether or not this is the typical observational

case will not be resolved in this chapter, but may easily be resolved by additional experimental studies. The frequency-dependent effects of the Earth-ionosphere waveguide may contribute to the discrepancy, which may also be affected by the assumption that the conductivity modulation is cylindrically symmetric. Despite these shortcomings, the model captures in a general sense the effects of simultaneous CW and modulated HF heating, in that it consistently predicts lower ELF/VLF magnitudes on the ground during CW-ON periods, and in that the predicted changes in magnitude are within $\sim$2 dB of observations. The observed large 7-9 dB changes in ELF/VLF magnitude indicate that the ELF/VLF magnitude may be sensitive to the frequency and power of the CW beam and we evaluate this possibility in great detail in Chapter 4.

Having discussed the predicted ELF/VLF magnitudes in great depth, we now proceed to consider the theoretical predictions for the ELF/VLF harmonic ratio.

3.3.2 ELF/VLF Harmonic Ratio

As described earlier in this chapter, the ELF/VLF harmonic ratio cancels frequency dependent propagation effects to first order. The second order effect depends on the spatial distribution of the source currents that generate the first and second harmonics.

Panel A of Figure 3-10 shows the ELF/VLF harmonic ratio as a function of electron density profile and electron temperature profile during CW-OFF periods, and the bottom panel shows the dB change in harmonic ratio between CW-ON and CW-OFF periods. The negative changes shown in the bottom panel indicate that the harmonic ratio is modeled to be higher during CW-ON periods than during CW-OFF periods, consistent with observations. The combination of electron density Profile III and electron temperature Profile D matches our observations very closely, both in terms of the CW-OFF harmonic ratio (-17.8 dB measured, -18.3 dB modeled) and in terms of the change in harmonic ratio between CW-ON and CW-OFF periods (-3.75 dB measured, -3.2 dB modeled). We attribute the closeness of this match to the effective cancellation of both first- and second-order propagation effects, which were not

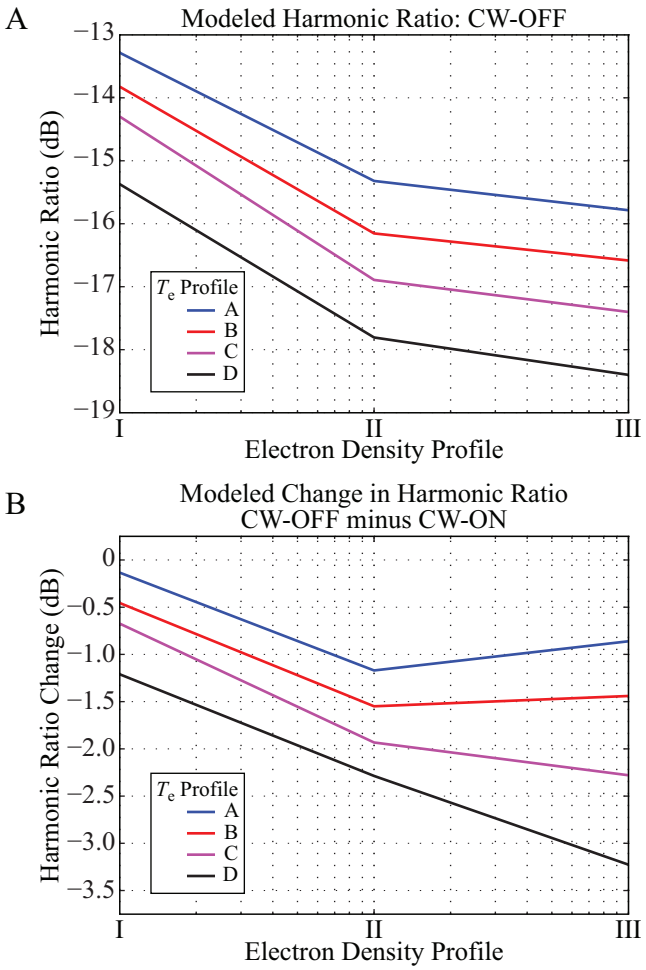

Figure 3-10. (A) ELF/VLF harmonic ratio (as described in the text) as a function of electron density profile and electron temperature profile. (B) The change in ELF/VLF harmonic ratio from CW-OFF to CW-ON conditions.

conveniently canceled by other measurement techniques. Interestingly, model results (not shown) indicate that the ELF/VLF harmonic ratio is a relatively stable value in terms of observation location, varying by less than $\sim$1 dB within 100 km of the HAARP transmitter.

The harmonic ratio is very sensitive to both the electron density profile and the electron temperature profile used, varying by several dB in both cases. The change in harmonic amplitude at CW-ON/CW-OFF boundaries is also easily detectable and quick to evaluate (only two ELF/VLF frequencies needed). It thus appears that the ELF/VLF harmonic ratio is ideally suited to evaluate HAARP-induced electron density changes

at the altitude of wave generation. Panel B of Figure 3-10 indicates that (for Profile D) a factor of 2 increase in electron density would result in an additional $\sim$0.25 dB change in the harmonic ratio between CW-ON and CW-OFF periods. In the observations from the current experiment this is not observable above the noise. We can limit the maximum change in electron density to a factor of $\sim$5, based on the $\pm$0.7 dB uncertainty of the measurement, however. The relatively weak ELF/VLF wave generation during the experiment, however, indicates that future experiments may have more success applying this technique to further limit the possible heater-induced change in the electron density with time.

Here we point out that electron density Profiles II and III, together with electron temperature Profile D have most closely matched the change in ELF/VLF magnitudes at CW-ON/CW-OFF boundaries and they also closely reproduce changes in ELF/VLF harmonic ratios that very closely match the observations presented earlier in this chapter. Although we have not presented an exhaustive set of electron density and temperature profiles, it is reasonable to conclude that electron temperature Profile D and some combination of electron density Profiles II and III are reasonable estimates of the physical properties of the *D*-region ionosphere during the presented experiment.

3.3.3 ELF/VLF Power-Law Exponent

The EPLE values as a function of electron density and electron temperature are shown in the panels A and B of Figure 3-11. Two important results are immediately evident from Figure 3-11. For the high HF power levels for which these results were calculated, the EPLE decreases significantly as the electron density varies from Profile I to Profile III (i.e., as the electron density increases). This result stands in stark contrast to the simulation results for the ELF/VLF magnitude, which increases sharply between Profiles I and III. Together, these simulation results support the conclusion that the EPLE does not represent the overall efficiency of ELF/VLF wave generation. A second result that is clearly depicted in Figure 3-11 is the tempering effect of additional CW heating

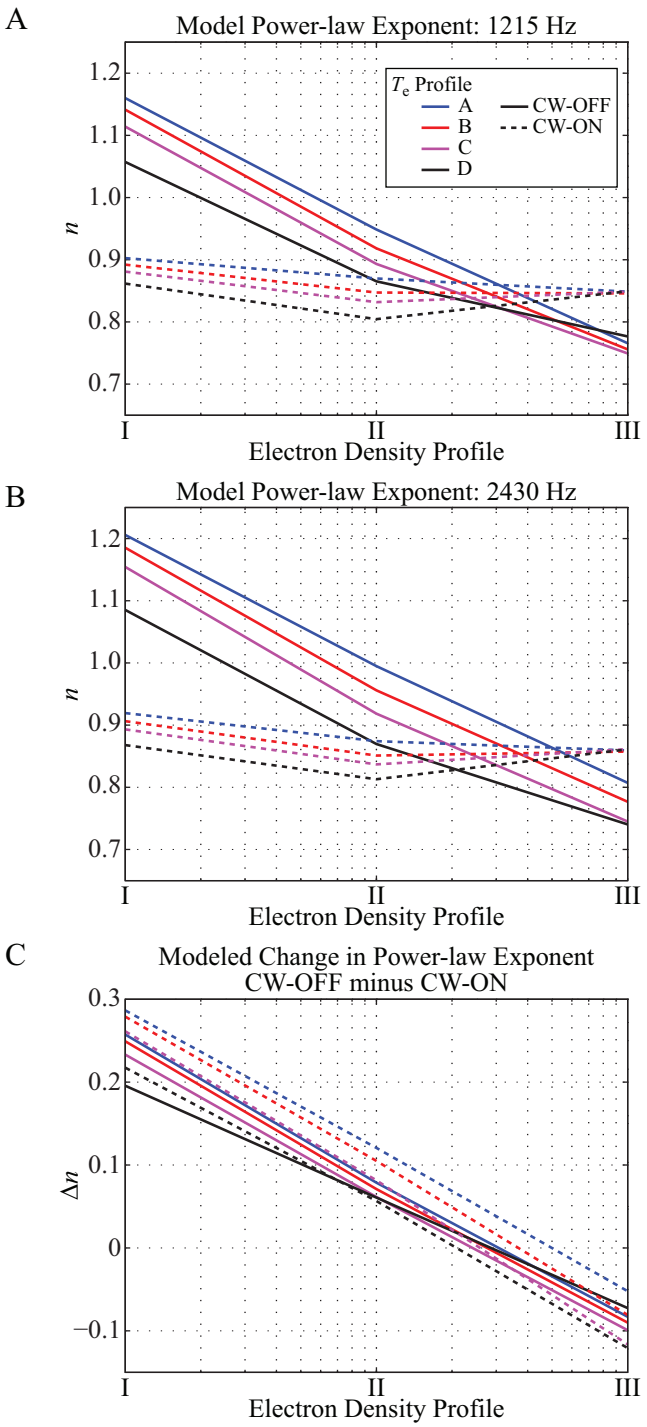

Figure 3-11. Numerical predictions. (A,B): n at 1215 and 2430 Hz. (C): The change in n from CW-OFF to CW-ON conditions.

on the EPLE. Although the EPLE varies significantly as a function of electron density profile under CW-OFF conditions, it is relatively constant under CW-ON conditions. This effect yields the general result that the EPLE may be either higher or lower during CW-ON or CW-OFF periods, depending on the electron density profile and the electron temperature profile employed.

Further conclusions may be drawn by closely inspecting the dependence of EPLE on electron density and electron temperature. A factor of two increase in electron density at 80 km altitude would decrease n by approximately 0.05–0.07. *Milikh and Papadopoulos* [2007] predict this change may occur with a timescale on the order of 1 minute (although at $\sim$85 km altitude). The level of noise in our experimental observations of EPLE, however, is much too large to detect this small modification. The ELF/VLF harmonic ratio clearly constitutes a much better measurement for providing limits for possible changes in electron density. The electron temperature is also an important factor in determining the EPLE. Similar to the dependence on electron density, n typically decreases as the electron temperature decreases, despite the indication that the total ELF/VLF magnitude tends to increase with decreasing electron temperature. The large uncertainty in our experimentally observed EPLEs makes our observations consistent with almost all of our modeling runs. While the ELF/VLF magnitude and the ELF/VLF harmonic ratio appear to be sensitive to ionospheric changes even under low SNR conditions, the EPLE derived from low SNR observations is clearly not a good indicator for ionospheric modification.

3.4 Discussion

We have presented experimental evidence along with model predictions indicating that the magnitudes of ELF/VLF waves observed on the ground are significantly reduced when generated together with a broader CW heating beam. We demonstrated that the ELF/VLF harmonic ratio is also sensitive to the presence of the CW heating beam, although it is somewhat less sensitive than the ELF/VLF magnitude and requires high

SNR. Lastly, the ELF/VLF power-law exponent was shown to be too sensitive to SNR to provide accurate experimental observations relating to ionospheric modification. Based on these observations, we conclude that the ELF/VLF signal magnitude as a function of HF transmission parameter is the property of the received ELF/VLF field that is most sensitive to the ambient ionospheric conditions.

CHAPTER 4
ELF/VLF WAVE GENERATION AS A FUNCTION OF POWER, FREQUENCY, MODULATION WAVEFORM, AND RECEIVER LOCATION

Based on the results of Chapter 3, this chapter focuses on the ELF/VLF magnitude generated as a function of the controllable transmission parameters at HAARP: HF power, HF frequency, modulation waveform, and HF polarization. The experimental observations are compared to the predictions of the dual-beam ionospheric HF heating model (Chapter 2) to identify the transmission parameters that provide independent information about the ambient D-region ionosphere.

This chapter progresses in the following manner: Section 4.1 describes the experiment; Section 4.2 presents a general description of experimental observations performed during the dual-beam HF heating experiment; and Section 4.3 directly compares the observations and model predictions. Section 4.4 provides a discussion and a summary of the presented material.

The work presented in this chapter has been published in the *Journal of Geophysical Research* [*Agrawal and Moore*, 2012].

4.1 Description of the Experiment

During three half-hour periods on 20, 21, and 25 July 2011, HAARP once again used a dual-beam heating configuration for which the HF array was split into two 6×15 (1800 kW) sub-arrays capable of simultaneously transmitting two independent HF beams at different HF frequencies. The first sub-array broadcast an amplitude modulated HF signal in order to generate ELF waves; we will refer to the modulated beam as Beam 1. At the same time, the second sub-array broadcast a CW wave at a different HF frequency and varied the power of the transmission; we will refer to the CW beam as Beam 2. The center frequency for Beam 1 alternated between 5.8 and 6.9 MHz (X-mode), and the peak power was held constant at 100%. The modulation was driven at 1225 Hz using five different modulation waveforms: square, sinusoid, square-root-sinusoid (sqrt-sine), triangle, and saw-tooth. The center frequency for

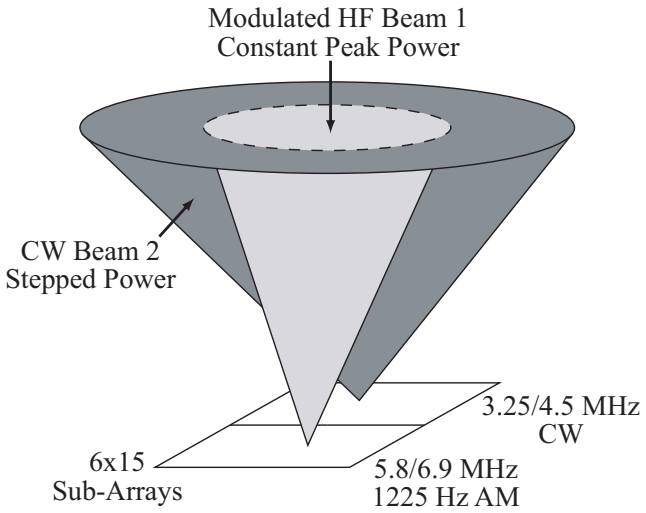

Figure 4-1. A cartoon diagram of the Dual-Beam HF heating experiment, showing the modulated HF beam (constant peak power) and the power-stepped CW beam. The CW beam is broader than the modulated HF beam.

Beam 2 alternated between 3.25 and 4.5 MHz (X-mode), resulting in four different HF frequency combinations between Beam 1 and Beam 2. The center frequency of Beam 2 was selected to be lower than that of Beam 1 in order to bathe the entire modulated ionospheric region with CW power, as depicted in the cartoon diagram of Figure 4-1. Although the cartoon diagram is very similar to that shown in Chapter 3, the transmission details are different. In this case, the peak power of Beam 2 increased (in 1-dB steps) from -8 dB to 0 dB (full power), resulting in ten CW power levels (including CW-OFF). Each CW power level was held constant for a one-second duration, and the CW transmission alternated between CW-OFF and CW-ON every other second to provide a means to evaluate changes in the electrojet field strength [*Barr and Stubbe*, 1993]. For each frequency combination, the 18-second transmission format was repeated five times: once for each modulation waveform.

Figure 1-4 maps the locations of the ELF/VLF receiver sites relative to HAARP. ELF/VLF receivers were located at Oasis (OA, 62.35°N, 145.1°W, 3 km from HAARP), Sinona Creek (SC, 62.58°N, 144.6°W, 33 km from HAARP), and Paradise (PD, 62.52°N, 143.2°W, 98 km from HAARP). In post-processing, the amplitudes and phases of the

received ELF/VLF tones were once again determined using 1-second-long discrete Fourier transforms.

4.2 Description of the Data Set

Figure 4-2 shows the first harmonic ELF signal magnitude (at 1225 Hz) received at Paradise during the three thirty-minute duration transmission blocks on 20, 21, and 25 July 2011. Signals with high ($>$10 dB) signal-to-noise ratio (SNR) were observed throughout the half-hour transmission periods on 20 July and 25 July. Our analysis will focus on observations performed during these two days, which are highlighted with a gray background in Figure 4-2. On both days, the HAARP fluxgate magnetometer registered magnetic field fluctuations of over 100 nT during the transmission periods, and the k_p index was $3+$. The level of absorption, as measured by the 30-MHz HAARP riometer, was much higher on 20 July ($\sim$0.2 dB) than on 25 July ($<$0.1 dB). Additionally, ionospheric electron density profile estimations performed by the HAARP digisonde at the times of transmission indicate that the ionospheric profiles were dramatically different on the two days, even in the *D*-region: the electron density at 100 km was $\sim\ 3.6 \times 10^4$/cm^3 on 20 July, whereas it was less than 1.2×10^4/cm^3 on 25 July. The comparison of observations performed on these two days will thus be used to experimentally investigate dual-beam ELF wave generation as a function of ambient ionospheric conditions.

Figure 4-3 shows 90-second spectrograms of the magnetic field recordings performed at Paradise on 20 July 2011. The top and bottom panels corresponds to the North-South (NS) and East-West (EW) channels of the receiver, respectively. During this 90-second period, HAARP broadcast five 18-second formats, one for each of the five different modulation waveforms employed. In order, these are: square, sinusoid, sqrt-sine, triangle, and saw-tooth waveforms. In all cases, the first harmonic at 1225 Hz is clearly visible in the spectrograms for each channel. Higher-order harmonic content is observed to depend on the modulation waveform. While observations of the

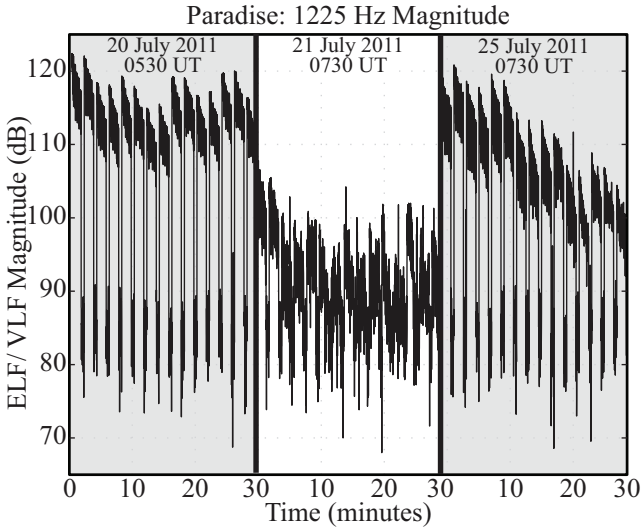

Figure 4-2. 1225 Hz signal magnitude observed at Paradise (PD) on 20, 21, and 25 July 2011. The highlighted gray backgrounds identify periods of high ($>$10 dB) SNR.

higher-order harmonics are important, this analysis will focus solely on the first harmonic component.

Panel B of Figure 4-4 shows the magnitude of the 1225 Hz tones observed at Paradise during the 30 minute transmission period on 20 July 2011. The alternating gray and white backgrounds represent the repetition of the 8-minute transmission format, which includes four distinct HF frequency combinations (between Beam 1 and Beam 2). Within each section, four distinct groups of data points ranging from $\sim$105 to $\sim$122 dB are clearly discernible, and these groups correspond to observations as a function of HF frequency combination. The data points ranging from $\sim$80 to $\sim$92 dB are performed during transmitter off times, and the largest of these amplitudes is used to estimate the noise floor.

Panel A of Figure 4-4 provides an expanded-time view of the 90-second transmission period for Beam 1 at 5.8 MHz and Beam 2 at 4.5 MHz. During this 90-second period, Beam 1 continuously modulated the conductivity of the lower ionosphere, changing the modulation waveform every 18 seconds. At the same time, Beam 2 broadcast a CW wave every other second (alternating between on and off) increasing the power of the

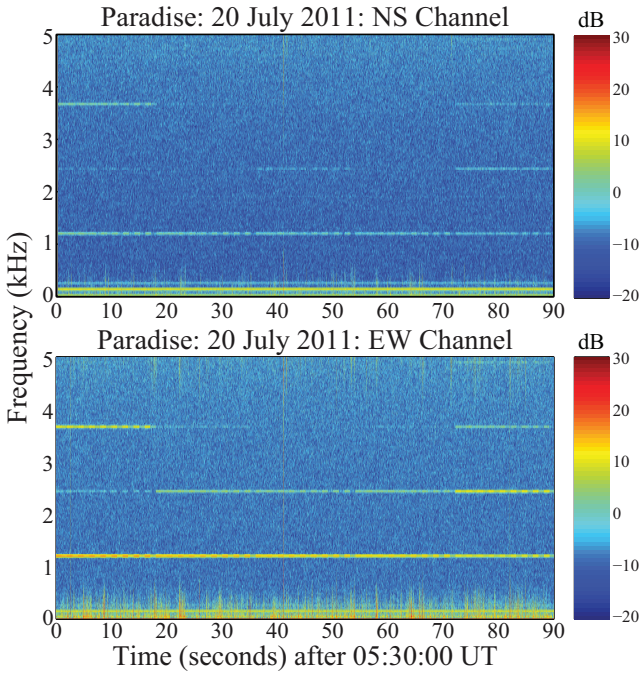

Figure 4-3. 90-second spectrograms of ELF observations at Paradise. Strong ELF waves are generated at 1225 Hz, as well as at higher-order harmonics.

transmission in 1-dB steps over the course of 18 seconds. The observations shown in Figure 4-4 demonstrate that the first harmonic magnitude during CW-OFF periods is clearly stable over each 18-second period, varying by less than 1 dB. The CW-OFF signal stability indicates that the ionosphere and the strength of the auroral electrojet were stable over the transmission sequence. The first harmonic magnitude also clearly depends on the modulation waveform employed, as can be seen by the several-dB changes in magnitude when the modulation waveform changes. These changes in magnitude are approximately consistent with Fourier analysis of the power envelope of the transmitted modulation waveform, as described by *Barr and Stubbe* [1993], and the slight deviations from Fourier analysis will be discussed in Section 4.3. During the CW-ON periods, the 1225 Hz signal magnitude is observed to decrease with increasing CW power for all modulation waveforms, consistent with the observations presented by *Moore and Agrawal* [2011].

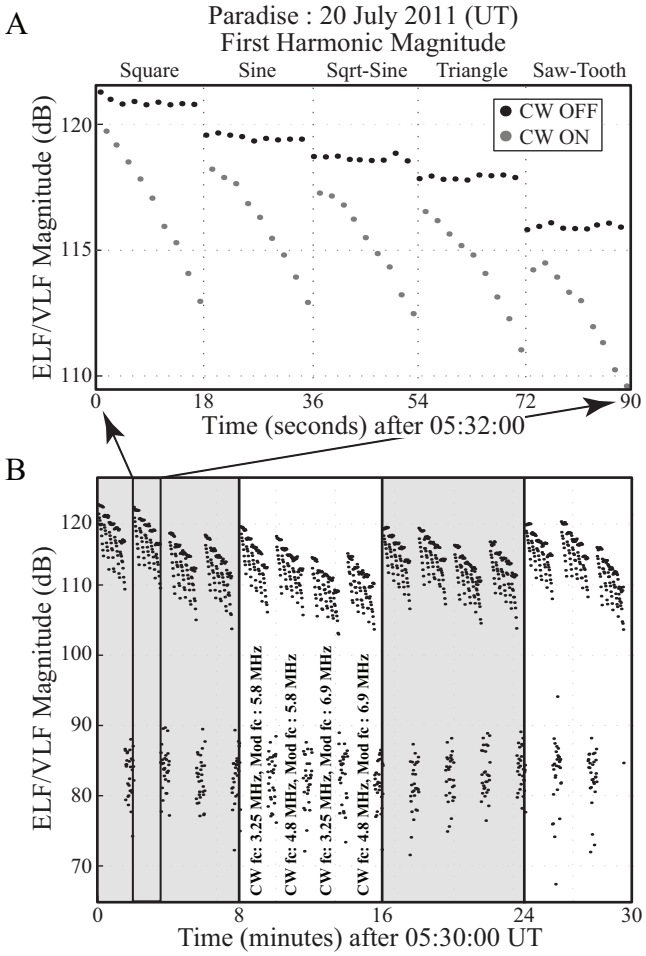

Figure 4-4. (A) 1225 Hz signal magnitudes over a 90-second transmission period. (B) 1225 Hz signal magnitude for the 30 minute transmission of 20 July 2011.

The data shown in Figures 4-2–4-4 are generally representative of our observations at all receiver sites and for all transmission periods, although the SNR varies with both time and site location. Table 4-1 summarizes the SNR observed at each receiver site for all days of observations during the transmission blocks. N/A entries indicate that the ELF receiver at Oasis had not yet been deployed to the site. To calculate the SNR levels shown in Table 4-1, the noise floor is approximated during periods when the HF transmitter is off.

In the following section, we provide detailed analysis of these observations as a function of CW power, HF frequency combination, modulation waveform, and receiver

Table 4-1. 1225 Hz SNR at each site for each day.

Date	Time	SNR (dB)		
(July 2011)	(UT)	PD	OA	SC
20	0530	13 - 30	N/A	10 - 20
21	0730	0	N/A	0
25	0730	5 - 30	5 - 20	0 - 20

location, and we compare the observations with the results of the dual-beam ionospheric HF heating model (Chapter 2).

4.3 Analysis

In this section, we compare observations with the predictions of the dual-beam HF heating model (Chapter 2) as a function of CW HF power, CW HF frequency, modulated HF frequency, modulation waveform, and receiver location. Experimental observations are used to demonstrate that the change in conductivity modulation (Figure 2-13) as a function of CW power is a measurable quantity that is sensitive to the ambient conditions of the D-region ionosphere. A theoretical analysis considering the cases of CW HF polarization and the modulation frequency of the modulated HF beam is also presented.

4.3.1 CW HF Power

The four panels of Figure 4-5 show the observed (black traces) and predicted (color traces) ELF wave magnitudes as a function of the effective radiated power (ERP) of the CW beam, with the four panels corresponding to the four Beam 1/Beam 2 HF frequency combinations employed. We point out that the scales of the four panels are different in order to clearly depict each of the traces within each panel. The predictions for all twelve combinations of electron density and electron temperature profiles are shown for each case, and each trace has been normalized so that 0 dB corresponds to the 1225 Hz magnitude observed during periods with the CW beam OFF. As mentioned previously, this normalization cancels the effects of the Earth-ionosphere waveguide to first order and provides a means to account for the variation in electrojet field strength over the course of the experiment [*Barr and Stubbe*, 1993].

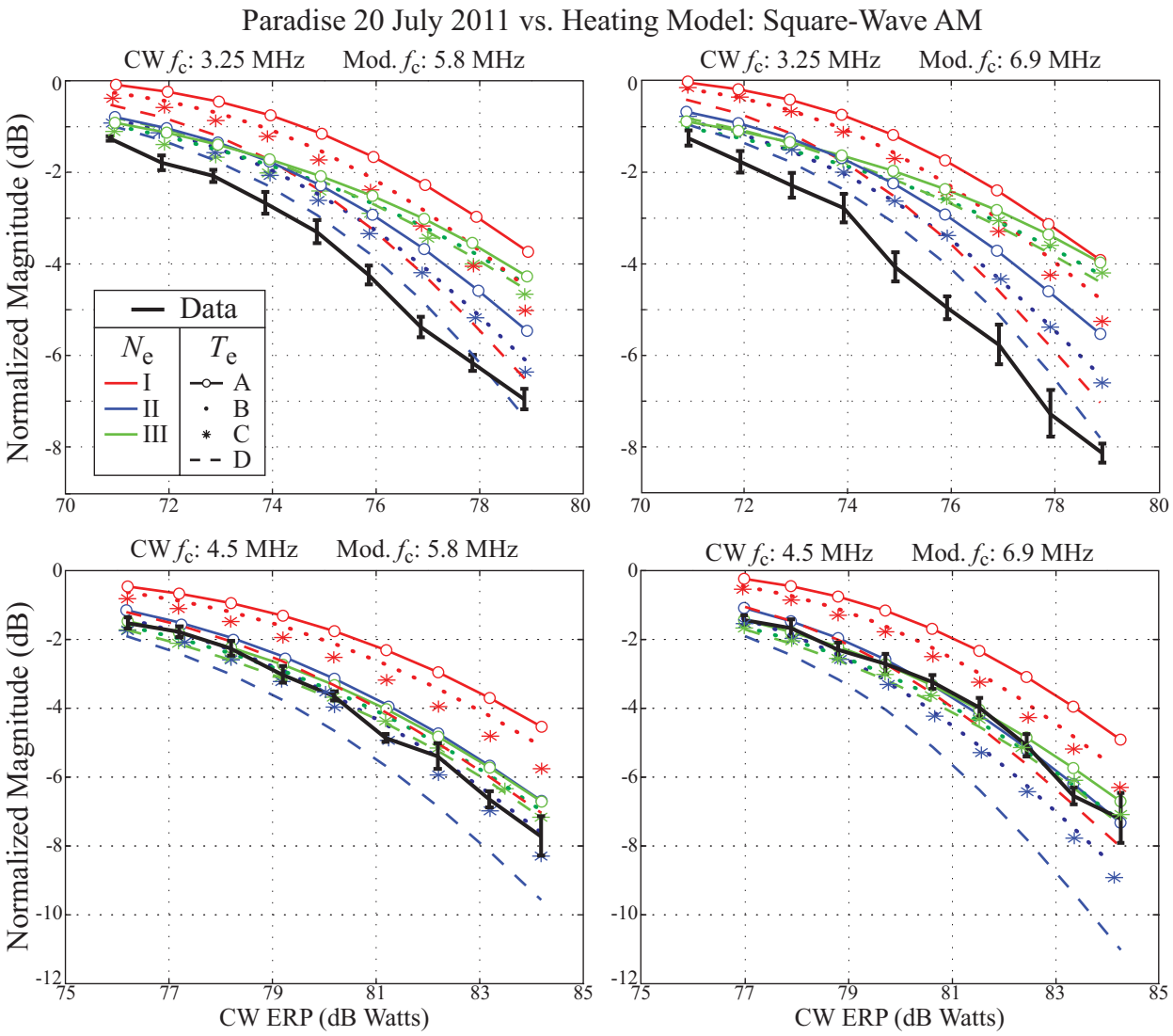

Figure 4-5. 1225 Hz signal magnitude observed at Paradise (solid black) together with dual-beam HF heating model predictions (color) for square-wave amplitude modulation. The four panels present results for four different Beam 1/Beam 2 HF frequency combinations and for twelve different N_e/T_e profile combinations.

First considering only the experimental observations, all four traces exhibit similar variations with CW ERP: the normalized ELF magnitude decreases as a function of increasing CW ERP, and the rate of decrease increases with increasing CW ERP. Although we have only shown the first repetition of 20 July 2011 for each frequency combination on this figure, all other iterations of the experiment exhibit these same characteristic features. For all power levels with the CW beam ON, the normalized magnitudes at 1225 Hz are less than those observed during periods with the CW beam OFF, consistent with the observations reported by *Moore and Agrawal* [2011]. Comparing the left and right panels of Figure 4-5 (i.e., for constant CW HF frequency), subtle differences exist between the observations as a function of CW power, and we will consider these differences in detail in subsequent subsections. Comparing the top and bottom panels (i.e., for constant HF frequency of the modulated wave), it is evident that for a given ERP value, the 3.25 MHz CW signal suppresses the ELF magnitude to a greater extent ($\sim$2 dB) than does the 4.5 MHz CW wave. We will consider this dependence in greater detail in Section 4.3.2.

Now considering the model predictions together with the experimental observations, Figure 4-5 clearly demonstrates that all traces (both experimental and theoretical) exhibit a similar dependence on CW ERP: the normalized ELF magnitude decreases as a function of increasing CW ERP, and the rate of decrease increases with increasing CW ERP. In general, the predicted ELF magnitudes show good agreement with observations, although specific details of the traces clearly depend upon the specific ambient electron density and electron temperature profile employed. Nevertheless, comparing the left and right panels of Figure 4-5 (i.e., for constant CW HF frequency), the differences between model predictions as a function of Beam 1 frequency are very similar to those exhibited by the observations. Furthermore, comparing the top and bottom panels (i.e., for constant HF frequency of the modulated wave), the model predicts that the 3.25 MHz CW signal will suppress the ELF magnitude to a greater

extent ($\sim$2 dB) than the 4.5 MHz CW wave for a constant ERP level, strikingly similar to observations.

Having compared experimental observations with theoretical predictions as a function of CW power, we continue our analysis by comparing results as a function of the HF frequency of the CW beam.

4.3.2 CW HF Frequency

Panel A of Figure 4-6 presents experimental observations of the 1225 Hz signal magnitude performed on 20 July 2011 (solid traces) and on 25 July (dashed traces) at Paradise (PD) as a function of CW ERP. The power steps for the two different CW frequencies employed span two distinct ERP ranges. In order to determine the dependence on CW frequency, we compare the 3.25/5.8 (red) traces with the 4.5/5.8 (green) traces and the 3.25/6.9 (blue) traces with the 4.5/6.9 (purple) traces. The observations performed on 20 July 2011 exhibit nearly identical dependencies on CW ERP (after discounting for the different CW frequency-dependent gains): the initial suppression offset and the spread of suppression as a function of CW power, as defined in the figure, are essentially the same. Observations performed on 25 July 2011, under different ambient ionospheric conditions, however, clearly indicate that the suppression offset is $\sim$1–2 dB greater for 3.25 MHz than for 4.5 MHz and that the suppression spread as a function of CW ERP is $\sim$1–2 dB greater for 3.25 MHz than for 4.5 MHz. In this case, the suppression offset and the spread are both different as a function of HF frequency combination. These experimental observations indicate that the received ELF magnitude as a function of CW frequency is sensitively dependent upon the ambient ionospheric conditions.

Panel B of Figure 4-6 presents model predictions for four different ionospheric profile combinations (I-A, II-C, II-D, and III-A). The level of ELF magnitude suppression differs as a function of CW frequency, and this difference changes as a function of ionospheric profile combination, dependent upon both the ambient electron density

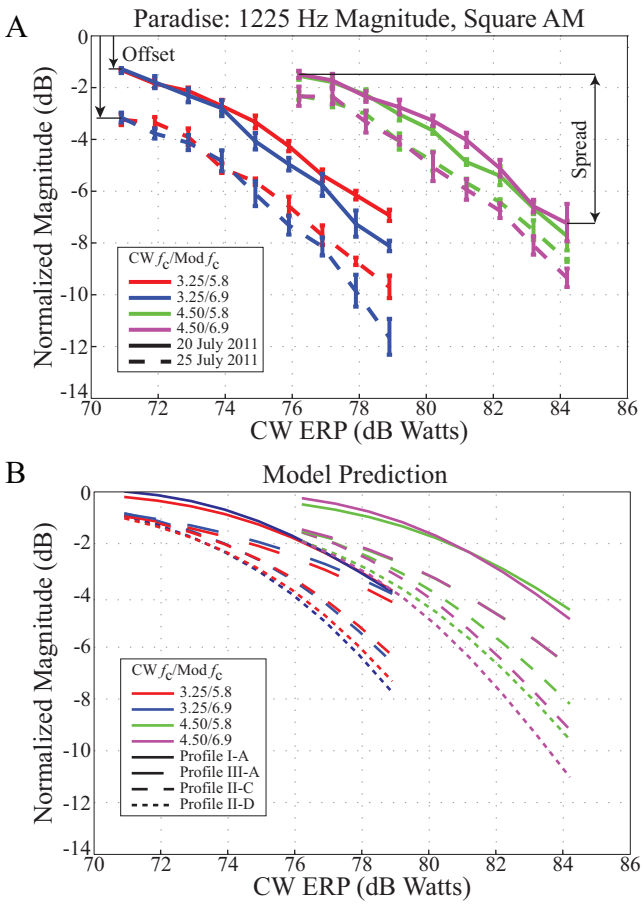

Figure 4-6. Normalized ELF magnitude as a function of CW ERP, highlighting the effects of Beam 1 (modulated) and Beam 2 (CW) HF frequency for (A) Observations at Paradise on 20 and 25 July 2011. (B) Model Predictions.

and electron temperature profile employed. Modeling results exhibit both small and large differences in suppression offset and spread as a function CW frequency. We expect that a different set of ionospheric profiles will reproduce the large ($\sim$3-dB) initial suppression offset observed on 25 July 2011, although we have made no effort to do so here. Most importantly, both observations and model predictions indicate that the level of ELF magnitude suppression by additional CW heating sensitively depends on the frequency of the CW signal and on the ionospheric conditions.

Having compared experimental observations with theoretical predictions as a function of CW HF frequency, we continue our analysis by comparing results as a function of the modulated HF frequency.

4.3.3 Beam 1(Modulated) HF Frequency

We continue to refer to Figure 4-6 to investigate the dependence on the modulated (Beam 1) HF frequency. In this case, we compare the 3.25/5.8 (red) traces with the 3.25/6.9 (blue) traces and the 4.5/5.8 (green) traces with the 4.5/6.9 (purple) traces. On a given day and for a given CW HF frequency, the normalized ELF magnitude for 5.8 MHz is extremely similar to that for 6.9 MHz. For both CW frequencies (3.25 and 4.5 MHz), the differences in ELF magnitude suppression are nearly negligible at low CW power levels. For a CW frequency of 3.25 MHz, at higher ($>$74 dBW ERP) CW power levels, the signals generated using 6.9 MHz are slightly more suppressed than those generated using 5.8 MHz, with the difference in suppression increasing with increasing CW power up to a maximum difference of 0.5–1.0 dB (depending on the day, and thereby ambient ionospheric conditions). For a CW frequency of 4.5 MHz, similar differences are observed at higher CW power levels ($>$80 dBW ERP), although the difference in the level of suppression is less than for the 3.25 MHz CW signal, maximizing at $\sim$0.25 dB.

The model predictions for the four different ambient ionospheric conditions shown in panel B of Figure 4-6 exhibit the same general trends exhibited by the experimental observations: the difference in the level of suppression between Beam 1 frequencies increases with increasing CW power. For the ambient ionospheric combinations considered, the predictions indicate that ELF signals generated using 5.8 MHz may be more or less suppressed than those generated using 6.9 MHz. Additionally, 3.25 MHz may create larger or smaller differences than 4.5 MHz, depending on the ionospheric profile combination. At the highest CW power levels, the difference in suppression may be as high as 1.0 dB, also depending on the ambient ionospheric profile combination employed. Based on both experimental observations and theoretical predictions, we conclude that while the dependence on Beam 1 (modulated) HF frequency is measurable at these CW power levels, significant ($\sim$1-dB) differences are detectable

only at higher CW power levels, when the ELF SNR is lower (and the error bars are higher). As a result, the difference in CW suppression as a function of Beam 1 frequency is a difficult measurement to perform in practice.

Having compared experimental observations with theoretical predictions as a function of Beam 1 (modulated) HF frequency, we continue our analysis by comparing results as a function of amplitude modulation (AM) waveform.

4.3.4 Modulation Waveform

The left panel of Figure 4-7 shows the normalized average ELF magnitude experimentally observed as a function of AM waveform on 20 July and 25 July 2011. These particular measurements were performed during CW-OFF periods, and they are normalized by the first Fourier harmonic component of the respective ideal signal waveforms, taking the average square-wave signal magnitude as a 0-dB reference. Accounting for the error bars, shown in gray, the difference in normalized signal magnitude measured between the two days varies between $\sim$0.10 and $\sim$0.80 dB as a function of modulation waveform, with the largest difference occurring for the saw-tooth waveform. We note that the 20 July 2011 observations are larger than the 25 July 2011 observations for all modulation waveforms. Because the transmission format did not change between the two days, these differences are attributable to the different ambient ionospheric conditions on the two days. The model predictions for the normalized ELF magnitude as a function of electron density (for electron temperature Profile A) are shown in the right panel of Figure 4-7. The model predictions exhibit variations as a function of ionospheric profile combination, with the largest ($\sim$0.80-dB) variations occurring for the triangle waveform. Comparing observations with the predictions of the theoretical model, all experimentally measured values are within $\sim$0.5-dB of the theoretical results, with the worst correspondence occurring for the sqrt-sine modulation waveform. Considering that a CW beam is not required to perform this measurement, the SNR does not significantly suffer as a result (as opposed to the Beam 1 frequency

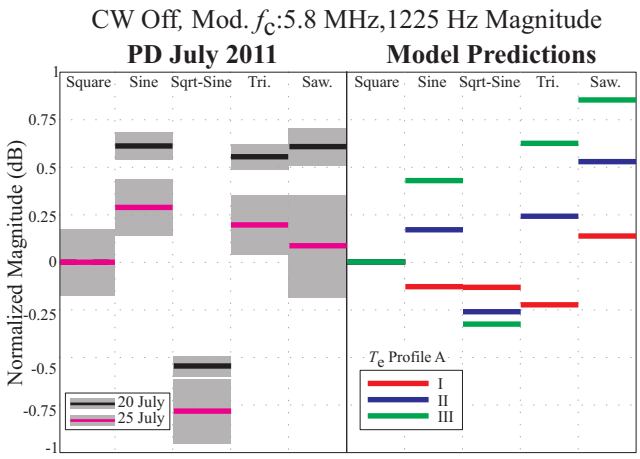

Figure 4-7. CW-OFF: ELF magnitude as a function of modulation waveform, normalized by the magnitude generated for square AM.

case). It thus appears to be the case that careful observations of the relative magnitudes generated using different AM waveforms may yield independent information regarding the ambient ionospheric conditions.

Now considering the effects of additional CW heating, panel A of Figure 4-8 shows the normalized ELF magnitude at 1225 Hz as a function of CW power for a constant Beam 1 HF frequency of 5.8 MHz. The observations are presented for both 20 July (solid traces) and 25 July (dashed traces). On both days, the normalized ELF magnitude for all five AM waveforms produce nearly identical results at all CW ERP levels, with the singular exception of the square-wave modulation case for 5.8/4.5 MHz on 20 July. The results for a Beam 1 HF frequency of 6.9 MHz (not shown) are similar in all respects. Panel B of Figure 4-8 shows the model predictions for the five AM waveforms as a function of CW ERP, using two different sets of ambient ionospheric conditions (I-A and II-D). The predictions for both sets of ambient profiles exhibit extremely similar variations of ELF magnitude for all five modulation waveforms as a function of CW ERP, with the largest offsets (only $\sim$0.25-dB) occurring for the triangle and saw-tooth waveforms. Based on these results, we conclude that additional CW power does not provide additional independent information about the ambient ionospheric conditions as a function of the modulation waveform. Considering the effects of CW heating on

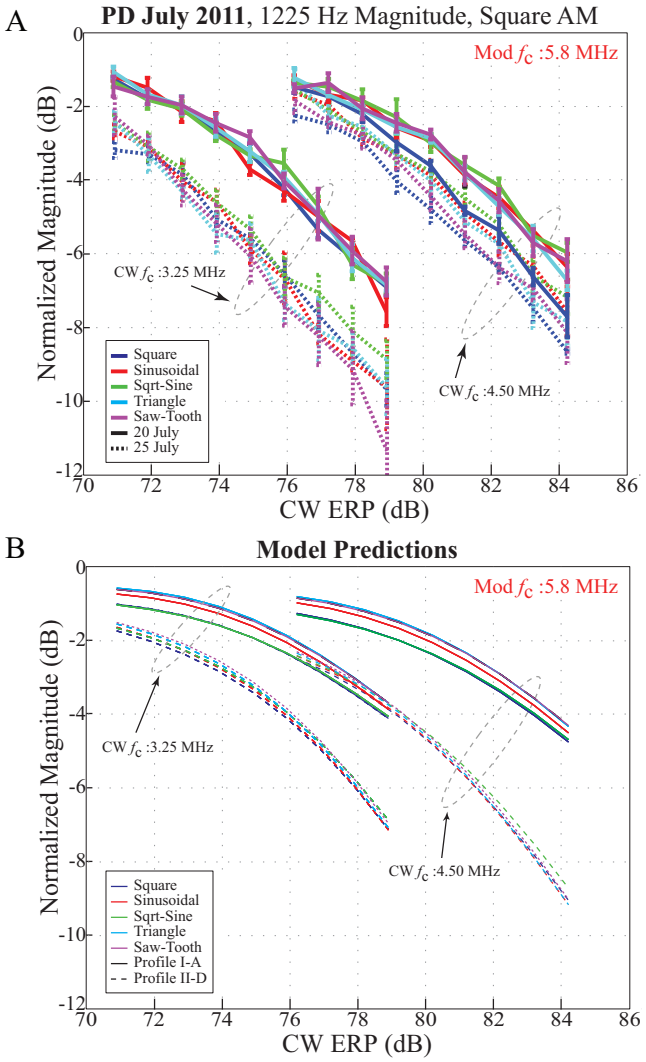

Figure 4-8. ELF magnitude as a function of CW ERP for five AM waveforms for CW f_c 3.25 MHz and modulated f_c 5.8 MHz for (A) experimental observations and (B) model predictions. Only very subtle variations in ELF magnitude are observed as a function of AM waveform.

the higher-order harmonic content produced as a function of modulation waveform is beyond the scope of this chapter.

In the following section, we compare observations and model predictions for different ELF receiver locations as a function of CW power.

4.3.5 Receiver Location

Panel A of Figure 4-9 shows the normalized ELF signal magnitude observed at at Sinona Creek (SC, 33 km from HAARP) and at Paradise (PD, 98 km from HAARP)

on 20 July 2011 as a function of CW ERP for the four combinations of HF frequencies employed. Note that two sets of traces in the top two panels have been falsely offset by 2 dB and two sets of model predictions (bottom panel) have been offset by 1 dB for aesthetic purposes in order to facilitate the comparison as a function of receiver location. The normalized ELF magnitudes observed at the two locations are essentially the same (within the error bars) for all CW power levels and all HF frequency combinations. The error bars for the Sinona Creek measurements are high ($>$2 dB in some cases), however. The deployment of an ELF receiver at Oasis (OA, 3 km from HAARP) enabled high SNR measurements at two receiver sites on 25 July 2011. Panel B of Figure 4-9 shows the normalized ELF observations at Paradise and Oasis on 25 July. For the Beam 2 CW frequency of 4.5 MHz, the observations are very similar at the two sites and the error bars overlap at almost all CW power levels. The same is not true for the Beam 2 CW frequency of 3.25 MHz. At low ($<$76 dB) CW power levels, the ELF magnitude generated by 5.8 MHz observed at Paradise is lower than that observed at Oasis by $\sim$1 dB. The difference decreases with increasing CW ERP. A similar variation is observed for the 6.9 MHz signal below 73 dB ERP, although the maximum difference is less than 0.25 dB. Panel C of Figure 4-9 shows the predicted normalized ELF magnitude as a function of CW ERP at all three ground based receivers. The model predictions are in general agreement with the observations, except at low power levels, and show that the normalized ELF magnitudes are expected to have comparable levels as a function of receiver location. We attribute the deviation observed at Paradise for low CW ERP levels to the effects of the Earth-ionosphere waveguide and possibly to the generation of secondary ionospheric currents [*Payne et al.*, 2007], neither of which are accounted for by our propagation model. Earth-ionosphere waveguide effects are expected to be important at receiver locations greater than $\sim$75 km from HAARP [*Payne*, 2007], and Paradise is 98 km distant.

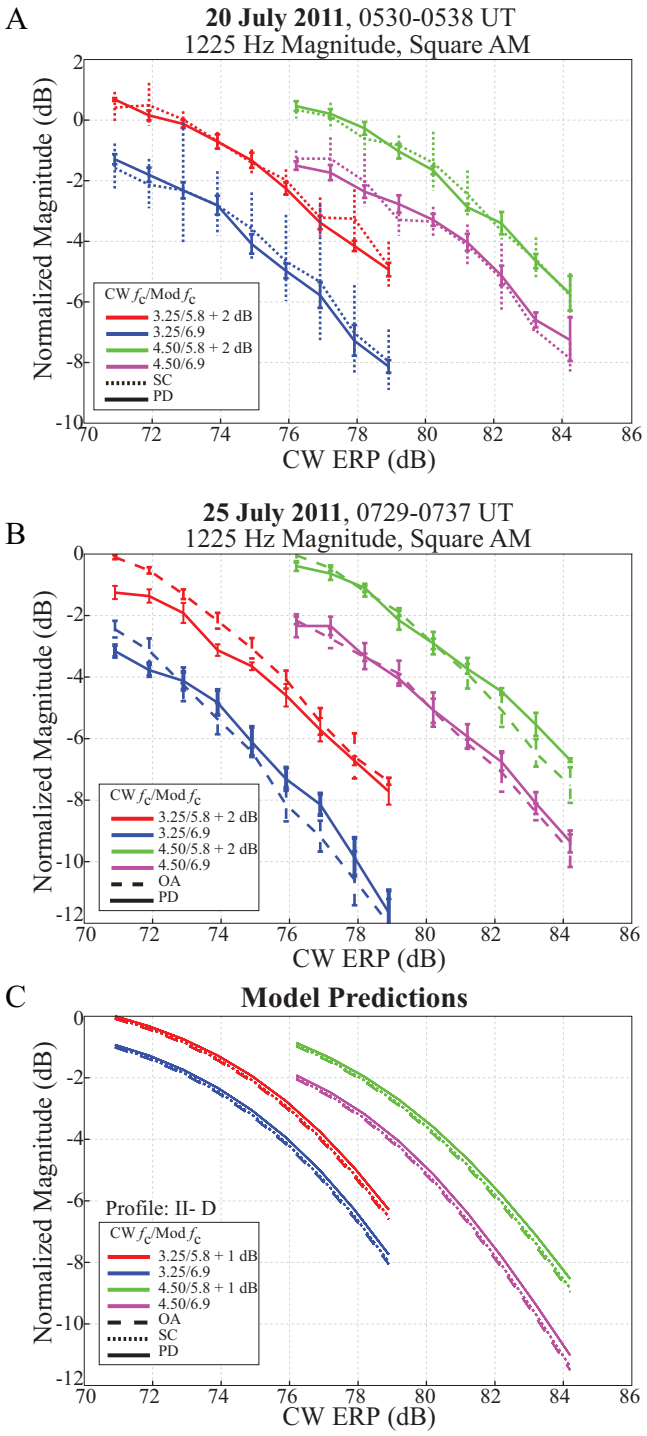

Figure 4-9. The normalized ELF magnitude as a function of ELF receiver location for (A) Observations on 20 July 2011, (B) Observations on 25 July 2011 and (C) Model Predictions. Red and green traces have been offset vertically to facilitate visual comparison between the traces.

It is interesting to note that at higher CW ERP levels and for higher CW HF frequencies, the observations presented in Figure 4-9 are very much in line with model predictions. We hypothesize that the altitude of the ELF source region plays a role in determining the relative importance of Earth-ionosphere waveguide effects at the receiver site. For instance, *Moore and Agrawal* [2011] showed (theoretically) that additional CW heating increases the altitude of the effective ELF source region. Furthermore, the ELF source produced by modulated heating at higher HF frequencies is expected to occur at somewhat higher altitudes than for lower HF frequencies [*Stubbe and Kopka*, 1977]. Lastly, higher altitude sources are expected to excite the Earth-ionosphere waveguide less effectively than lower altitude sources [e.g., *Tripathi et al.*, 1982]. Together, these considerations may explain the normalized ELF magnitudes observed at Paradise for low and high CW ERP levels.

Based on the observations and theoretical modeling, we conclude that additional measurements at receiver locations within $\sim$75 km of HAARP will not contribute a significant amount of additional information about the ambient D-region ionosphere. Nevertheless, additional observations at locations greater than $\sim$100 km from HAARP could possibly provide more information regarding other effects, such as those related to the Earth-ionosphere waveguide or to secondary ionospheric currents.

Having completed our comparison of experimental observations with model predictions, we now present theoretical predictions for the normalized ELF magnitude as a function of the polarization of the CW HF beam and the modulation frequency of the modulated beam.

4.3.6 Polarization

In this section, we theoretically investigate the effects that are produced by changing the polarization of the CW beam, as opposed to that of the modulated HF beam. Figure 4-10 shows the model predictions for CW heating using both X- and O-mode polarizations for the CW beam. Results for two ionospheric profile combinations

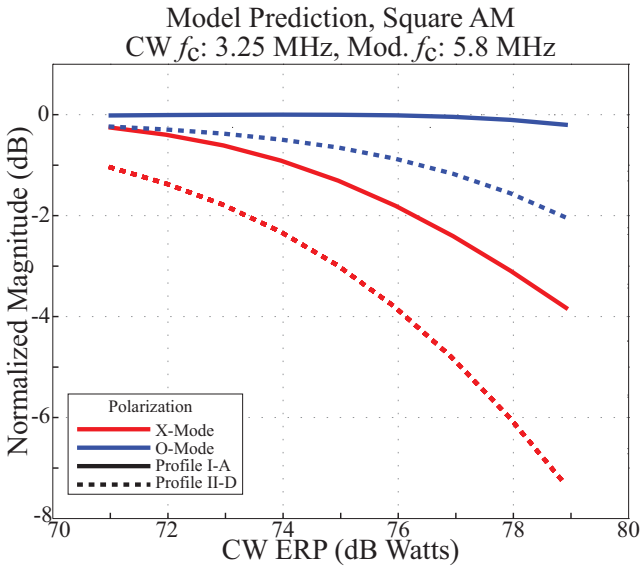

Figure 4-10. Theoretical predictions for normalized ELF magnitude as a function of CW HF beam polarization (X- vs. O-mode).

(I-A and II-D) are presented. In both cases, O-mode CW heating suppresses the normalized ELF magnitude to a lesser extent than X-mode heating. For Profile I-A, O-mode heating appears to have an almost negligible effect on the ELF magnitude, whereas for Profile II-D, O-mode heating produces 2 dB of suppression at the highest CW ERP level. Based on these model predictions, we suggest that the difference in the level of ELF magnitude suppression produced by X-mode and O-mode CW heating 1) is measurable, and 2) produces independent information regarding the ambient ionospheric conditions. For instance, for Profile I-A, the difference in the suppression produced by X- and O-mode CW heating increases with CW ERP from $\sim$0.25 dB at the lowest CW ERP level to $\sim$3.5 dB at the highest CW ERP level. For Profile II-D, the difference increases from $\sim$0.75 dB to $\sim$5.5 dB. Additionally, the suppression offsets and spreads are significantly different ($>$3 dB), especially at high CW power levels. Measurements comparing X- and O-mode CW suppression could significantly contribute to an analysis of ambient ionospheric conditions.

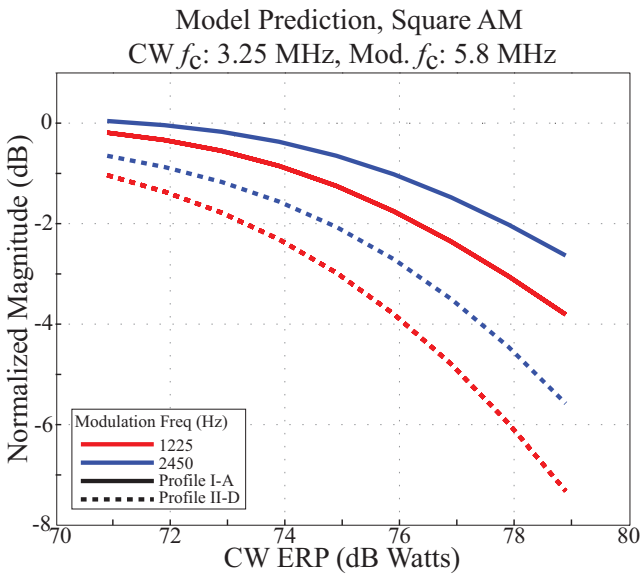

Figure 4-11. Theoretical predictions showing the normalized ELF magnitude for different modulation frequencies.

4.3.7 Modulation Frequency

Figure 4-11 shows the predicted ELF magnitude as a function of CW ERP for two different modulation frequencies and for two different ambient ionospheric profile combinations. For both modulation frequencies, increasing the CW power increases the level of ELF magnitude suppression, and for both ionospheric profiles, the signal generated using the higher modulation frequency is suppressed to a lesser extent. The difference in suppression (as a function of modulation frequency) increases from $\sim$0.25 dB at the lowest CW power level to 0.75–1.0 dB at the highest CW power level for both ionospheric profiles. While these differences as a function of CW power level are not as large as the differences produced by X- and O-mode heating, they are detectable. Nevertheless, the system response would need to be calibrated to a very tight tolerance at the different modulation frequencies to provide reliable observations as a function of modulation frequency. We thus conclude that while measurements comparing CW suppression as a function of modulation frequency and CW power can provide additional information regarding the ambient ionospheric conditions, such measurements would be difficult to perform reliably in practice.

4.4 Discussion

This chapter has compared experimental observations performed during power stepped dual-beam ELF wave generation experiments at HAARP to the predictions of a dual-beam ionospheric HF heating model. Comparisons were performed as a function of HF power, HF frequency, modulation waveform, and receiver location. Model predictions agree well with observations, demonstrating that the model incorporates the essential physics involved in multibeam HF heating of the lower ionosphere. We evaluated the sensitivity of the received ELF wave magnitude to these controllable parameters and interpreted the dependence on ambient ionospheric conditions. As a result, we have identified the types of transmissions that may provide a significant amount of information regarding the ambient conditions of the D-region ionosphere. While an inverse procedure to derive the ambient electron density and temperature profiles from these measurements remains to be presented, the observations and modeling presented herein strongly suggest that dual-beam ELF wave generation experiments can play an important role in a possible future D-region diagnostic.

We conclude by enumerating our experimental and theoretical results:

1. For high CW power levels, the introduction of additional CW heating reduces the amplitude of the received ELF wave. The rate of ELF magnitude suppression increases with increasing CW power.

2. The level of ELF magnitude suppression depends on the CW frequency employed, and the level of suppression as a function of CW frequency is sensitively dependent on the ambient ionospheric conditions.

3. The level of ELF magnitude suppression also depends on the frequency of the modulated HF beam, although to a lesser extent than the CW frequency.

4. The ELF signal magnitude as a function of modulation waveform (without CW heating) also depends on the ambient ionospheric conditions, whereas the suppression supplied by additional CW heating is extremely similar as a function of modulation waveform.

5. ELF receivers located at significantly different distances from HAARP (3–98 km) register similar normalized ELF magnitudes at high CW power levels. Differences

exist at lower CW power levels, and we attribute these differences to the effects of the Earth-ionosphere waveguide at larger distances.

6. A theoretical analysis predicts that O-mode CW heating may provide additional independent information to observations performed using X-mode CW heating and that these observations are sensitively dependent on the ambient conditions of the *D*-region.

7. Lastly, we predict that the effect of CW heating will decrease with increasing modulation frequency.

CHAPTER 5
TIME-OF-ARRIVAL (TOA) MEASUREMENTS AS A MEANS TO DETECT *D*-REGION STRUCTURE

Chapter 4 identified the types of HF transmissions that can be used to provide significant information regarding the ambient characteristics of the *D*-region ionosphere. One of the major difficulties in providing a *D*-region diagnostic using these parameters is simply to separate the effects of electron density and electron temperature. In this chapter, we demonstrate that N_e and T_e effects *cannot* be fully decoupled in general. Nevertheless, we determine that linear T_e variations with altitude produce a minimal impact on the modeling of ELF waves generated using dual-beam heating, allowing for a best-fit electron density profile to be calculated in a straight-forward manner. This class of electron density solutions necessarily assumes a linear electron temperature variation with altitude. While we do not presume that the identified electron density and electron temperature profile uniquely match observations, we assert that the combination of the two may be used to provide insight into the structure of the lower ionosphere.

The identified method is applied to produce an electron density profile that accurately models the unusually large level of ELF magnitude suppression observed on 25 July 2011. These observations are fairly accurately modeled, and the identified electron density profile produces a dominant ELF source altitude located at a sharp ridge in the electron density profile. This observation, in turn, leads to the investigation of ELF/VLF time-of-arrival (TOA) measurements as a means to provide additional information about the ambient *D*-region electron density profile. We demonstrate that TOA observations performed during dual-beam heating experiments are consistent with a structured electron density profile, and we provide a piecewise exponential N_e profile that closely matches the TOA observations.

The signal processing related to the TOA observations presented herein is the focus of a University of Florida Ph.D. thesis by Shuji Fujimaru. While this chapter makes

use of the TOA observations, the primary focus of this chapter is on the modeling of observations, specifically under dual-beam HF heating conditions.

5.1 Coupled Nature of N_e and T_e Profiles

Continuing with the type of numerical analysis presented in Chapter 4, we present numerical modeling results indicating that the suppression of ELF magnitude by additional CW heating depends sensitively on both the electron density and electron temperature profiles. Figure 5-1 presents summary charts of ELF magnitude suppression as a function of CW ERP, with the traces organized by electron density profile. It is clear that for electron density Profiles 1 and 2, the electron temperature profile employed significantly impacts the resulting ELF signal magnitude. For electron density Profile 3, however, the results are essentially independent of electron temperature, indicating that for larger D-region electron densities, the effects of electron temperature are minimized.

The results summarized in Figure 5-1 demonstrate that the electron temperature profile can produce changes in the magnitude offset of up to 0.25 dB and changes in the magnitude spread of up to 2.25 dB. Because similar results may be produced by slightly modifying either the electron density or electron temperature profile, it is clear that the electron density profile cannot be fully decoupled from the electron temperature profile. At the same time, modeling results indicate that the electron density profile dominates both the magnitude offset and the magnitude spread, with the effect of electron temperature being secondary.

With these results in mind, we undertake the task of identifying a class of electron temperature profile that minimally impacts the modeling results. From this perspective, an electron density profile may be identified and used to interpret the structure of the D-region ionosphere.

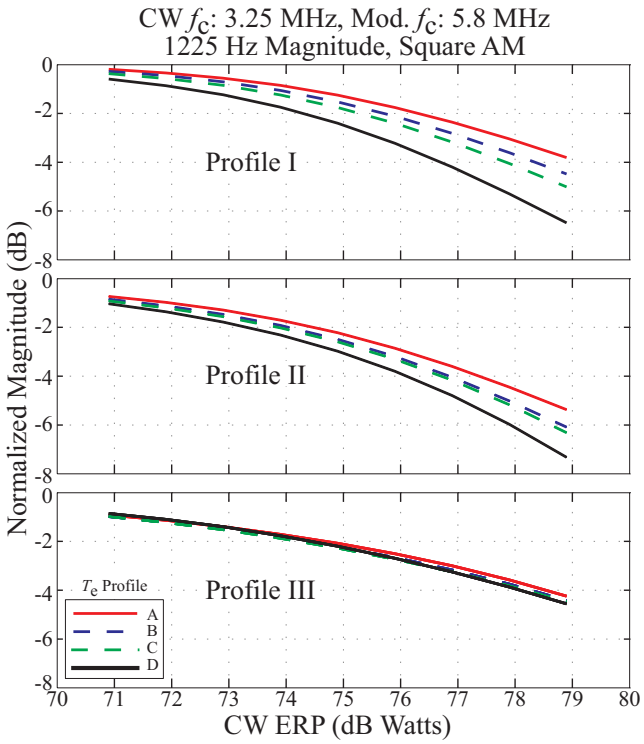

Figure 5-1. Model predictions for the normalized ELF magnitude as a function of electron density profile and electron temperature profile.

5.2 Linear T_e Profiles and Exponential N_e Profiles

In order to assess the sensitivity of ELF/VLF wave generation to the electron density and temperature profiles and to determine the conditions (if any) under which the effects of N_e and T_e may be decoupled, we evaluate the multibeam-HF heating model using a variety of exponential N_e profiles and linear electron temperature profiles with differing magnitudes and slopes.

The exponential electron density profiles are parameterized by h' (km) and β (km^{-1}), as given by *Wait and Spies* [1964]:

$$N_e(h) = 1.43 \times 10^7 \exp(-0.15h') \times \exp[(\beta - 0.15)(h - h')] cm^{-3} \qquad (5\text{–}1)$$

The *Wait and Spies* [1964] electron density profile has been successfully used in previous D-region works [e.g., *Cummer and Inan*, 1997; *Cummer et al.*, 1998; *McRae and Thomson*, 2000]. The parameter h' controls the magnitude of the electron density

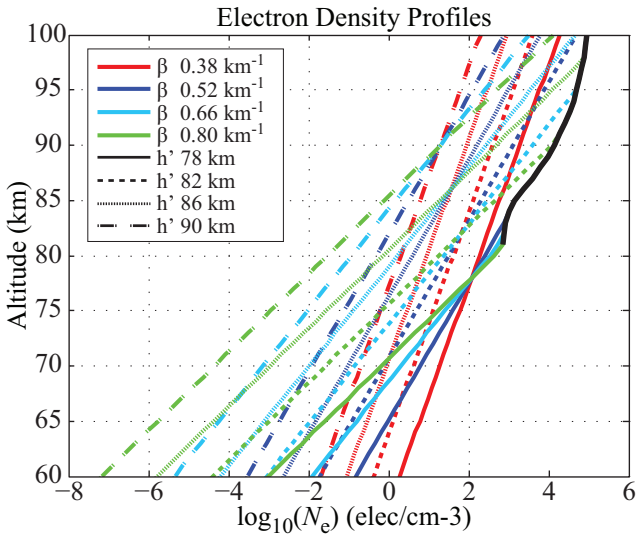

Figure 5-2. 16 unique exponential electron density profiles (plotted on log scale) obtained by varying parameters β and h'.

profile and β controls the slope of the profile on log-scale. In this work, we varied β from 0.38 to 0.8 and h' from 78 to 90 km in order to cover a complete range of reasonable electron densities consistent with a nighttime D-region ionosphere [e.g., *Moore et al.*, 2007; *Moore and Agrawal*, 2011; *Fujimaru and Moore*, 2011a]. Figure 5-2 shows the 16 distinct electron density profiles employed. In order to provide moderately realistic profiles, these profiles have been limited at higher altitudes ($>$ 80 km) by the maximum electron density calculated using the IRI calculator (`http://omniweb.gsfc.nasa.gov/vitmo/iri_vitmo.html`) for 20 August 2011 at 7.5 hours UT (denoted by the solid black trace). N_e profiles with the same color trace represent profiles with the same β value while profiles with the same line style represent the same h' values.

The T_e profiles employed vary linearly with altitude, with the parameters selected to cover the range delineated by profiles A, B, C, and D shown in Figure 5-3. Profiles A, B, C, and D are representative of the electron temperature profiles modeled over the course of a year using the MSISE-90 Atmosphere Model [*Moore and Agrawal*, 2011; *Agrawal and Moore*, 2012]. The eight profiles used in this work are shown in Figure 5-3. These profiles have been truncated by Profile A at lower altitudes to be more realistic.

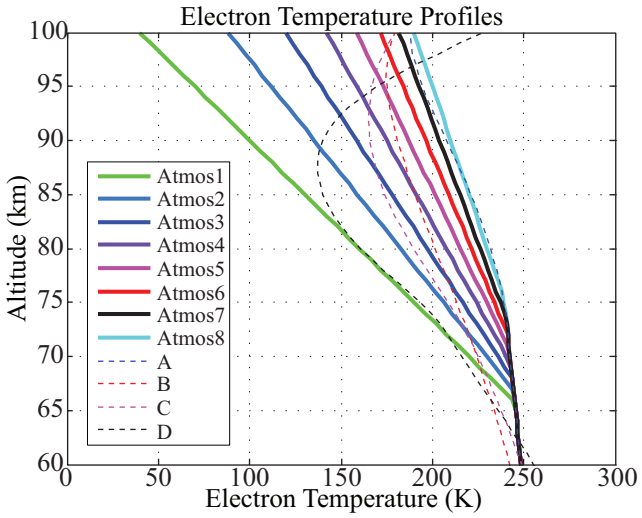

Figure 5-3. 8 unique linear electron temperature profiles obtained to cover the entire range of reasonable T_e profiles.

The normalized ELF magnitude predictions for all 128 combinations of exponential N_e and linear T_e profiles are shown in Figures 5-4 and 5-5. Figure 5-4 highlights the dependence on β, while Figure 5-5 highlights the dependence on h'. In each of the figures, the top panel shows the ELF magnitude with the CW beam OFF, while the middle and bottom panels show the ELF suppression offset and magnitude spread, respectively, as a function of β and h'. In order to simplify the displays, we have used error bars to represent the extremes of the predictions for the 8 linear T_e profiles. We note that the model predictions cover a wide range of detectable ELF magnitudes ($\sim$1 fT to 1 pT, top panel), suppression offsets (~ -1 to $+1$ dB, middle panel), and magnitude spreads (~ -8 to 0 dB, bottom panel).

Focusing on Figure 5-4, the different color traces represent the different h' values used to generate the exponential N_e profiles. Panel B of Figure 5-4 demonstrates that for a given h', the suppression offset has a complicated dependence on β: for $h' = 82, 86$, the offset increases and then decreases with β, while for $h' = 78, 90$, the offset increases monotonically with β. Panel C of Figure 5-4 demonstrates that for a given h', the magnitude spread generally increases with increasing β, with only one exception at $h' = 86$.

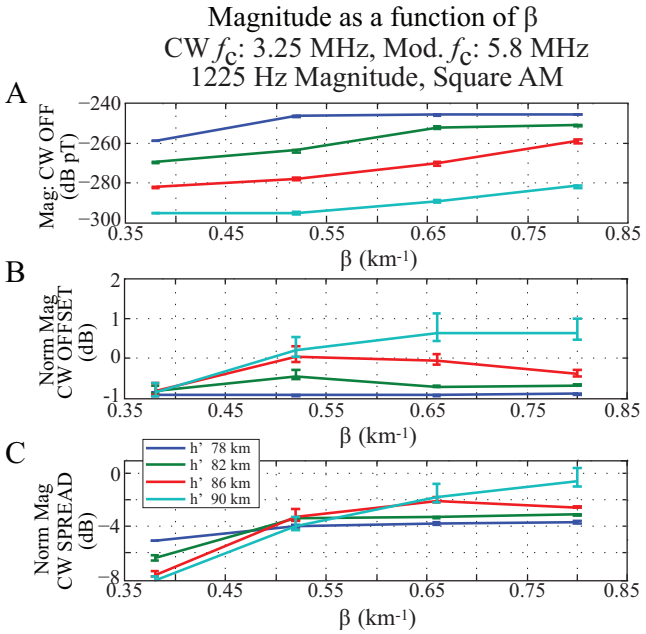

Figure 5-4. (A) ELF magnitude with CW beam turned off. (B) Normalized ELF initial suppression offset and (C) Normalized ELF suppression spread, as a function of β.

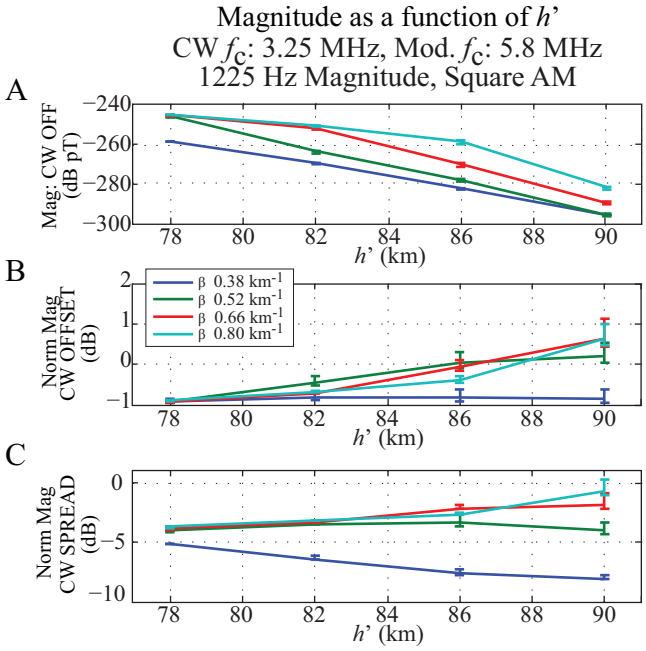

Figure 5-5. (A) ELF magnitude with CW beam turned off. (B) Normalized ELF initial suppression offset and (C) Normalized ELF suppression spread, as a function of h'.

Turning our attention to Figure 5-5, the different color traces represent the different β values used to generate the exponential N_e profiles. Panel B of Figure 5-5 demonstrates that for a given β, the suppression offset tends to increase with h', with the only exception being for $\beta = 0.38$ km^{-1}. Panel C of Figure 5-5 demonstrates that for a given β, the magnitude spread has a complicated dependence on h': for $\beta = 0.38$ km^{-1}, the magnitude spread decreases monotonically with h', for $\beta = 0.52, 0.66$ km^{-1}, the magnitude spread increases then decreases with increasing h', and for $\beta = 0.80$ km^{-1}, the magnitude spread increases monotonically with h'.

For both Figures 5-4 and 5-5, the displayed error bars indicate that the electron temperature profile has a minimal impact on the calculations. The electron temperature affects the suppression offset by at most 0.75 dB ($h' = 90$ km, $\beta = 0.66$ km^{-1}) and the magnitude spread by at most 1.25 dB ($h' = 90$ km, $\beta = 0.66$ km^{-1}). The figures demonstrate that the typical variation with electron temperature is much less than these two quoted values. Based on these modeling results, and considering that the typical SNR observed during dual-beam heating experiments is $\pm$0.5 dB, we conclude that electron temperature profiles that vary linearly with altitude do not significantly impact ELF wave generation calculations for comparison with experimental observations.

In the next section, we discuss how we can achieve additional ELF suppression offsets and magnitude spreads in order to match the observations performed on 25 July 2011.

5.2.1 Matching Observations on 25 July 2011

The range of β and h' shown in Figures 5-4 and 5-5 still do not account for the additional initial ELF suppression offset and magnitude spread observed on 25 July 2011 at OA, as discussed in Sections 4.3.2 and 4.3.5. Based on the model predictions shown in Figures 5-4 and 5-5, however, we conclude that decreasing β and h' together may closely match observations. Figure 5-6 shows the electron density profiles using βs of 0.1 and 0.05 and an h' of 90 km (blue dashed and blue dash-dot trace respectively).

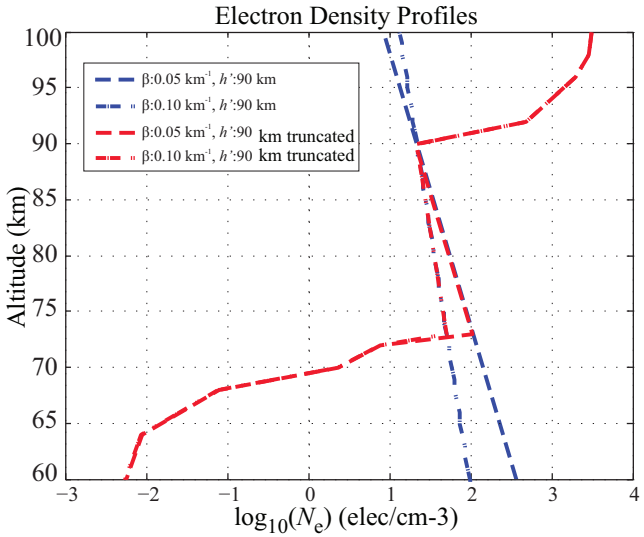

Figure 5-6. Exponential *Ne* at h' of 90 km with β of 0.05 and 0.10 km^{-1} (blue dashed and blue dash-bot respectively). Red dashed and red dash-dot traces represent the profiles truncated by realistic profiles, I, II and III (left panel of Figure 2-1).

These profiles have decreasing slopes throughout the *D*-region ionosphere. In order to make these profiles more realistic, we interpret the decreasing slope as indicating that ledges exist at the lower and upper portions of the profiles. We thus bound the profiles using an average of Profiles II and III at the lower altitudes and Profile I at the higher altitudes. These profiles are represented by the red dashed and red dash-dot traces in Figure 5-6 respectively.

The normalized ELF magnitude predictions as a function of CW ERP for these profiles are shown in Figure 5-7. The experimental observations of normalized ELF magnitude observed on 25 July 2011 at OA are overlaid on this figure. The two N_e profiles exhibit significant additional suppression, both in terms of the ELF suppression offset and in terms of the magnitude spread. The modeling predictions match the observations reasonably well, and certainly provide a better match than the profile combinations used in Chapter 4 (model predictions from profile combination II-D, also overlaid on this figure). This analysis indicates that the dual-beam ELF wave generation experiment may be sensitive to *D*-region structure, as exhibited by the

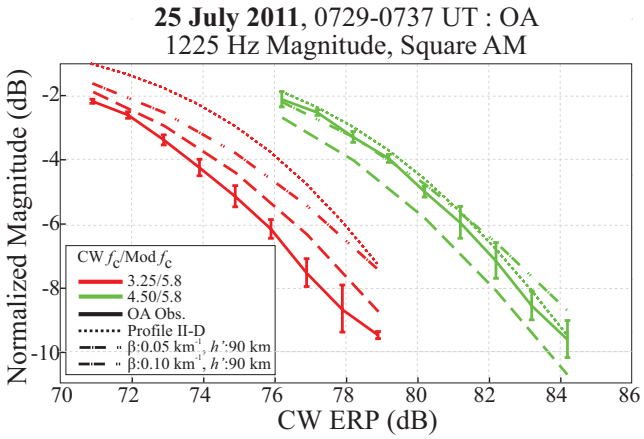

Figure 5-7. Normalized ELF magnitude at 1225 Hz as a function of CW ERP for 25 July 2011 at OA, observations for N_e profile with h' 90 km and β of 0.1 and 0.05 km^{-1}, (dashed and dotted respectively). Red and green traces represent CW f_c 3.25 and 4.5 MHz respectively with modulated CW f_c 5.8 MHz.

electron density ledges required to make the profile realistic. Without additional information, it is impossible to verify whether this structure indeed existed within the D-region ionosphere on 25 July 2011.

While performing this theoretical exercise, however, we noticed that the dominant ELF source region was located just above the lower ridge in electron density for all CW power steps. Figure 5-8 shows the Hall conductivity modulation generated in the ionosphere using a β of 0.1 km^{-1} and an h' of 90 km for CW OFF and CW ON (full power) transmissions. The white trace overlaid on each panel represents the N_e profile, while the white dot on each panel represents the altitude of the dominant source region. In both cases, the dominant source location is essentially at the lower N_e ridge at an altitude of $\sim$73 km. This theoretical result is a quantity that can be measured experimentally using ELF/VLF time-of-arrival (TOA) analysis [*Fujimaru and Moore*, 2011a], and the next section focuses on the TOA analysis of experimental observations in the context of the dual-beam HF heating experiment.

5.3 Dual-Beam ELF/VLF TOA Observations

Fujimaru and Moore [2011a] describe an ELF/VLF time-of-arrival (TOA) measurement method that requires modulating the ionosphere using a frequency-time ramp format,

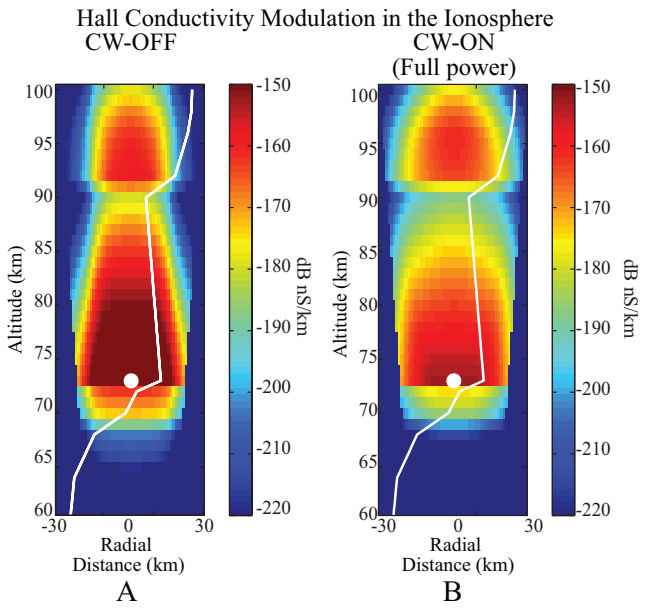

Figure 5-8. Modulated source region for Hall with CW-OFF (A) and Hall with CW at peak power (B) with altitude. Overlaid on each panel is the truncated N_e profile with β 0.1 km^{-1} and h' 90 km. The white dot on each panel represents the altitude of the respective dominant source regions.

rather than tones. The analysis of TOA observations leads to the ability to approximate the location of the dominant ELF/VLF source altitude. During a five minute period on 3 May 2012 between 07:35:30 and 07:40:00 UT, HAARP used a dual-beam heating configuration in which the HF array was split into two 6$\times$15 (1800 kW) sub-arrays. The first sub-array (Beam 1) modulated the ionosphere using a full-power 4.5 MHz (X-mode) beam that was square wave amplitude modulated with a linear 1$-$6 kHz frequency-time ramp (1 kHz/sec slope). At the same time, the second sub-array (Beam 2) broadcast a CW wave at 3.25 MHz. The peak power of Beam 2 decreased (in 3-dB steps) from 0 dB (full power) to $-$15 dB. The orientation of both beams was held vertical with respect to HAARP. Each CW power level was held constant for a five-second duration, and the CW transmission alternated between CW-OFF and CW-ON every five seconds in order to provide a means to evaluate changes in the electrojet field strength [*Barr and Stubbe*, 1993]. Data for five complete experiments was obtained during this time. The HAARP fluxgate magnetometer showed large disturbances and registered magnetic

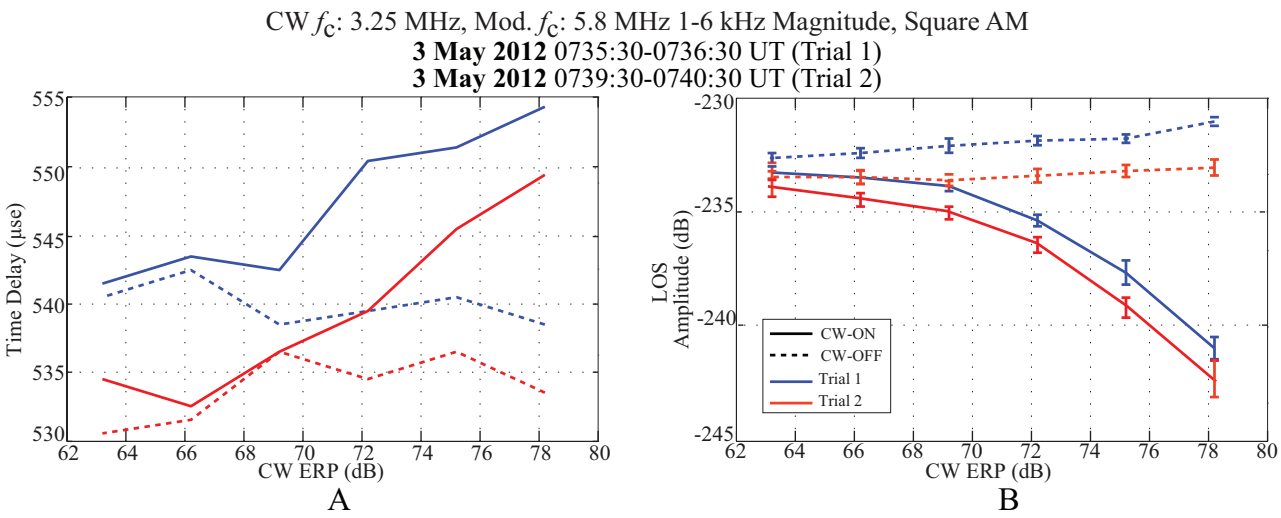

Figure 5-9. (A) Absolute TOA and (B) line of sight (LOS) magnitude observations as a function of CW ERP with CW beam turned ON (solid) and CW-OFF (dashed). Red and blue traces represent two trials of the experiment.

field fluctuations of between 75 nT and 100 nT during the transmission period. The k_p index was 2− at this time. Using the analysis method described by [*Fujimaru and Moore*, 2011b, Chapter 2], the ELF/VLF signals generated by the modulation of the ionosphere with frequency-time ramps are extracted.

Panels A and B of Figure 5-9 show the times-of-arrival and the ELF/VLF amplitudes detected during the dual-beam TOA experiment as a function of CW power respectively. In both panels, the blue and red traces correspond to two trials of the experiment, with solid and dashed traces representing observations with the CW beam turned ON and OFF respectively. The left panel demonstrates that the TOA increases with CW power between ∼530 μ-seconds and ∼555 μ-seconds. In terms of a dominant source altitude, this propagation time delay corresponds to a dominant ELF/VLF source altitude of ∼82 km with CW OFF. Panel B of Figure 5-9 demonstrates that the amplitude decreases with increasing CW ERP, exhibiting a maximum suppression of ∼7–8 dB, as expected. The ELF/VLF TOAs and amplitudes for CW OFF (dashed traces) are fairly constant during the entire duration of the experiment, indicating a fairly stable ionosphere and electrojet field strength.

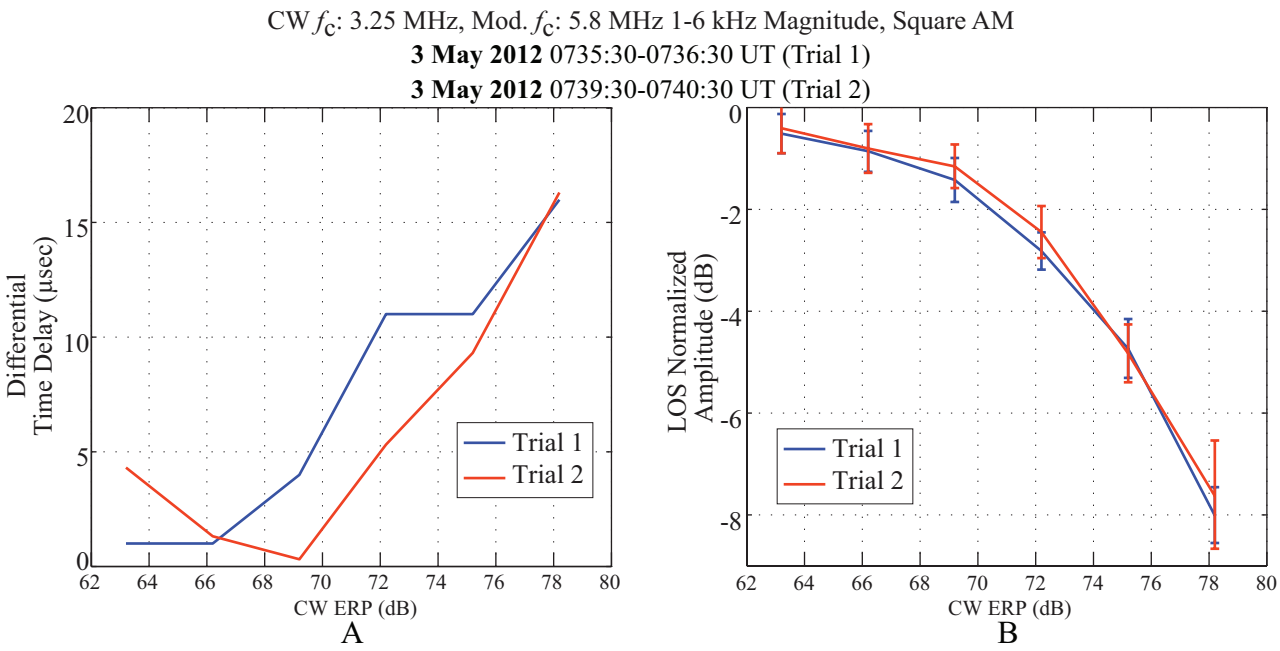

Figure 5-10. Relative TOA (A) and normalized LOS amplitude (B) observations with CW ERP. The red and blue traces represent the normalized observations from two trials of the experiment.

Figure 5-10 shows the relative change in TOA (referred to as TOA spread) and in ELF/VLF amplitude as a function of CW ERP for two trials of the dual-beam TOA experiment. In the left panel, both trials demonstrate that the normalized TOA increases with increasing CW ERP (by 16 μ-seconds), consistent with the predictions by *Moore and Agrawal* [2011] and indicating that the altitude of dominant source region increases by $\sim$2–3 km as a function of increasing CW ERP. The right panel shows that the normalized ELF/VLF amplitude decreases by $\sim$6.5–8.5 dB as a function of increasing CW ERP with reasonable error bars of $\sim\pm$ 0.4 dB at the lowest CW ERP level and $\sim\pm$ 1 dB at the highest CW ERP level.

We compare these observations with the predictions of the dual-beam HF heating model using exponential electron density profiles. The model is evaluated at the midpoint frequency of the frequency-time ramp, i.e., at 3500 Hz, using exponential N_e profiles with β varying from $-$ 0.1 to 0.8 km^{-1} and with h' varying from 78 to 86 km. Figure 5-11 shows the model predictions for the CW-OFF TOA, the TOA spread (TOA

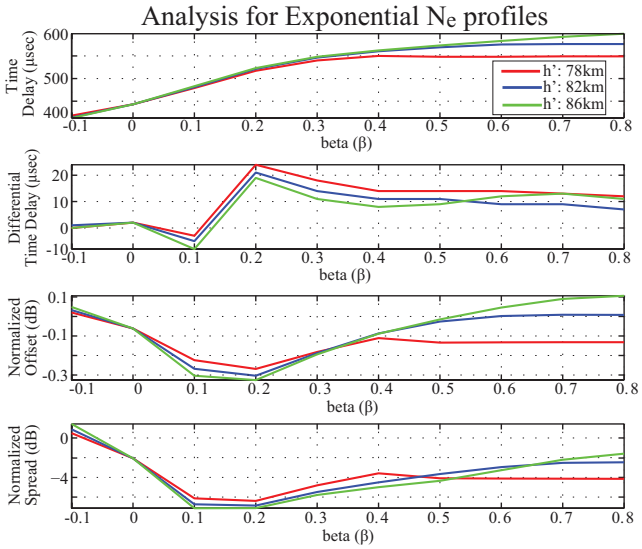

Figure 5-11. Analysis for exponential N_e as a function of β from -0.1 to 0.8, for h' 78, 82 and 86 km.

CW-ON 100% minus CW-OFF TOA), the initial ELF/VLF magnitude offset, and the ELF/VLF magnitude spread as a function of β. The different colored traces on each panel represent the three h's employed. The top panel of Figure 5-11 shows that the CW-OFF TOA increases with β for all h'. On the other hand, the TOA spread decreases until a certain β, experiences a sharp increase at $\beta \approx 0.2$, and then gradually decreases with increasing β. This is consistent for all h'. The opposite is true for the ELF/VLF magnitude offset and magnitude spread, however. Both quantities (shown in the bottom 2 panels of Figure 5-11) decrease until a certain β and then gradually increase. For β between 0.2 and 0.4, the values of CW-OFF TOA, TOA spread, ELF/VLF magnitude offset, and ELF/VLF magnitude spread lie within a reasonable range of the presented ELF/VLF TOA observations.

Figure 5-12 shows a zoomed view of Figure 5-11 for four h's varying from 78 to 90 km. Also shown in the right panel are the 16 exponential N_e profiles employed. The top 2 panels of Figure 5-12 demonstrate that the CW-OFF TOA and the TOA spread exhibit competing dependencies on β for all h's. As β increases, the CW-OFF TOA increases from $\sim$520 μ-seconds to $\sim$560 μ-seconds, whereas the TOA spread

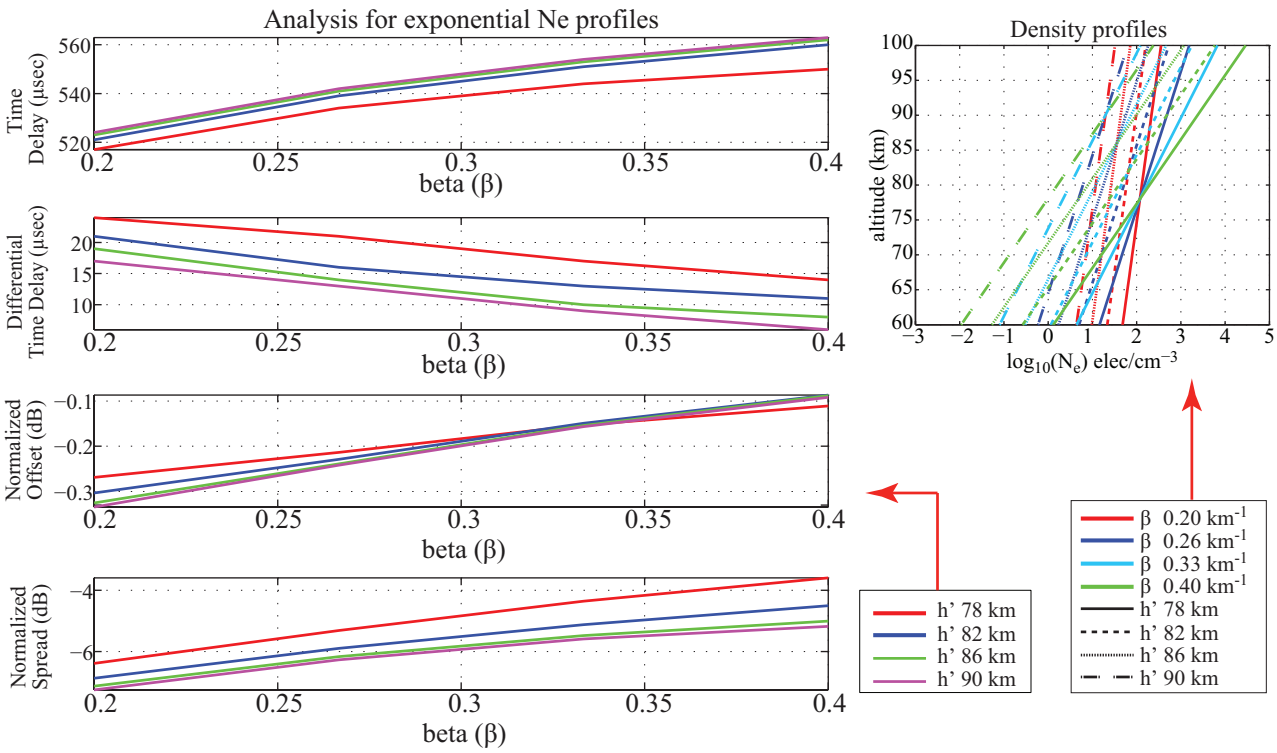

Figure 5-12. Analysis for exponential N_e as a function of β from 0.2 to 0.4, for h' 78, 82 and 86 and 90 km.

decreases with increasing β from ~20 μ-seconds to ~10 μ-seconds. The ELF/VLF magnitude offset and magnitude spread exhibit the same dependence on β, however: both quantities increase with increasing β.

Examining these results as a function of h', we notice that for a given β, the CW-OFF TOA (top panel) increases as h' increases from 78 to 90 km. Similarly, in the second panel, we observe that the TOA spread decreases with increasing h'. Lastly, in the bottom panel, it is demonstrated that the ELF/VLF magnitude spread becomes increasingly negative with increasing h'.

Although the modeling results for profiles with β between 0.2 and 0.4 and for h' between 78 and 90 km provide values for all four quantities that are within a reasonable range of observations, there does not exist a single profile among them that accurately matches all of the observations within error bars. Additionally, due to the trade off between CW-OFF TOA and magnitude spread, there is no clear direction in which

to modify the exponential profile – either in terms of β or in terms of h'. In order to overcome the competing affects of CW-OFF TOA, TOA spread, and magnitude spread, we consider the construction of a piecewise-exponential N_e profile in the next section.

5.3.1 Fitting a Piecewise-Exponential N_e Profile Using TOA

Based on the modeling results provided thus far, we propose the following method for identifying a piecewise exponential electron density profile that matches TOA observations. 1) Use the TOA dominant altitude as the initial guess for the altitude of intersection between the two profiles, 2) use the profile that best matches the TOA spread and magnitude spread as the initial guess for the lower portion of the profile, and 3) use the profile that best matches the CW-OFF TOA as the initial guess for the upper portion of the profile. Based on this description, we identify an initial intersection altitude of 82 km based on the TOA observations, and we use Figure 5-11 to identify the combination of $\beta = 0.2$ for the lower portion of the profile and $\beta = 0.33$ for the upper section of the profile. Once this initial guess profile has been identified, we iteratively modify the profile by adjusting 1) the β of the lower section, 2) the altitude of intersection, 3) the maximum electron density, and 4) the β of the upper section in order to best match the observations.

Tables 5-1 and 5-2 provide references for the observed and modeled parameters. The columns of the 'Piecewise-Exponential' section provides a summary of the iterations in order. The final iteration results in a CW-OFF TOA of 532 μ-seconds, a TOA spread of 16 μ-seconds, a magnitude offset of -0.30 dB, and a magnitude spread of -6.9 dB, all of which are within the error bars of the observations. In the following subsections, we step through each iteration and describe how the choices were made.

5.3.1.1 Lower Section β

Keeping the β and h' of the upper section (β_u and h'_u) fixed at 0.33 km^{-1} and 82 km respectively, and keeping the height of intersection h'_{int} fixed, we varied the β (β_l) of the lower section. The right panel of Figure 5-13 shows the lower section profiles that were

Table 5-1. Experimental TOA observations.

Parameters	Trial 1	Trial 2
Abs. TOA(μ sec)	540	**530**
Rel. TOA(μ sec)	16	**16**
Norm. offset(dB)	-0.50 ± 0.4	$-$**0.40**$\pm$**0.4**
Norm. spread(dB)	-8.0 ± 0.5	$-$**7.6**$\pm$**1**

Table 5-2. Piecewise-Exponential N_e.

Parameters	Exponential		Piecewise-Exponential				
β_l (km^{-1})	0.20	0.33	0.20	0.22	0.22	0.22	0.22
β_u(km^{-1})			0.33	0.33	0.33	0.33	0.33
h_{int} (km)			82	82	86	86	86
$\Delta log_{10}(N_e)$			0	0	0	-0.20	-0.22
Abs. TOA(μ sec)	524	551	522	534	529	**532**	534
Rel. TOA(μ sec)	21	13	31	24	20	**16**	19
Norm. offset(dB)	-0.30	-0.14	N/A	N/A	N/A	$-$**0.30**	-0.29
Norm. spread(dB)	-6.80	-5.1	-6.7	-6.2	-6.4	$-$**6.9**	-6.4

evaluated. The left panel of Figure 5-13 shows the variation of the three quantities as a function of β_l. Similar competing effects are observed for CW-OFF TOA, TOA spread, and magnitude spread as was described in association with the exponential electron density profiles. Nevertheless, we observe an improvement in the CW-OFF TOA (top left panel). Based on this analysis, we choose a β_l of 0.22 at this stage.

5.3.1.2 Altitude of Intersection (h'_{int})

Keeping the β and h' of the upper section (β_u and h'_u) fixed at 0.33 km^{-1} and 82 km respectively, and keeping the β_l fixed at 0.22 (as derived in Section 5.3.1.1), we varied the altitude of intersection of the two profile sections. The right panel of Figure 5-14 shows the profiles that were evaluated. The left panel of Figure 5-14 shows the variation of the three quantities as a function of h'_{int}. The same competing dependencies are once again observed for the CW-OFF TOA and the magnitude spread as was described above, but the TOA spread increases up to a certain h'_{int} after which it decreases with increasing h'_{int} (middle panel). We see a significant improvement in magnitude spread

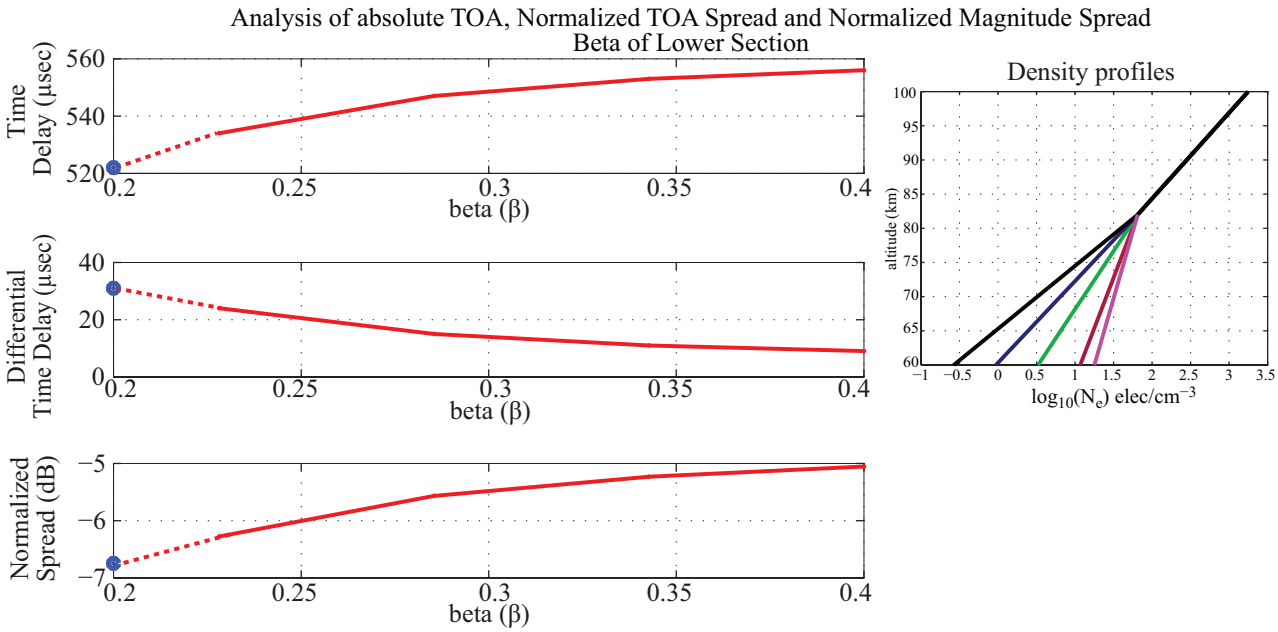

Figure 5-13. Beta of lower section.

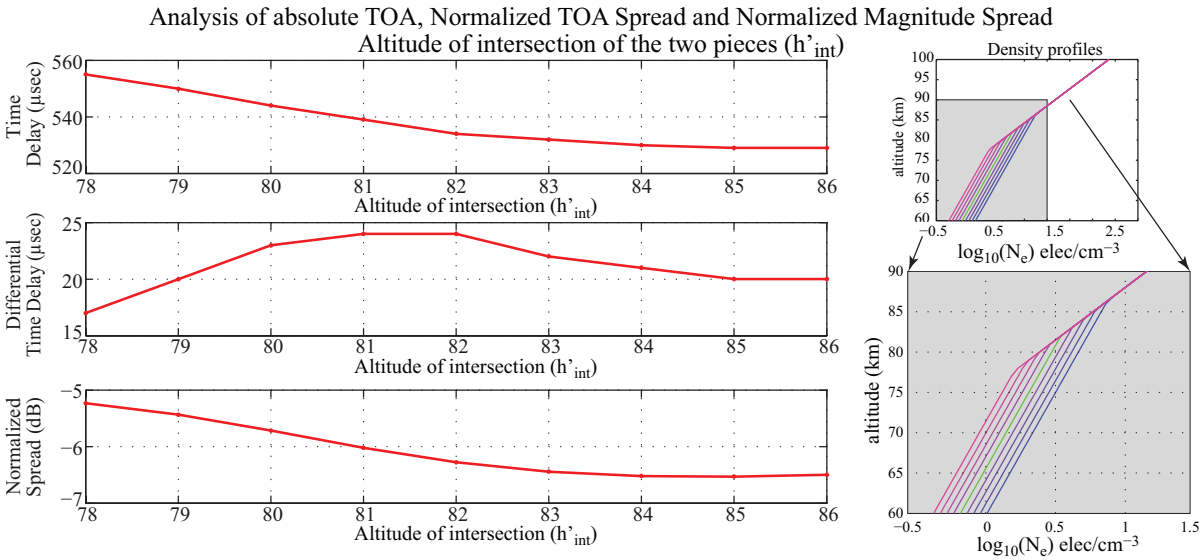

Figure 5-14. Altitude of intersection of the two pieces.

(bottom left panel), however, that is worth the trade off in CW-OFF TOA. As a result, we select an h'_{int} of 86 km at this stage.

5.3.1.3 The Magnitude of N_e

Keeping the βs of both sections (β_u and β_l) fixed at 0.33 km^{-1} and 0.22 km^{-1}, respectively, and keeping the altitude of intersection of the two pieces at 86 km, we

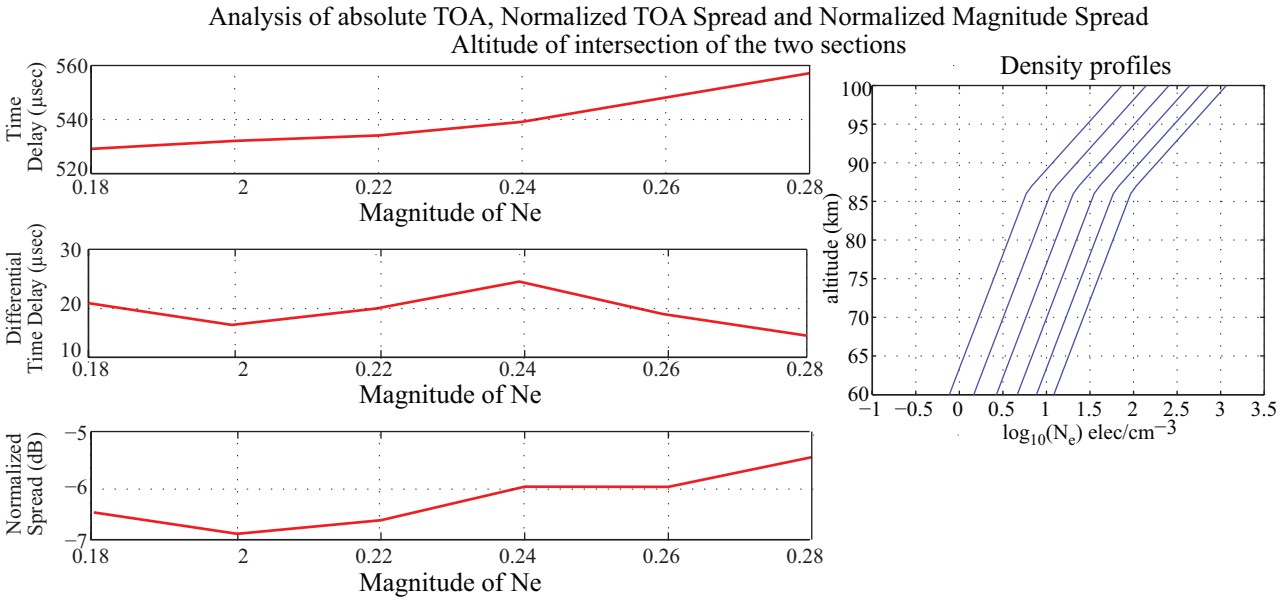

Figure 5-15. Magnitude of N_e.

modify the magnitude of the entire N_e profile. The right panel of Figure 5-15 shows the N_e profiles evaluated, and the left panels of the figure shows the variation of the three quantities as a function of N_e magnitude on log scale. It is clear from this figure that two profile matching all of the observations within error bars have been evaluated: $\Delta\log_{10}(N_e)$ is 0.20 and 0.22 elec/cm^{-3}.

5.3.1.4 Upper Section β

In the case at hand, it is unnecessary to continue the process farther because we have identified an electron density profile that can reproduce observations with the error bars. Nevertheless, we evaluate the dependence of the parameters on the upper section β for reference. Figure 5-16 demonstrates that the CW-OFF TOA can either increase or decrease with β, depending on the slope of the lower section. The TOA spread tends to increase with increasing upper section β, although it changes by less that 10 μ-seconds. Similarly, the magnitude offset and magnitude spread vary only subtly, and the direction of variation with upper section β depends on the β of the lower section.

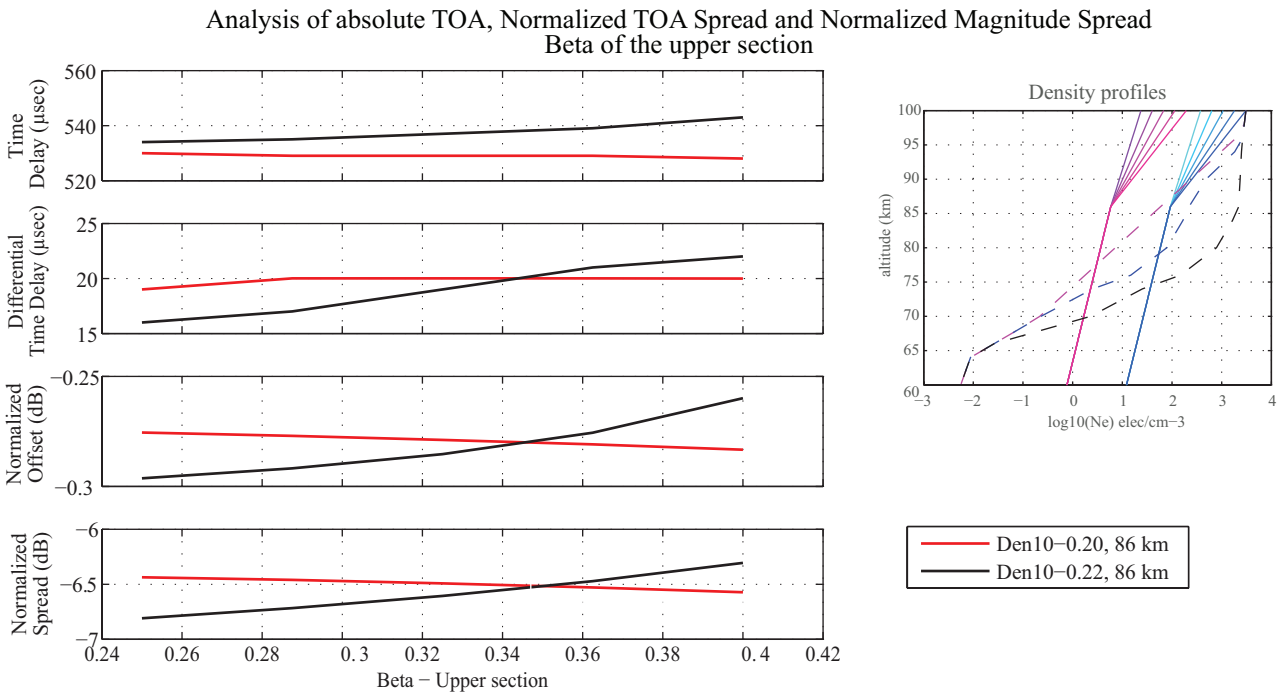

Figure 5-16. Beta of upper section.

5.4 Best Fit Piecewise-Exponential Profile

Figure 5-17 compares the model predictions at all CW power levels for the two profiles that fit experimental observations of the CW-OFF TOA, the TOA spread, the magnitude offset, and the magnitude spread. In all panels the solid green and dashed green lines represent the model predictions; the blue and red traces represent the observations. Comparing the variation of CW-OFF TOA, TOA spread, and ELF/VLF magnitude as a function of CW ERP, both model predictions generally capture the CW power dependence of each of the evaluated quantities. Based on these results, we are not able to choose between the two model profiles, but we note that they are only ∼5% different in electron density.

This chapter has presented new experimental observations using TOA analysis. The two best-fit electron density profiles (calculated assuming a linear electron temperature profile) are only different by ∼5%, suggesting ∼5% accuracy. Furthermore, the experimental TOA observations could not be accurately predicted using only

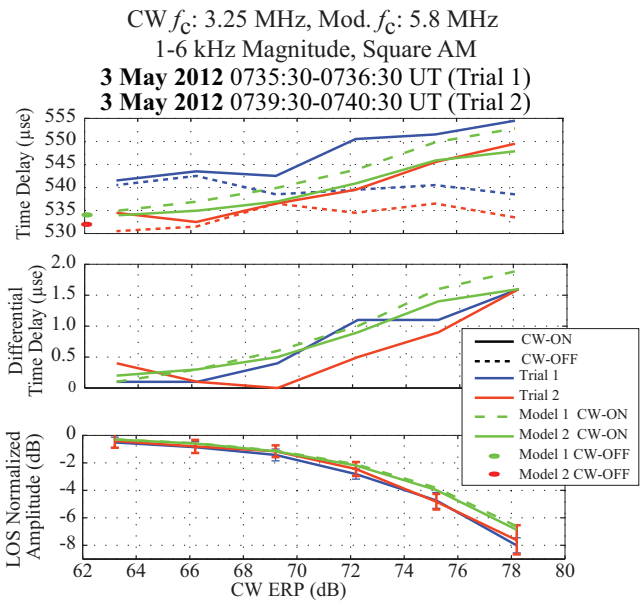

Figure 5-17. Observations along with best fit piecewise-exponential profile.

exponential electron density profiles; instead a piecewise exponential electron density profile was required to reproduce the observations. This result indicates that the dual-beam experiment is sensitive to structure within the *D*-region ionosphere, defined as a deviation from linear electron temperature profile and/or exponential electron density profile, and that the dual-beam TOA experiment is well suited to detect this type of structure.

CHAPTER 6
SUMMARY AND FUTURE WORK

In this dissertation, we identify a novel method to characterize the ambient properties of the D-region ionosphere using ground-based observations of ELF/VLF waves generated during dual-beam HF heating experiments at HAARP. Chapter 1 provided background material and a short history of D-region diagnostic techniques. Chapter 2 described the multi-beam HF heating model, including the upgrades performed in order to model various modulation waveforms and X- and O-mode polarizations of the CW HF beam. Chapter 3 outlined the dual-beam heating experiment, discussing in particular an extensive experiment conducted at HAARP in 2007. Experimental observations and model predictions of ELF/VLF wave generation were compared as a function of magnitude, harmonic ratio, and power-law exponent, and the first harmonic of the ELF/VLF magnitude was identified as the wave property that is most sensitive to the ambient D-region conditions. Chapter 4 presented a rigorous analysis that compared experimental observations of the first harmonic ELF/VLF magnitude with model predictions as a function of several transmission parameters (HF power, HF frequency, and modulation waveform). The sensitivity of the received ELF/VLF wave magnitude to these controllable parameters was evaluated and their dependence on ambient ionospheric conditions was interpreted. Lastly, Chapter 5 evaluated the conditions under which the effects of N_e and T_e could be decoupled. Dual-beam TOA experiments were identified as an excellent means to provide key additional information about the structure of the D-region ionosphere. The construction of a best-fit piecewise-exponential ambient electron density profile was described in great detail.

The following scientific contributions were demonstrated in this work:

1. A multi-beam HF ionospheric heating model was tested and validated using observations at HAARP. The functionality of the multi-beam HF heating model was successfully extended to account for five different AM waveforms, namely square,

sinusoidal, square-root-sine (sqrt-sine), triangle, and saw-tooth. The model was also extended to account for both X- and O-mode polarizations of the CW beam.

2. It was experimentally established that the magnitude of ELF/VLF wave generation is the parameter most sensitive to additional CW heating.

3. The transmission parameters that provide independent information about the ambient D-region ionosphere during dual-beam heating experiments were experimentally identified. These transmission parameters are: 1) the CW power level, 2) the frequency of the HF CW beam, 3) the modulation waveform, and 4) the polarization of the HF CW beam.

4. In the context of the HF heating model, it was demonstrated that observations performed during the dual-beam heating experiment are sensitive to structure within the D-region ionosphere. Piecewise-exponential electron density approximations appear to adequately match all available observations.

A few items that are not covered in this present dissertation, but would be rather interesting areas for future research are discussed below.

6.1 Weighted Least Square Implementation

A possible method of estimating the N_e and also T_e profiles would be to implement a weighted least square algorithm, by treating the magnitude of the B field, M ($\sqrt{B_H^2 + B_P^2}$) as a linear function of electron density profile, $N_e(h)$ and T_e.

$$M(n, h) = g(N_e(h), n) + f(T_e(h), n) \tag{6–1}$$

where n is the CW ERP level.

By varying the controllable parameters of N_e, β, h'_{int} and $\Delta log_{10}(N_e)$ at every iteration and further parameterizing T_e, possibly as a piecewise-linear profile and implementing a complex optimization algorithm [*Boyd*, 2004], we can find the best fit piecewise-exponential N_e and piecewise-linear (or any reasonably parameterized function) T_e to best match observations and get better insight into the structure of the D-region.

6.2 Extension to Higher Harmonics

In this work presented, we have only compared observations and model predictions of the magnitude of the first harmonics of the received ELF/VLF waves as a function of CW ERP. We saw in Figure 4-3 that higher harmonics were generated for all modulation waveforms, however with a significantly lower SNR compared to the first harmonic. By choosing the modulation frequency, such that there is high SNR generation of second and possibly third harmonics, depending on the modulation waveform chosen and by extending the model to properly evaluate the magnitude of the higher harmonics, it will be interesting to evaluate the magnitude variation of the higher harmonics as a function of CW ERP. This analysis could provide additional independent information to detect structure in the D-region.

6.3 HF Frequencies Within a Collision Frequency

One of the assumptions of the dual-beam HF heating model used in this work, is that the frequency of the two HF beams are such that they are more than a collision frequency from one another, such that the two HF beams do not interact with one another. Although challenging, it will be noteworthy to develop the dual-beam HF model in order to evaluate the non-linearities that result from the inter harmonic mixing between CW and modulated signal when the two HF frequencies are less a collision frequency apart. More recently there have been several experiments conducted at HAARP to experimentally evaluate these effects, such as STF-CW steps and STF-TOA. It will be exciting to evaluate the magnitude of the ELF/VLF waves and consequently the suppression as a function of CW ERP for this non-linear interaction.

6.4 Evaluation of Ionospheric Current Drive (ICD)

Recently, there have been efforts to generate ULF/ELF waves using modulated F-region HF heating without the presence of an electrojet current [e.g., *Papadopoulos et al.*, 2011a,b; *Eliasson et al.*, 2012]. This method uses the heater to modulate the F-region at low frequencies (< 50 Hz) to generate MagnetoSonic (MS) waves. By

incorporating changes in electron density with time in our existing dual-beam HF model, we could get more insight into the generation of ULF/ELF waves by ICD. This is a direct application that could provide some important information about N_e as it depends on the modulation of N_e, using lower frequencies and accounting for N_e changes with time.

6.5 HF Cross-Modulation Under Dual-Beam Heating Conditions

In Section 1.3.5, we discussed HF Cross-Modulation probing experiments that have been used to determine the extent of ionospheric conductivity modulation in the D-region ionosphere. Recently, *Langston and Moore* [2013] demonstrated using HF cross-modulation during HF heating experiments at HAARP that it was possible to quantize the D-region absorption produced by HF heating both during the initial stages of heating and under steady-state conditions. It would be interesting to calculate HF cross-modulation under dual-beam heating conditions, and in turn quantify the D-region absorption as a function of CW ERP. By evaluating the absorption produced by the piecewise-exponential N_e profiles, we could possibly further confirm the structure in the D-region.

REFERENCES

Agrawal, D., and R. C. Moore (2012), Dual-beam ELF wave generation as a function of power, frequency, modulation waveform, and receiver location, *J. Geophys. Res.*, *117*(A12305), doi:10.1029/2012JA018,061.

Appleton, E. V. (1932), Wireless studies of the ionosphere, *J. Inst. Elec. Engrs*, *71*, 642–650.

Appleton, E. V., and M. A. F. Barnett (1925), Local reflection of wireless waves from the upper atmosphere, *Nature (London)*, *115*, 333 – 334.

Banks, P. (1966), Collision frequencies and energy transfer: electrons, *Planet. Space Sci.*, *14*, 1085–1103.

Banks, P. M., and J. R. Doupnik (1975), A review of auroral zone electrodynamics deduced from incoherent scatter radar observations, *J. Atmos. Terr. Phys.*, *37*, 951–972.

Barr, R., and P. Stubbe (1984), ELF and VLF radiation from the polar electrojet antenna, *Radio Sci.*, *19*, 1111–1122.

Barr, R., and P. Stubbe (1991), ELF radiation from the Tromso Super Heater facility, *Geophys. Res. Lett.*, *18*(6), 1035–1038.

Barr, R., and P. Stubbe (1993), ELF harmonic radiation from the Tromso heating facility, *Geophys. Res. Lett.*, *20*, 2243–2246.

Bernhart, P. A., P. J. Erickson, F. D. Lind, J. C. Foster, and B. W. Reinisch (2005), Artificial disturbances of the ionosphere over the Millstone Hill Incoherent Scatter Radar from dedicated burns of the space shuttle orbital maneuver subsystem engines, *J. Geophys. Res.*, *110*(A5), A05,311.

Bittencourt, J. A. (1986), Fundamentals of Plasma Physics.

Boyd, S. (2004), *Convex Optimization*, Cambridge University Press.

Budden, K. G. (1985), *The propagation of Radio Waves: The Theory of Radio Waves: The Theory of Radio Waves of Low Power in the Ionosphere and Magnetosphere*, Cambridge University Press, Cambridge and New York.

Chau, J. L., and R. F. Woodman (2005), D and E region incoherent scatter radar density measurements over Jicamarca, *J. Geophys. Res.*, *110*(A12), doi:10.1029/2005JA011438.

Cheng, Z., S. A. Cummer, D. N. Baker, and S. G. Kanekal (2006), Nighttime D region electron density profiles and variabilities inferred from broadband measurements using VLF radio emissions from lightning, *J. Geophys. Res.*, *111*(A5), doi:10.1029/2005JA011308.

Cohen, M. B., U. S. Inan, M. Golkowski, and M. J. McCarrick (2010), ELF/VLF wave generation via ionospheric HF heating: Experimental comparison of amplitude modulation, beam painting, and geometric modulation, *J. Geophys. Res.*, *115*(A02302), doi:10.1029/2009JA014,410.

Cohen, M. B., M. Golkowski, N. G. Lehtinen, U. S. Inan, and M. J. McCarrick (2012), HF beam parameters in ELF/VLF wave generation via modulated heating of the ionosphere, *J. Geophys. Res.*, *117*(A05327).

Cummer, S. A., and U. S. Inan (1997), Measurement of charge transfer in sprite-producing lightning using ELF radio atmospherics, *Geophys. Res. Lett.*, *24*, 1731–1734.

Cummer, S. A., U. S. Inan, and T. F. Bell (1998), Ionospheric D region remote sensing using VLF radio atmospherics, *Radio Sci.*, *33*(6), 1781–1792, doi:10.1029/98RS02381.

Dalgarno, A., M. B. McElroy, M. H. Rees, and J. C. G. Walker (1968), The effect of oxygen cooling on ionospheric electron temperatures, *Planet. Space Sci.*, *16*, 1371–1380.

Davies, K. (1990), *Ionospheric Radio*, 580 pp, Peter Peregrinus Ltd., London.

de Forest, L. (1912), Absorption (?) of undamped waves, *Electrician*, *69*, 369–370.

Djuth, F. T., B. W. Reinisch, D. F. Kitrosser, J. H. Elder, A. L. Snyder, and G. S. Sales (2006), Imaging HF-induced large-scale irregularities above HAARP, *Geophys. Res. Lett.*, *33*(4), doi:10.1029/2005GL024536.

Eliasson, B., C.-L. Chang, and K. Papadopoulos (2012), Generation of elf and ulf electromagnetic waves by modulated heating of the ionospheric f2 region, *Journal of Geophysical Research: Space Physics*, *117*(A10), n/a–n/a, doi:10.1029/2012JA017935.

Fallen, C. T., J. A. Secan, and B. J. Watkins (2011), In-situ measurements of topside ionosphere electron density enhancements during an HF-modification experiment, *Geophys. Res. Lett.*, *38*(8), doi:10.1029/2011GL046887.

Fejer, J. A. (1970), Radio wave probing of the lower ionosphere by cross-modulation techniques, *J. Atmos. Terr. Phys.*, *32*(597).

Ferraro, A. J., H. S. Lee, R. Allshouse, K. Carroll, R. Lunnen, and T. Collins (1984), Characteristics of ionospheric ELF radiation generated by HF heating, *J. Atmos. Terr. Phys.*, *46*, 855–865.

Fujimaru, S., and R. C. Moore (2011a), Analysis of Time-of-Arrival Observations Performed during ELF/VLF Wave Generation Experiments at HAARP, *Radio Sci.*, *46*(RS0M03), doi:10.1029/2011RS004,695.

Fujimaru, S., and R. C. Moore (2011b), Time-of-Arrival analysis applied to the spatially distributed ELF/VLF source region above HAARP, Master's thesis, Univeristy of Florida, Gainesville.

Hargreaves, J. K. (1992), *The Solar-Terrestrial Environment*, Cambridge University Press.

Hedin, A. E. (1991), Extension of the MSIS Thermospheric Model into the Middle and Lower Atmosphere, *J. Geophys. Res.*

Holmes, J. M., T. R. Pedersen, and T. J. Mills (2011), RF-Induced airglow observed using composite multispectral imaging, *Plasma Science, IEEE Trans.*, *39*(11), 2714 – 2715.

Huxley, L. G. H., and J. A. Ratcliffe (1949), A survey of ionospheric cross-modulation, *Proc. Inst. Elec. Eng.*, *96*, 433–440.

Hysell, D. L. (2008), 30 MHz radar observations of artificial E region field-aligned plasma irregularities, *Annales Geophysicae*, *26*, 117 –129.

Jacobson, A. R., R. Holzworth, and X.-M. Shao (2008), Low-frequency ionospheric sounding with Narrow Bipolar Event lightning radio emissions: energy-reflectivity spectrum, *Annales Geophysicae*, *26*(7), 1793–1803, doi:10.5194/angeo-26-1793-2008.

James, H. G., R. L. Dowden, M. T. Rietveld, P. Stubbe, and H. Kopka (1984), Simultaneous observations of ELF waves from an artificially modulated auroral electrojet in space and on the ground, *J. Geophys. Res.*, *89*, 1655–1666.

Kendall, E., R. Marshall, R. T. Parris, A. Bhatt, A. Coster, T. Pedersen, P. Bernhardt, and C. Selcher (2010), Decameter structure in heater-induced airglow at the High frequency Active Auroral Research Program facility, *J. Geophys. Res.*, *115*(A8), doi:10.1029/2009JA015043.

Kou, Y., X. Zhou, Y. Morton, and L. Zhang (2010), Processing GPS L2C signals under ionospheric scintillations, in *Position Location and Navigation Symposium (PLANS)*, pp. 771 – 782, IEEE/ION.

Labitzke, K., J. J. Barnett, and B. E. (eds.) (1985), Handbook MAP 16, SCOSTEP, University of Illinois, Urbana.

Langston, J., and R. C. Moore (2013), High time resolution observations of HF cross-modulation withing the D-region ionosphere, *Geophys. Res. Lett.*, p. doi:10.1002/grl.50391.

Lay, E. H., and X. M. Shao (2011), Multi-station probing of thunderstorm-generated D-layer fluctuations by using time-domain lightning waveforms, *Geophys. Res. Lett.*, *38*(23), doi:10.1029/2011GL049790.

Lehtinen, N. G., and U. S. Inan (2008), Radiation of ELF/VLF waves by harmonically varying currents into a stratified ionosphere with application to radiation by a modulated electrojet, *J. Geophys. Res.*, *113*(A06301).

Maslin, N. M. (1974), Theory of energy flux and polarization changes of a radio wave with two magnetoionic components undergoing self demodulation in the ionosphere, *Royal Society of London Proceedings Series A*, *341*, 361–381.

Mathews, J. D. (1984), The incoherent scatter radar as a tool for studying the ionospheric D-region, *Journal of Atmospheric and Terrestrial Physics*, *46*(11), 975 – 986, doi:10.1016/0021-9169(84)90004-7.

Mathews, J. D. (1986), Incoherent Scatter Radar Probing of the 60-100 km Atmosphere and Ionosphere, *IEEE Trans. on GeoSci. and Remote Sensing*, *GE-24*(5), 765–776.

McRae, W. M., and N. R. Thomson (2000), VLF phase and amplitude: daytime ionospheric parameters, *Journal of Atmospheric and Solar-Terrestrial Physics*, *62*(7), 609–618.

Mentzoni, M. H., and R. V. Row (1963), Rotational excitation and electron relaxation in nitrogen, *Phys. Rev.*, *130*, 2312–2316.

Milikh, G. M., and K. Papadopoulos (2007), Enhanced ionospheric ELF/VLF generation efficiency by multiple timescale modulated heating, *Geophys. Res. Lett.*, *34*.

Milikh, G. M., A. Gurevich, K. Zybin, and J. Secan (2008), Perturbations of GPS signals by the ionospheric irregularities generated due to HF-heating at triple of electron gyrofrequency, *Geophys. Res. Lett.*, *35*(L22102).

Milikh, G. M., E. Mishin, I. Galkin, A. Vartanyan, C. Roth, and B. W. Reinisch (2010), Ion outflows and artificial ducts in the topside ionosphere at HAARP, *Geophys. Res. Lett.*, *37*, L18,102, 1 – 4.

Moore, R. C. (2007), ELF/VLF wave generation by modulated HF heating of the auroral electrojet, Ph.D. thesis, Stanford University, Stanford, California.

Moore, R. C., and D. Agrawal (2011), ELF/VLF wave generation using simultaneous CW and modulated HF heating of the ionosphere, *J. Geophys. Res.*, *116*(A04217), doi:10.1029/2010JA015,902.

Moore, R. C., U. S. Inan, T. F. Bell, and E. J. Kennedy (2007), ELF waves generated by modulated HF heating of the auroral electrojet and observed at a ground distance of 4400 km, *J. Geophys. Res.*, *112*(A05309).

Nicolet, M., and A. C. Aikin (1960), The Formation of the D-Region of the Ionosphere, *J. Geophys. Res.*, *65*(5), 1469–1483.

Papadopoulos, K., C. L. Chang, P. Vitello, and A. Drobot (1990), On the efficiency of ionospheric ELF generation, *Radio Sci.*, *25*, 1311–1320.

Papadopoulos, K., T. Wallace, M. McCarrick, G. M. Milikh, and X. Yang (2003), On the efficiency of ELF/VLF generation using HF heating of the auroral electrojet, *Plasma Phys. Rep.*, *29*, 561–565.

Papadopoulos, K., T. Wallace, G. M. Milikh, W. Peter, and M. McCarrick (2005), The magnetic response of the ionosphere to pulsed HF heating, *Geophys. Res. Lett.*, *32*(L13101).

Papadopoulos, K., N. A. Gumerov, X. Shao, I. Doxas, and C. L. Chang (2011a), Hf-driven currents in the polar ionosphere, *Geophysical Research Letters*, *38*(12), n/a–n/a, doi:10.1029/2011GL047368.

Papadopoulos, K., C.-L. Chang, J. Labenski, and T. Wallace (2011b), First demonstration of hf-driven ionospheric currents, *Geophysical Research Letters*, *38*(20), n/a–n/a, doi:10.1029/2011GL049263.

Payne, J. A. (2007), Spatial structure of very low frequency modulated ionospheric currents, Ph.D. thesis, Stanford University, Stanford, California.

Payne, J. A., U. S. Inan, F. R. Foust, T. W. Chevalier, and T. F. Bell (2007), HF modulated ionospheric currents, *Geophys. Res. Lett.*, *34*(L23101).

Pickett, J. S., G. B. Murphy, W. S. Kurth, C. K. Goertz, and S. D. Shawhan (1985), Effects of Chemical Releases by the STS 3 Orbiter on the Ionosphere, *J. Geophys. Res.*, *90*(A4), 3487–3497.

Prakash, S., and R. Pandey (1984), Rocket borne studies of electron density irregularities in equatorial D and E regions, *J. Earth System Science*, *93*(3), 283–308.

Prasad, S. S., and D. R. Furman (1973), Electron cooling by molecular oxygen, *J. Geophys. Res.*, *78*, 6701–6707.

Rakov, V. A., and M. A. Uman (2003), *Lightning Physics and Effects*, ISBN 0521583276, PB ISBN 0521035414, Cambridge University Press.

Rietveld, M. T., H. Kopka, and P. Stubbe (1986), D-region characteristics deduced from pulsed ionospheric heating under auroral electrojet conditions, *J. Atmos. Terr. Phys.*, *48*, 311–326.

Rietveld, M. T., P. Stubbe, and H. Kopka (1989), On the frequency dependence of ELF/VLF waves produced by modulated ionospheric heating, *Radio Sci.*, *24*, 270–278.

Rishbeth, H., and O. K. Garriott (1969), *Introduction to Ionospheric Physics*, New York: Academic Press.

Rodriguez, J. V. (1994), Modification of the Earth's ionosphere by very-low-frequency transmitters, Ph.D. thesis, Stanford University, Stanford, California.

Sechrist, C. F. J. (1974), Comparison of techniques for measurement of D-region electron densities, *Radio Sci.*, *9*(2), 137–149.

Seddon, J. C., A. D. Pickar, and J. E. Jackson (1954), Continuous Electron Density Measurements Up To 200 km, *J. Geophys. Res.*, *59*(4), 513–524.

Senior, A., M. T. Rietveld, M. J. Kosch, and W. Singer (2010), Diagnosing radio plasma heating in the polar summer mesosphere using cross modulation: Theory and observations, *J. Geophys. Res.*, *115*(doi:10.1029/2010JA015379), A09,318.

Stubbe, P., and H. Kopka (1977), Modulation of polar electrojet by powerful HF waves, *J. Geophys. Res.*, *82*, 2319–2325.

Stubbe, P., and W. S. Varnum (1972), Electron energy transfer rates in the ionosphere, *Planet. Space Sci.*, *20*, 1121–1126.

Stubbe, P., H. Kopka, and R. L. Dowden (1981), Generation of ELF and VLF waves by polar electrojet modulation: Experimental results, *J. Geophys. Res.*, *86*, 9073–9078.

Stubbe, P., H. Kopka, M. T. Rietveld, and R. L. Dowden (1982), ELF and VLF wave generation by modulated HF heating of the current carrying lower ionosphere, *Journal of Atmospheric and Terrestrial Physics*, *44*(12), 1123–1135.

Tellegen, B. D. H. (1933), Interactions between radio waves, *Nature (London)*, *131*, 840.

Tomko, A. A. (1980), *D* region absorption effects during high-power radio wave heating,, *Radio Sci.*, *15*, 675–682.

Tomko, A. A. (1981), Nonlinear phenomena arising from radio wave heating of the lower ionosphere, *Technical Report PSU-IRL-SCI-470*, Ionosphere Research Laboratory, Pennsylvania State University, University Park, Pennsylvania.

Tripathi, V. K., C. L. Chang, and K. Papadopoulos (1982), Excitation of the Earth-ionosphere waveguide by an ELF source in the ionosphere, *Radio Sci.*, *17*, 1321–1326.

Tulasi, S. R., S. Y. Su, C. H. Liu, B. W. Reinisch, and L. A. Mckinnell (2009), Topside ionospheric effective scale heights (HT) derived with ROCSAT-1 and ground-based ionosonde observations at equatorial and midlatitude stations, *J. Geophys. Res.*, *114*(A10), A10,309.

Ulwick, J. C., K. D. Baker, M. C. Kelley, B. B. Balsley, and W. L. Ecklund (1988), Comparison of Simultaneous MST Radar and Electron Density Probe Measurements During STATE, *J. Geophys. Res.*, *93*(D6), 6989–7000.

Villard, O. G. J. (1976), The ionospheric sounder and its place in the history of radio science, *Radio Sci.*, *11*(11), 847 – 860.

Villasenor, J., A. Y. Wong, B. Song, J. Pau, M. McCarrick, and D. Sentman (1996), Comparison of ELF/VLF generation modes in the ionosphere by the HIPAS heater array, *Radio Sci.*, *31*, 211–226.

Wait, J. R., and K. P. Spies (1964), Characteristics of the Earth-ionosphere waveguide for VLF radio waves, *Tech. rep.*, National Blur. of Stand., Boulder, Colo.

Weisbrod, S., A. J. Ferraro, and H. S. Lee (1964), Investigation of phase interaction as a means of studying the lower ionosphere, *J. Geophys. Res.*, *69*(2337).

Zinn, J., and C. D. Sutherland (1980), Effects of rocket exhaust products in the thermosphere and ionsphere, *Technical Report LA-8233-MS*, Los Alamos Scientific Lab., NM (USA).

BIOGRAPHICAL SKETCH

Divya Agrawal received her Bachelor of Science in Electronics and Communication engineering in 2005 from Sri Jayachamarajendra College of Engineering, India. She earned a Master of Science degree and a Ph.D. in Electrical and Computer Engineering in 2008 and 2013, respectively, from the University of Florida, Gainesville, Florida. Her interests include signal processing, antenna design, and electromagnetic field theory.